TECHNISCHE UNIVERSITÄT MÜNCHEN

Fakultät für Chemie

Lehrstuhl für Theoretische Chemie

D I S S E R T A T I O N

Dissociation and dissipation dynamics of adsorbates at solid surfaces

Vanessa Jane Bukas

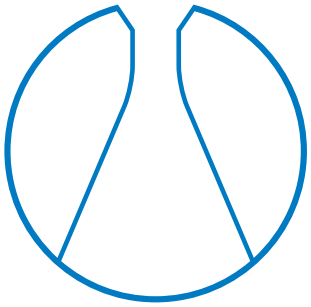

Garching b. München, 2016

TECHNISCHE UNIVERSITÄT MÜNCHEN

Fakultät für Chemie

Lehrstuhl für Theoretische Chemie

Dissociation and dissipation dynamics of adsorbates at solid surfaces

Vanessa Jane Bukas

Vollständiger Abdruck der von der Fakultät für Chemie der Technischen Universität München zur Erlangung des akademischen Grades eines

Doktors der Naturwissenschaften (Dr. rer. nat.)

genehmigten Dissertation.

Vorsitzende(r) : Prof. Dr. Hubert A. Gasteiger

Prüfer der Dissertation:

1. Prof. Dr. Karsten Reuter
2. Prof. Dr. Ville Kaila
3. Prof. Dr. Axel Groß

Die Dissertation wurde am 24.10.2016 bei der Technischen Universität München eingereicht und durch die Fakultät für Chemie am 09.12.2016 angenommen.

Preface

This dissertation is a publication-based doctoral thesis. The work which is hereby presented has been published or has been submitted for publication in international peer-reviewed scientific journals. Following a comprehensive overview of the main concepts and methods in Part I, Part II provides short summaries for each of the aforementioned papers and lists the individual contributions of the corresponding co-authors. The gained insight along with the various methodological developments which are part of this work overall stimulate a plethora of potential future studies with interesting applications both within and beyond the specific context that has been investigated here. Some of these are surveyed in a concluding outlook section, along with a broader scope synopsis that integrates our scientific work into the existing literature. Finally, the three papers already published and one paper accepted for publication are appended in Part III as an attachment to this thesis. One submitted manuscript is not included in order to avoid prior-to-publication copyright issues, yet will be made available to the examination committee.

All work which is presented was performed between November 2012 – October 2016 at the Chair of Theoretical Chemistry of the Technische Universität München and under the supervision of Prof. Dr. Karsten Reuter.

Vanessa Jane Bukas, Garching b. München, October 2016

Contents

Summary (Zussamenfassung)

Exothermic surface reactions may release several electron volts of energy. Fundamental questions regarding the conversion and dissipation of this microscopically sizable amount of energy are critical in e.g. present day energy production and pollution mitigation. Here, we promote microscopic understanding through large-scale molecular dynamics simulations. A novel multi-scale embedding approach allows, for the first time, to model phononic dissipation at the nanoscale from first-principles.

Exotherme Oberflächenreaktionen setzen häufig mehrere Elektronvolt Energie frei. Fundamentale Fragen, bezüglich der Umsetzung und Dissipation mikroskopischer Energie, sind von Bedeutung für z.B. die Energieerzeugung und Emissionsverringerung. Diese Arbeit zielt auf das mikroskopische Verständnis durch aufwändig Molekulardynamik-Simulationen. Ein neuartiger Multiskalen-Einbettungs-Ansatz erlaubt es, zum ersten mal Phononendissipation auf der Nanometerskala mit ab-initio Methoden zu modellieren.

Part I.

Overview & Methods

1. Introduction

The field of gas-surface dynamics has been an active field of research for many decades and is ever the more driven and exploited by the materials industry in order to enhance the performance for a number of important technical processes. A prominent example is that of heterogeneous catalysis which plays a critical role in chemical conversion, energy production and pollution mitigation, and yet in many cases eludes a proper microscopic understanding in terms of the involved elementary processes. Today due to continuous increases in computer power and the development of efficient algorithms for electronic structure calculations, the community is all the more turning for answers towards predictive quality simulations based on high-level theoretical approaches such as density functional theory (DFT) [1, 2].

Unfortunately, the inherent complexity of adsorption processes in particular at metal surfaces still poses enormous challenges to corresponding first-principles approaches and quantitative dynamical descriptions may remain an elusive hallmark even in cases of seemingly simple adsorbates [3]. The challenges to be met by theory include at the electronic structure level prominently the simultaneous reliable description of localized molecular orbitals and delocalized metal band structure [4, 5]. In the meantime, corresponding molecular dynamics (MD) simulations are additionally being faced with exploring the vast configurational spaces encountered by initially random gas-phase molecules when impinging into the potential of the solid surface [6]. This receives even further stimulus from the basic energy science perspective which requires that DFT suitably enters into dynamical modeling in order to answer fundamental questions such as the conversion of energy forms at interfaces.

A particular example is the conversion of chemical energy to heat which arises as a consequence of an adsorbate's exothermic interaction with the surface. For a prototypical model reaction like the dissociative oxygen adsorption, scanning-tunneling microscopy (STM) experiments have suggested delayed dissipation of the released chemical energy with the concomitant formation of so-called "hot adatoms" on several metal surfaces [7–13]. This essentially implies dissociation fragments with a kinetic energy large enough to travel on the surface even at temperatures where thermal motion would nominally be prohibited. Thereby defying the notion of a (uniform) global temperature, this transient mobility intricately couples the elementary reaction steps of dissociation and diffusion; an implication hitherto not considered in present-day microkinetic formulations in surface catalysis [14, 15]. Concepts embracing such "hot reactions" are nevertheless becoming increasingly established over the past decades [16] and attract a lot of attention in view of their ability to generate hot precursors for subsequent reaction steps [17]. This offers promises for strongly influencing rates in e.g. heterogeneous catalysis [18], while also playing a vital role in epitaxial growth mechanisms at low temperatures [19]. As the experimental quest to generate molecular movies of such reactions is still ongoing, theory is (aided of course also by significant advances on the practical level) making tremendous progress in elucidating the reaction and ensuing equilibration dynamics.

Using large-scale MD simulations, the present thesis investigates from first-principles the first steps of oxygen adsorption at transition metal surfaces; a key process in oxidation catalysis. New microscopic insight is reached with respect to the chemical reactivity of

such processes, while key efforts are placed on advancing conceptual and methodological understanding from a modeling perspective. In this context, a principal objective concerns the physics of dissipating the energy released during exothermic surface reactions into lattice vibrations of the underlying substrate, i.e. phonons. Cited only recently as one of the major conceptual problems in contemporary gas-surface dynamical modeling [3], we employ here a hierarchical application of increasingly advanced theoretical models in order to disentangle the role of phononic dissipation and elucidate its influence both during the early stages of adsorption and the ensuing highly non-equilibrium thermalization process. Through a combination of existing and newly-established methodologies, we thereby address fundamental aspects of dynamical surface processes (adsorption, dissociation, and diffusion), while paving the way towards a deeper atomistic understanding of energy conversion at interfaces in general.

In the following, we specifically provide a comprehensive overview of the central concepts and methods that the present thesis is based upon. An extensive literature review complements the provided theoretical background, while the main scope, challenges, and results are placed in the wider context of the current state of research. Following a brief introduction to the main methods employed in this thesis for obtaining energies and forces, we thus continue in section 3 by reviewing contemporary theoretical approaches and the underlying approximations that have come to define the state-of-the-art in gas-surface dynamical modeling. Section 4 outlines the basic principals behind the so-called divide-and-conquer approach which serves as the main workhorse for a major part of this work, in determining e.g. the small reaction probabilities of O_2 at a rigid Ag(100) surface [20]. We continue in section 5 with various effective accounts of substrate mobility which are used to augment divide-and-conquer type MD simulations with some account of energy exchange between the adsorbate and underlying lattice [21], in a detailed comparison to high-quality experimental data [22]. Motivated by the qualitative effect arising from the inclusion of phononic dissipation already during the first steps of O_2 adsorption at Pd(100), we proceed in section 6 with the development of the QM/Me embedding approach for metals [23]. QM/Me augments self-standing *ab initio* MD simulations with a fully quantitative account of phononic dissipation into a macroscopic heat bath and thus allows for following the entire reaction dynamics towards equilibration. Using the exothermic O_2 dissociation at different Pd surfaces as a representative showcase, we thereby scrutinize the intricate "hot" adatom mobility from a first-principles perspective, comparing to STM data where available, and addressing further implications brought forth by the unraveled hot chemistry [24]. Section 7 details the derivation of a rigorous phonon projection scheme which is subsequently used to identify the dominant dissipation channels for the released chemical energy in a mode-specific manner [25]. Offering unprecedented insight into the microscopic details of the dissipative dynamics, the corresponding analysis reveals a sensitive dependence on the phononic fine structure, while highlighting the importance of specific surface excitations and questioning prevalent assumptions about energy sinks made in commonly used model bath Hamiltonians (cf. for example Refs. [26–29] and references therein).

2. Obtaining total energies & forces

The making and breaking of chemical bonds during surface reactions calls for an *ab initio* quantum-mechanical description on the atomic scale. For periodic metal systems with large surface unit cells, density functional theory (DFT) has so far proven an unbeatable method of choice and has thus firmly established itself as the workhorse for electronic structure calculations in surface science [1, 2]. In particular for simple adsorbates at transition metal surfaces, present-day DFT can reach a most comprehensive description that encompasses all standard experimental characterization in ultra-high vacuum (UHV) conditions [30]. Capturing this level of precision in the adsorbate-substrate interaction is very difficult, or even impossible, through classical interatomic potentials (CIPs). Even if parametrized from first-principles calculations, semi-empirical potentials generally show limited transferability and hence bear the risk of a reduced (potentially even misleading) predicitive power. On the other hand, CIPs of a many-body functional form have been shown to yield remarkable success when it comes to describing the elastic properties of a "bare" metal. As such, the numerical efficiency that comes with the latter has been exploited in the present work for modeling a macroscopic substrate heat bath that will incorporate a realistic description of the metal's phononic fine structure (cf. sections 6 and 7). One of the more straightforward and convenient choices for this purpose is the (modified) embedded atom method ((M)EAM) [31–33]. Both DFT and MEAM evaluations thus form the basis of the present work in terms of obtaining the required total energies/forces, and are hence briefly recapitulated in the following.

Density functional theory

While its conceptual roots lie in the early Thomas-Fermi model [34, 35] of solid state physics, DFT was only put on a firm theoretical footing in 1964 by the two Hohenberg-Kohn theorems [36]. The ground-state electron density was thus established as the basis for DFT and connected to a variational principle analogous to that in wave mechanics [37] for minimizing the (ground-state) total energy. The success of modern DFT methods is nevertheless chiefly based on the ingenious proposition brought forth by Kohn and Sham in 1965 [38]. Aiming at an applicable ansatz for practical (computer) calculations, the Kohn-Sham scheme effectively reduces the intractable many-body problem of interacting electrons that move in a static external potential. This is achieved by mapping onto a fictitious reference system of non-interacting particles that exist in the environment of an effective (so-called Kohn-Sham) potential to generate the exact same density as the real (interacting) system. The accuracy of Kohn-Sham DFT is thus ultimately determined by the reliable representation of all electronic quantum-mechanical many-body effects that are, by construction, incorporated in this effective potential. Exact analytical expressions for describing exchange and correlation interactions, however, remain unknown. Their contributions must therefore be approximated in practice through the so-called exchange-correlation (xc) functional. The adversity beheld therein lies in the reliable representation of the respective function's non-local nature and one may argue that all present formulations in principle still represent an uncontrolled approximation [39]. The development of more accurate xc expressions is, however, a very active research field and with the ap-

pearance of each new functional there tends to be at least one publication benchmarking its performance on a variety of standard test sets [39].

Probably the most popular approach to date is the generalized gradient approximation (GGA) which is an 'extension' to the older local density approximation (LDA) and depends not only on the local value of the electron density but also on (a 'corrected' version of) its gradient (hence, also termed semi-local DFT). The first widely accepted GGA exchange functional was developed by Becke [40], and followed by a staggering amount of others which are typically denoted in literature by concatenating the initials of the respective authors. The most prominent example of such functionals which (in contrast to that of Becke) contain no empirically optimized parameters is that of Perdew and Wang (PW91) [41], which was subsequently simplifed by Perdew, Burke and Ernzerhof (PBE) [42, 43], and later on revised by Hammer, Hansen and Nørskov (RPBE) [44]. The PBE, RPBE flavors of semi-local xc also form the basis for all DFT calculations performed within the context of the present thesis; as the latter have been implemented within the plane-wave CASTEP code [45] (cf. Ref. [21]) and all-electron FHI-aims code [46] (cf. Refs. [24, 25, 47]). Although certainly not without its limitations [3, 4], we altogether deem this choice (as compared to e.g. the use of a so-called meta-GGA functional [48] that would additionally include the second derivative of the electron density) a reasonable and sufficiently accurate compromise with respect to computational efficiency for the present purposes of capturing the chemistry of bond dissociation/formation at a metal surface.

The (modified) embedded atom method

The EAM was developed by Daw and Baskes in the 1980s [31, 32] and has its foundations in density functional theory. As with any CIP, the basic concept lies in reducing the interaction between the nuclei to a simple analytical functional form that "hides" all quantum-mechanical complexity of the electronic structure. Specifically targeting the delocalized character of chemical binding in metals, EAM achieves this through a simple pair potential expression that is appropriately augmented by a many-body correction term. The latter comes in the form of an atomic embedding energy, while assuming that each atom of the solid is seen as an impurity in the host electron density of all the other atoms. This so-called quasi-atom concept [49] then motivates the following ansatz form for the EAM interatomic potential:

$$V^{\mathrm{EAM}}(\mathcal{R}) = \sum_i \left[\frac{1}{2} \sum_{j \neq i} \phi_{\mathrm{ij}}(R_{ij}) + F_i \left(\sum_{j \neq i} \rho_{\mathrm{h,i}}(R_{ij}) \right) \right] \quad , \tag{2.1}$$

where i, j denote summations over atoms with distance R_{ij} between them. The first and second terms in the main sum represent the pair potential and many-body contributions, respectively. The so-called embedding function F is responsible for capturing all complexity of 'embedding' each atom into the metal and, in the spirit of the local density approximation of DFT, depends only on the background host electron density ($\sum_{j \neq i} \rho_{\mathrm{h,i}}(R_{ij})$) at the site of the respective quasi-atom i. Different functional forms have generally been proposed for ϕ, F, and ρ_{h}. These typically incorporate material-specific parameters that have either been related to physical properties through available experimental data, or taken directly from first-principles calculations. EAM's modified successor, MEAM [33], for example employs more stringent forms for the aforementioned terms, thereby reducing the parametrization effort required from DFT. Altogether, both EAM and MEAM have overall met remarkable success in the calculation of material-specific phonon properties [50], also for the case of transition metal surfaces [51–54] which is of particular relevance to the present work.

3. Modeling chemical reaction dynamics at surfaces from first-principles

The impingement of molecules onto a solid surface occurs with initially randomly distributed molecular orientations and lateral positions. A discussion of gas-surface dynamics must thereby inevitably consider some statistical aspects. Following the time evolution of individual impingement events through molecular dynamics (MD) simulations offers most detailed insight into the adsorption process, and corresponding studies have in fact predominantly established the mechanistic understanding that we have today. In obtaining data, however, that can be directly compared to experimentally measured kinetic quantities such as e.g. the (initial) sticking coefficient, this dynamical information needs to be appropriately averaged over an entire ensemble of trajectories.

As a practical consequence of the Born-Oppenheimer approximation (BOA) [55], the adiabatic potential energy surface (PES) describing the adsorbate-substrate interaction can conveniently be invoked in order to propagate the nuclear system in time by solving the appropriate classical or quantum-mechanical equations of motion. The key concern then lies in obtaining a numerically efficient, yet sufficiently accurate, description of the aforementioned molecule-surface potential; a challenge which is presently still ongoing. Although all the more accurate BOA-based numerical solutions of the Schrödinger equation have become available during the last nine decades, the dimensionality of the problem still remains a major limitation to employing the PES concept in practice.

One-dimensional potential curves, along with pioneering ideas regarding dissociation at surfaces, were introduced already in 1932 by Lennard-Jones [56]; whom the corresponding classical interatomic potentials (CIPs) are named after. Still, the first quantitative evaluations (based on several thousands of trajectories) did not come until about forty years later through simple analytical PES forms that were derived from e.g. re-parametrizing Morse potentials [57–61]. It soon became clear, however, that such semi-empirical CIPs – with the London-Eyring-Polanyi-Sato (LEPS) approach as the most prominent example – are generally not flexible enough to capture the complex bond breaking and making involved in a dissociative or recombination event [61] (although promising steps towards more accurate parametrizations from first principles have been reported more recently [62, 63]). With *ab initio* methods starting to become available in the 1990s, also for the treatment of adsorption at metal surfaces, the predictive power of material-specific modeling met an evolutionary boost. This came, however, at a tremendous increase in computational cost.

Given this situation, it is not surprising that first prototypical DFT-based dynamical studies focused predominantly on light H_2 adsorbates due to their relatively "simple" electronic structure on the one hand, and huge mass mismatch with respect to the underlying metal atoms on the other. The latter was specifically invoked in order to justify the inherent neglect of substrate mobility, and thus significantly reduce the computational effort to explicitly considering only the (at most, six) internal degrees of freedom corresponding to a diatomic adsorbate. This simplification then also promotes a so-called divide-and-conquer strategy where the extensive statistical MD sampling is preceded by the construction of a numerically efficient continuous PES function of *ab initio* quality, as will be detailed in the next section. As reviewed by Darling and Holloway [64], only two or three molecular

degrees of freedom were typically included in these early studies, while the nuclei of the hydrogen atoms were treated both classically and quantum-mechanically. The first six-dimensional dynamical treatment from DFT was presented by Groß and co-workers for H_2 adsorbing at an immobile (or "frozen") Pd(100) surface [65–67]. This, along with a number of subsequent studies (cf. for example Refs. [68–73]), have overall outlined the dangers of relying on a reduced number of adsorbate degrees of freedom and show that it can give rise to dramatically wrong results with respect to thereby extracted dynamical properties. A low-dimensional PES representation may, for example, fail to capture the intermediate products that result in lowering of a dissociative activation barrier (often involved in heterogeneous catalysis), hence leading to substantial errors in the calculation of reaction rates [1]. Consequently, facing the (at least) six-dimensional problem for diatomic adsorbates currently defines the state-of-the-art in gas-surface dynamical modeling and is an established necessity; reported as potentially more important than a quantum-mechanical treatment of the nuclei, even in the case of hydrogen [74].

Going beyond the frozen surface approximation largely precludes to stay within the divide-and-conquer ansatz given the problem's exploding dimensionality and the concomitant increasing difficulty associated with each added degree of freedom when constructing a continuous PES representation. For heavier and in particular stronger interacting molecules than hydrogen, however, some account of substrate mobility must be included in the theory in order to procure a means of dissipating the released chemical energy. With respect to the reaction exothermicity, this view is nurtured by considering that freed enthalpies can well be of the order of several eVs. This is e.g. also the case for the dissociative adsorption of oxygen molecules at the catalytically relevant transition metal surfaces that the present thesis focuses on. Such amounts of energy are particularly sizable on the scale of phononic degrees of freedom, and would call for efficient microscopic dissipation channels to achieve the assumed quasi-instantaneous local equilibration that is still fundamentally relied upon in prevalent models of chemical kinetics [75]. At metallic substrates of course, electronic excitations could also potentially represent an important additional energy sink. While the latter would signal a fundamental breakdown of the BOA, the contributing role of electronic non-adiabaticity in the process of gas-surface energy transfer remains unclear and is currently still under vivid discussion [76]. With both experimental and theoretical evidence existing to weigh either side of the discussion (cf. for example Refs. [77, 78]), unfortunately no concencus has yet been reached regarding the specific systems or conditions under which this additional energy sink might be expected to play a significant role. For the particular O_2/Pd(100) showcase investigated in the context of this thesis, however, a first-principles based estimate of the energy loss into electron-hole pair excitations was calculated to amount to less than 5% of the total chemisorption energy [77]. We therefore conveniently chose to remain here within the BOA and focus instead on an accurate description of the phononic dissipation channel as a very important, if not dominant, part of the dissipative dynamics.

In this respect, theoretical models incorporating an effective treatment of substrate mobility [79–83], as those discussed in section 5, may offer an invaluable contribution. Such approaches generally target to reduce the phononic fine structure of the substrate into computationally convenient augmentations of the frozen-surface interaction in order to include at least some approximative account of energy exchange with the lattice. Applied within a divide-and-conquer framework, corresponding MD simulations exploit the numerical efficiency that comes with the latter and can provide extremely useful insight regarding the importance of phononic effects, the influence of surface temperature, etc. Albeit approximate and despite its obvious limitations, this methodology has met an overall intriguing consistency with respect to experimental sticking or scattering probabilites for e.g. H_2 at Pd [84–86]. Taking away from its *ab initio* flavor, however, a major practi-

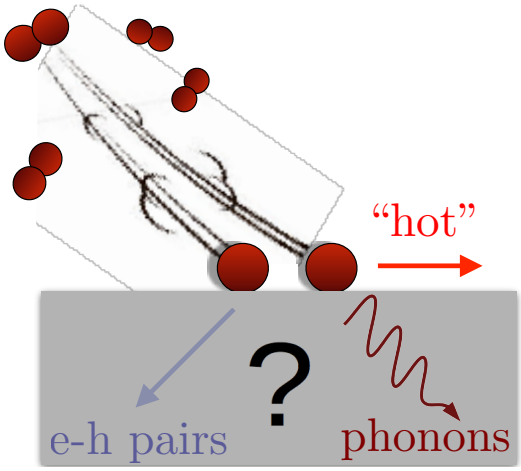

Figure 3.1.: Schematic illustration of dissociative adsorption from an ensemble of gas-phase diatomics as they impinge on a metal surface. Microscopic dissipation channels for the released chemical energy include the (electronically non-adiabatic) excitation of electron-hole pairs and the excitation of substrate phonons. The rate of interfacial energy conversion may lead to delayed adsorbate thermalization with the resulting "hot" transients acting as precursors in subsequent reaction steps.

cal bottleneck still lies in the assumptions that have to be made with respect to the bath Hamiltonian.

On the other hand, direct *ab initio* MD (AIMD) simulations stand entirely free of any such parametrizations. The forces needed to integrate the equations of motion are computed "on-the-fly" by first-principles electronic structure calculations, thereby overcoming prevailing limitations of the divide-and-conquer ansatz with respect to substrate mobility and also the complexity of the adsorbing molecule. Nevertheless, the enormous computational cost of evaluating such forces (even if based on efficient semi-local DFT) only allowed for the first AIMD attempts in gas-surface dynamics to start appearing within the last decade or so. With the advent of supercomputers and continuous developments towards improved algorithms for electronic structure calculations, it is nowadays becoming increasingly possible to compute a meaningful number of AIMD trajectories for obtaining statistically significant reaction probabilities and to study adsorption processes that could not be addressed even a few years ago [74].

The first *ab initio* study targeting "hot" adatom diffusion was launched by Groß in 2009 for the prototypical H_2 adsorption at Pd(100) and based on about one hundred trajectories [87]. This already demonstrated the importance of energy dissipation in determining the transient mobility of the hyperthermal dissociation products, despite the aforementioned large mass mismatch between hydrogen and surface atoms. What nevertheless remains to be resolved before such AIMD simulations can generally be used for the quantitative study of dynamical surface processes is the appropriate coupling to a *macroscopic* heat sink in order to treat phonons and their propagation with the same quality that is used for the adsorbate-substrate interaction. While the versatility of the AIMD methodology inherently allows for substrate mobility, this is only within computationally tractable simulation cells comprising a few surface lattice constants and layers. For example, the calculations in Groß' pioneering study (which took over a year to be completed) were based on a periodic DFT cell containing about one hundred substrate atoms. The propagation of long-range phonon modes can thereby only unavoidably be limited due to unphysical reflections at the boundaries of the latter, i.e. the energy transferred into the phononic degrees of freedom has no possibility of leaving the system. This manifests

an arising need for developing an appropriate scheme which will be designed to treat the interactions of both the impinging molecule and dissociation products with the metal substrate on a first-principles level, while simultaneously providing an accurate description of phonon excitations. Sections 6 and 7 of the present thesis discuss efficient strategies in this direction and constitute an important step in opening the road towards obtaining the entire dynamical picture of adsorption, involving more complex systems (beyond the prototypical H_2 adsorbate) and including the experimentally alluded intricate "hot" adatom motion.

4. The "divide-and-conquer" approach

Within the so-called divide-and-conquer approach, DFT calculations go as far as to provide a discrete set of total-energy data that discretely maps out the adsorbate-surface interaction on a finite mesh. Constructing a *continuous* PES representation which is both accurate and computationally inexpensive then constitutes a crucial second step in order to procure an efficient means for extensively evaluating potential energies and gradients. Within the Born-Oppenheimer approximation [55], the actual dynamical simulations are thus finally performed on such a continuous function by solving either classical or quantum-mechanical equations of motion. Appropriate averages over a sufficiently large number of trajectories can thereby routinely be obtained using computational resources commonly available nowadays in order to give access to the adsorption dynamics and arrive at a quantitative understanding of central kinetic parameters such as (dissociative) sticking probabilities. Targeted quantities that require statistical averaging over even several tens of thousands of trajectories, in order to e.g. properly determine small reaction probabilities of $\leq\sim 1\%$, are thus readily obtained today for (such) numerically convenient PESs, also for example as a function of initial kinetic energy and varying incidence angles [6].

While conceptually appealing, the practical bottleneck of this approach lies in the difficulty of procuring *and* assessing a reliable differentiable interpolation in high dimensions that are usually very closely intertwined [20]. Even when relying on the simplification of the frozen surface approximation and restricting the problem to only the internal degrees of freedom of a simple diatomic adsorbate, one is already faced with the far-from-trivial task of representing a continuous six-dimensional (6D) PES. With a number of high-dimensional interpolation techniques suggested and employed in the context of gas-surface dynamics (cf. for example Refs [77, 88–97]), we will focus here on the prevalent corrugation reducing procedure and neural networks. In the following, we therefore highlight conceptual and methodological features of these two state-of-the-art approaches which are of particular relevance to the present work for investigating the dynamics governing the adsorption of molecular oxygen at the Ag(100) and Pd(100) surfaces [20, 21].

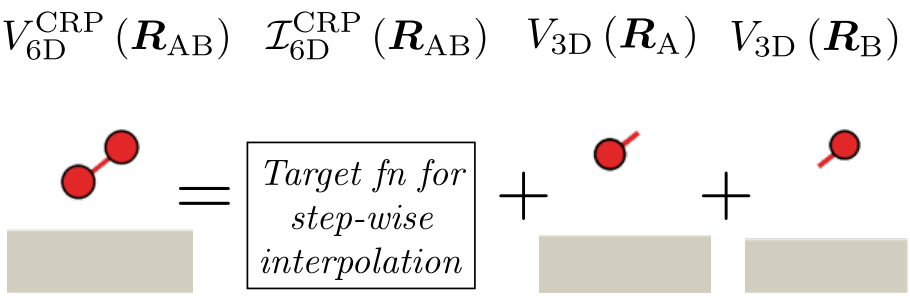

Figure 4.1.: Schematic illustration of the corrugation reducing procedure applied to the problem of continuously representing the six-dimensional interaction of a homonuclear diatomic adsorbate with a frozen surface. The full molecular PES V_{6D}^{CRP} is decomposed into a superposition of the individual (three-dimensional) atom-surface interactions V_{3D} and a smooth target function $\mathcal{I}_{6D}^{CRP}$ for the ensuing step-wise interpolation.

The difficulties beheld in a direct numerical interpolation of a 6D PES arise from the large energy variations connected e.g. with the strongly repulsive regions at short molecule-surface distances. In developping the corrugation reducing procedure (CRP) [88, 89], Busnengo and Salin relied on the notion that most of this corrugation is in fact already embedded in the repulsive wall individually encountered by each of the constituent adsorbate atoms as they approach the surface. The central idea of CRP therefore lies in decomposing the 6D molecular PES (V_{6D}^{CRP}) into a superposition of the 3D atom-surface interactions for both atoms (at their coordinates $\mathcal{R}_{A,B}$ in the diatomic) and a remaining smoother function ($\mathcal{I}_{6D}^{CRP}$):

$$V_{6D}^{CRP}(\mathcal{R}_{AB}) = \mathcal{I}_{6D}^{CRP}(\mathcal{R}_{AB}) + V_{3D}^{A}(\mathcal{R}_{A}) + V_{3D}^{B}(\mathcal{R}_{B}) \quad . \tag{4.1}$$

The scope of equation 4.1 thus lies in removing the high degree of corrugation from $\mathcal{I}_{6D}^{CRP}$ which then becomes a more convenient target for the 6D interpolation. In practice, this of course requires additional *ab initio* data for the construction of continuous atom-surface PES representations ($V_{3D}^{A,B}$), obviously simplifying to a single function in the case of a homonuclear diatomic. This constitutes, however, a much simpler task due to the lower 3D dimensionality and can straightforwardly be obtained through a direct interpolation with typical accuracies of <10 meV in absolute error [89]. The full CRP interpolation is then usually performed by decoupling the 6D problem into four at most 2D *independent* steps, where appropriate interpolation schemes are chosen according to generally expected energy variations in the respective degrees of freedom and carefully adapted to the symmetry of the latter [89]. Finally, once the full interpolation over $\mathcal{I}_{6D}^{CRP}$ has been carried out, the 3D atomic functions $V^{A,B}$ are invoked anew in order to recover the full 6D PES.

A neural network (NN) is instead inspired by neuroscience and can in general be described as a highly flexible, non-linear model that is in principal (based on a rigid mathematical proof) capable of approximating any continuous function to arbitrary accuracy [98, 99]. It consists of a number of artificial neurons or nodes that are interconnected via a set of links and typically arranged in layers: An input layer initially distributes the given information to the network where it is internally processed and re-distributed by one or more hidden layers until it is finally collected by the output layer and transformed into the returned data. The described architecture in which every node is connected to all nodes of the adjacent layer and information is transmitted only in one direction appoints a so-called multi-layer feed-forward neural network, as is schematically illustrated in Fig. 4.2.

The key attraction to performing a NN fitting lies in its inherent flexibility. In practice, the weights which are assigned to every node connection are optimized or 'trained' in order to best reproduce the given set of input data. Moreover, in each node a so-called activation function maps the summed input weights in a monotonic way to a certain output interval (typically between 0 and 1), thus activating the connected neuron to a certain amount. Different types of activation functions can be used in different layers and are usually denoted by 's' for sigmoid, 'l' for linear and 't' for hyperbolic tangent within the NN notation. In the meantime, bias weights act as an adjustable offset of the activation functions thereby further extending the network's flexibility.

As recently summarized in a review article by Handley and Popelier [100], Lorentz *et al.* were the first in 2004 to extend a NN application to the high-dimensional description of molecule-surface interactions [94]. In this context, the network is obviously trained to a set of input DFT data based on given atomic configuration vectors ($\boldsymbol{R}$), while the (single) output node returns a fitted PES value (V^{NN}). The latter is thus targeted directly and equally in e.g. its full six-dimensionality, allowing to capture intertwinement of degrees of freedom which are treated independently in the prevalent interpolation strategies hitherto employed in the CRP context described above. Further unlike the latter, the input data are not required to fall on regular grids, thus enabling the addition of individual points

depending on the desired accuracy in certain PES "regions" [20, 101]. Extrapolation capabilities of NNs beyond the coordinate ranges of the input data can also supersede those of the above described individual interpolations due to inherent limitations of the underlying fixed analytic forms. This inherent flexibility does, however, come as somewhat of a mixed blessing and renders an *a priori* knowledge of the investigated system all the more important both for choosing an appropriate set of weighted input data and for properly taking underlying symmetries into account.

Both the CRP and NN methodologies have met an overall remarkable sucess over a range of dynamical studies applied within the divide-and-conquer approach (cf. for example Refs [77, 88–90, 94–97]). Notwithstanding, one needs to recognize that their robustness remains severely limited by the problem's dimensionality and does not extend, at least in common practice application studies [102], as far as lifting of the frozen surface approximation. Corresponding divide-and-conquer studies have hitherto predominantly focused on light H_2 adsorbates for which an inherent neglect of substrate mobility may be somewhat justified. As already indicated in the previous section, however, a proper account of interfacial energy exchange may still be expected to play an eminent role in obtaining the correct dynamical behavior of heavier or more strongly chemisorbing adsorbates. In this respect, an effective treatment of substrate mobility that can be used to augment such simulations within a divide-and-conquer type approach become particularly appealing. Development of appropriate model bath Hamiltonians has thus been the subject of long-standing effort within the gas-surface dynamics community and will thereby represent the center of focus also in the following section.

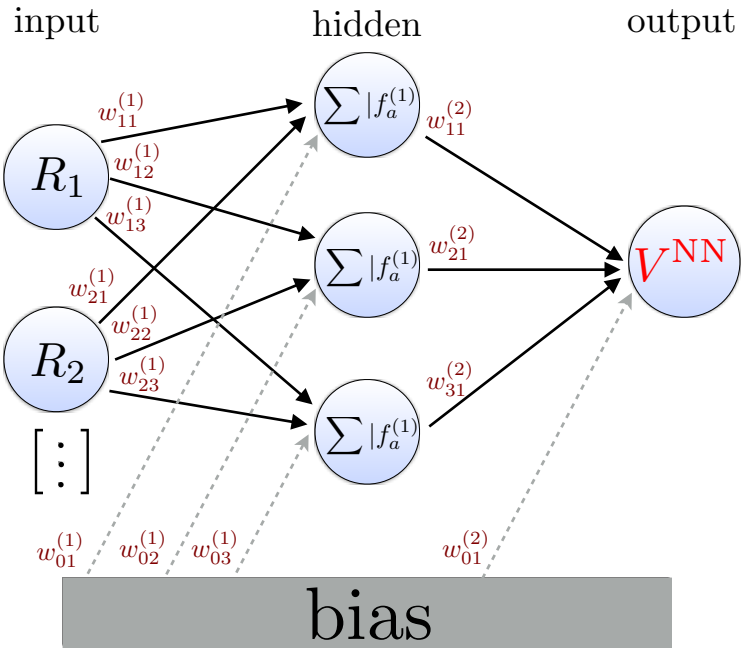

Figure 4.2.: Schematic illustration of a feed-forward neural network architecture. The specific design consists of two or more nodes in the input layer processing the input configuration vector ($R_{1,2,\ldots}$), a single hidden layer of three nodes, and one output node yielding the target potential energy function (V^{NN}). $\sum |f$ denotes the composition of the summation of weights w with an activation function f_α. A weight $w_{jk}^{(i)}$ is assigned to connections of nodes j and k between an adjacent pair of layers i.

5. Effective models of substrate mobility

Several different approaches (along with their numerous variations) have been proposed in the literature over the years in order to provide an effective heat sink for MD simulations in the context of gas-surface dynamics and thus account for some energy exchange with the lattice. Here, we will focus on the prevalent surface oscillator (SO) [79] and generalized Langevin oscillator (GLO) [80, 82, 83] models due to their particular relevance to the present thesis [21]. One of the main practical advantages of these approaches (exploited also in this work) is their convenient coupling to any pre-existing adsorbate-surface interaction potential that has already been obtained within the frozen surface approximation. This also includes of course the continuous DFT-based PES representations discussed in the previous section within the divide-and-conquer framework. MD simulations of an *ab initio* quality may thus straightforwardly, and with practically negligible computational overhead, be augmented with effective accounts of substrate mobility as these are provided on the SO and GLO levels of theory.

The SO is motivated by an Einstein-like model for the phononic system and aims to account for the effects of substrate mobility by a rigidly moving surface. In other words, the surface is simplistically mimicked by a single harmonic oscillator with assigned mass (m_{SO}) and frequency (ω_{SO}) parameters. The later naturally requires an appropriate tensorial representation ($\hat{\omega}_{\mathrm{SO}}$) if including three-dimensional Cartesian displacements $\boldsymbol{R}_{\mathrm{SO}} = (X_{\mathrm{SO}}, Y_{\mathrm{SO}}, Z_{\mathrm{SO}})$. Coupling to the adsorbate is then conveniently described through a space-rigid shift $\boldsymbol{R}_{\mathrm{SO}}$ in the potential describing its interaction with a frozen surface. For the case of a diatomic adsorbate and concomitant 6D PES representation (V_{6D}), the classical MD equations of motion in the SO approximation are thus given by:

$$\frac{\partial^2 \boldsymbol{R}_{\mathrm{A,B}}}{\partial t^2} = -\frac{1}{m_{\mathrm{A,B}}} \nabla_{\boldsymbol{R}_{\mathrm{A,B}}} V_{\mathrm{6D}}(\boldsymbol{R}_{\mathrm{A}} - \boldsymbol{R}_{\mathrm{SO}}; \boldsymbol{R}_{\mathrm{B}} - \boldsymbol{R}_{\mathrm{SO}}) \tag{4.1a}$$

$$\frac{\partial^2 \boldsymbol{R}_{\mathrm{SO}}}{\partial t^2} = -\frac{1}{m_{\mathrm{SO}}} \nabla_{\boldsymbol{R}_{\mathrm{SO}}} V_{\mathrm{6D}}(\boldsymbol{R}_{\mathrm{A}} - \boldsymbol{R}_{\mathrm{SO}}; \boldsymbol{R}_{\mathrm{B}} - \boldsymbol{R}_{\mathrm{SO}}) - \hat{\omega}_{\mathrm{SO}}^2 \cdot \boldsymbol{R}_{\mathrm{SO}} \quad , \tag{4.1b}$$

where $\mathrm{m}_{\mathrm{A/B}}$ and $\boldsymbol{R}_{\mathrm{A/B}}$ are the masses and Cartesian coordinates of the two individual adsorbate atoms A and B.

Extending on the latter, the GLO additionally incorporates the approximate effect of a bulk thermal bath. Here, the SO is coupled to a further 3D so-called ghost oscillator (m_{GLO}, $\hat{\omega}_{\mathrm{GLO}}$) through additional frequency parameters $\hat{\Lambda}_{\mathrm{SO-GLO}}$. The adsorbate is thereby only indirectly coupled to the thermal bath, while energy dissipation and thermal fluctuations are accounted for by subjecting the ghost oscillator to frictional and random forces, respectively. The latter represents a key step in the (mathematically rigorous) derivation of the equations underlying the GLO model: It significantly reduces the bath degrees of freedom, while effectively capturing the complexity of the corresponding many-body system through well-defined statistical properties. Physically, these properties are connected through a manifestation of the fluctuation-dissipation theorem which ensures that bulk dissipation is on average balanced by a back-flow of energy that allows to globally maintain the heat bath temperature T. The statistical treatment of the bath, however, comes at the price that individual trajectories lose their physical meaning, though still

stand correct in a stochastic sense even for systems which are far away from thermal equilibrium.

In order to make the GLO approach tractable in practice, suitable mathematical forms within some approximations are typically adopted for the friction and random force representations. As originally proposed by Adelman and Doll [80], the former is described through an isotropic and diagonal damping matrix $\hat{\gamma}_{\mathrm{GLO}} = \gamma_{GLO}\hat{\mathbf{1}} = \pi\omega_{\mathrm{D}}/6\,\hat{\mathbf{1}}$, where ω_{D} is the bulk Debye frequency. This simple friction coefficient can be related to the width σ of the Gaussian distribution G of the random force through:

$$\sigma = \frac{2k_{\mathrm{B}}T\gamma_{\mathrm{GLO}}}{m_{\mathrm{GLO}}\Delta t} \quad , \tag{5.2}$$

where k_B is the Boltzmann constant, and Δt is the discrete time interval used as a time-step in practical MD simulations. Extending on Eqs. 5.1 for the example of a diatomic adsorbate, the equations of motion within the GLO formalism can thereby be written as follows:

$$\frac{\partial^2 \boldsymbol{R}_{\mathrm{A,B}}}{\partial t^2} = -\frac{1}{m_{\mathrm{A,B}}}\nabla_{\boldsymbol{R}_{\mathrm{A,B}}} V_{6\mathrm{D}}(\boldsymbol{R}_{\mathrm{A}} - \boldsymbol{R}_{\mathrm{SO}}; \boldsymbol{R}_{\mathrm{B}} - \boldsymbol{R}_{\mathrm{SO}}) \tag{4.3a}$$

$$\frac{\partial^2 \boldsymbol{R}_{\mathrm{SO}}}{\partial t^2} = -\frac{1}{m_{\mathrm{SO}}}\nabla_{\boldsymbol{R}_{\mathrm{SO}}} V_{6\mathrm{D}}(\boldsymbol{R}_{\mathrm{A}} - \boldsymbol{R}_{\mathrm{SO}}; \boldsymbol{R}_{\mathrm{B}} - \boldsymbol{R}_{\mathrm{SO}}) - \hat{\omega}^2_{\mathrm{SO}} \cdot \boldsymbol{R}_{\mathrm{SO}} + \hat{\Lambda}_{\mathrm{SO-GLO}} \cdot \boldsymbol{R}_{\mathrm{GLO}} \tag{4.3b}$$

$$\frac{\partial^2 \boldsymbol{R}_{\mathrm{GLO}}}{\partial t^2} = -\hat{\omega}^2_{\mathrm{GLO}} \cdot \boldsymbol{R}_{\mathrm{GLO}} + \hat{\Lambda}_{\mathrm{SO-GLO}} \cdot \boldsymbol{R}_{\mathrm{SO}} - \hat{\gamma}_{\mathrm{GLO}}\frac{\partial \boldsymbol{R}_{\mathrm{GLO}}}{\partial t} + G(\Delta t) \quad . \tag{4.3c}$$

Despite the conceptual shortcomings and limitations (such as e.g. the implicitly assumed harmonic approximation), the models described above have overall been applied very successfully in quantifying macroscopic observables connected to surface adsorption and diffusion (e.g. Refs [81, 103–106]), also within a first-principles context [21, 84–86]. Particularly the latter renders them still highly relevant today when a fully quantitative account of phononic energy dissipation in explicit AIMD simulations remains highly demanding, when aiming for sufficient statistical averaging and the full computation of energy-dependent sticking curves. A major practical bottleneck still lies of course in the semi-empirical nature of these effective theories and the assumptions that have to be made with respect to the bath Hamiltonian. With very little generally known about adsorbate-surface or surface-bath coupling constants, rather crude descriptions represent the state of the art. The semi-phenomenological parameters (m_{SO}, $\hat{\omega}_{\mathrm{SO}}$) entering for example the ansatz of Eq. 5.1 are usually chosen based on the atomic masses of the surface atoms and experimentally determined vibrational properties, such as e.g. the Debye frequency of the corresponding bulk material [79]. Changes in these parameters by even orders of magnitude have nevertheless so far been found to have no significant influence on statistical properties (typically sticking or scattering probabilities) that have been studied [83–86]. While this may well find its cause in the inherent simplicity of these models, a higher sensitivity to the underlying phononic fine structure may nevertheless still be expected and can not be excluded from future studies to come. Early experimental work has, for example, already suggested a complex multi-phonon picture to govern the dynamics of the heavier (compared to H_2) NO at Ag(111) [107]. Generalizing the single-phonon approximation within common-practice applications of one (usually low-frequency) surface oscillation may thereby represent a highly dangerous over-simplification, in particular when going beyond prototypical studies of light atom/molecule scattering [108].

6. QM/Me: An embedding scheme for metals

The restrictions imposed within the divide-and-conquer ansatz do not apply to direct *ab initio* molecular dynamics (AIMD) simulations. In this method, the forces necessary to integrate the equations of motion are computed "on-the-fly" by first-principles electronic structure calculations, so that no fitting or interpolation of the PES is required. Substrate atoms are thereby treated explicitly and no *a priori* assumptions have to be made with respect to the heat bath Hamiltonian. For evaluating e.g. sticking probabilities of molecules at surfaces and for metals in particular, AIMD has only been scarcely applied in the past mainly because of the high computational effort connected with obtaining a sufficient amount of first-principles forces to propagate the system. Due to the continuous methodological developments and massive increase in computer power, this limitation is being steadily overcome and the situation is now changing [6].

Self-standing AIMD simulations remain, however, challenged in complementing the reliable quantum-mechanical description of surface chemical reactions with a fully quantitative account of phononic dissipation. Even at the limit of what is computationally tractable with present day resources, substrate mobility is only allowed within supercells and slab models that comprise a few surface lattice constants and layers. In contrast, a simple estimate of the phonon propagation distance in metals according to the respective speed of sound yields tens of lattice constants per picosecond in each direction. Corresponding dynamical studies will thereby suffer from an inadequate description of the phononic band structure and unphysical phonon reflections at the periodic boundaries of the employed supercell geometry. This unavoidably results in confining energy dissipation to the finite extent of the latter and would thus also falsify the picosecond-scale equilibration of the actual adsorbate dynamics. Current state-of-the-art AIMD simulations are thereby excluded from providing an accurate reference for the entire dynamical picture following e.g. an exothermic surface reaction, potentially also including the experimentally alluded intricate "hot" adatom motion.

In this situation, the recent development of the QM/Me simulation approach [109] is an important step forward. Within a multi-scale modeling philosophy, QM/Me augments the DFT-based quantum-mechanical (QM) description of the immediate reaction zone with a quantitative treatment of phononic dissipation into a numerically undemanding, yet appropriately described, extended metal (Me) heat bath. The originality of this methodology, in comparison to QM/MM (quantum-mechanics/ molecular-mechanics) embedding as routinely employed in e.g. biomolecular modeling [110–112], lies in avoiding the use of finite QM clusters. Embedding is instead performed within periodic boundary conditions, as is required to fully capture the delocalized metallic band structure and its crucial importance to adsorption. This is achieved by separating the chemical and elastic contributions in the QM interaction potential and leads to the following embedding ansatz for an atom

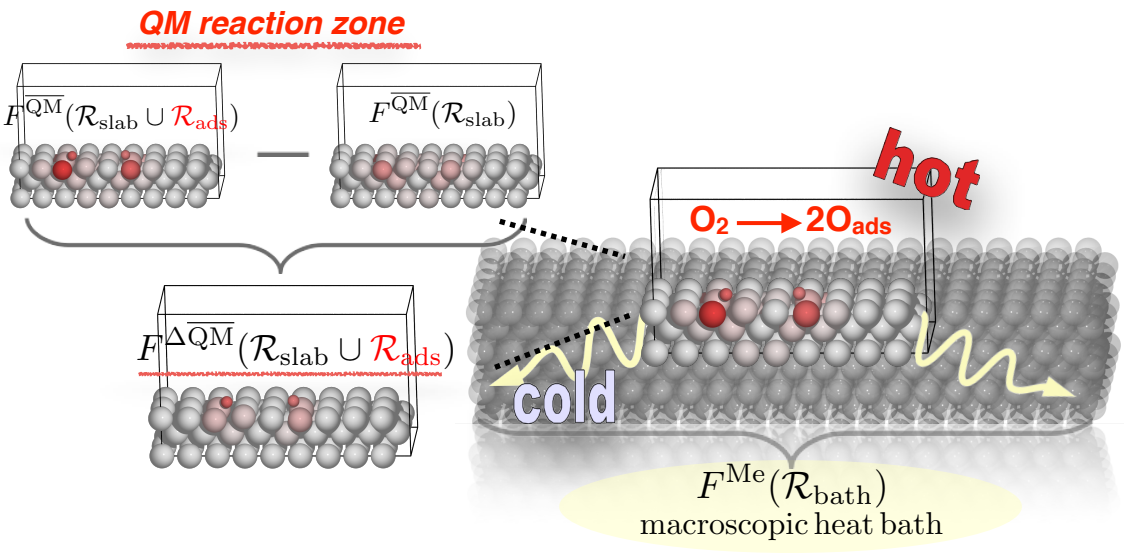

Figure 6.1.: Schematic illustration of the QM/Me embedding approach for metallic systems, as defined by Eq. 6.1. A quantum-mechanical (QM) description of the immediate reaction zone is obtained based on the periodic DFT supercell indicated in black. Treating the latter twice at the same level of theory provides the adsorbate-induced chemical contribution to the forces $F^{\Delta\overline{\mathrm{QM}}}$ which are sufficiently short-ranged to be well-contained within its finite extent. The elastic contribution to the forces $F^{\mathrm{Me}}(\mathcal{R}_{\mathrm{bath}})$ are subsequently obtained by embedding into an extended metal (Me) substrate that is treated at the level of a numerically efficient classical interatomic potential. Chemical energy released during the depicted (exothermic) dissociative oxygen adsorption is thus dissipated out of the "hot" reaction zone and into a "cold" macroscopic heat bath, while atoms in the embedding cell are color-coded according to forces calculated along a real QM/Me-AIMD trajectory for O_2 at Pd(100) [24].

at position $\mathcal{R}$:

$$V^{\mathrm{QM/Me}}(\mathcal{R}) = V^{\mathrm{Me}}(\mathcal{R}_{\mathrm{bath}}) + \underbrace{\left[E^{\overline{\mathrm{QM}}}(\mathcal{R}_{\mathrm{slab}} \cup \mathcal{R}_{\mathrm{ads}}) - E^{\overline{\mathrm{QM}}}(\mathcal{R}_{\mathrm{slab}})\right]}_{V^{\Delta\overline{\mathrm{QM}}}(\mathcal{R}_{\mathrm{slab}} \cup \mathcal{R}_{\mathrm{ads}})} , \tag{6.1}$$

where the coordinate sets $\mathcal{R}_{\mathrm{bath}}$, $\mathcal{R}_{\mathrm{slab}}$, and $\mathcal{R}_{\mathrm{ads}}$ correspond to all metals atoms in the environment of the adsorbate, metal atoms in the embedded QM supercell, and adsorbate atoms respectively.

Equation 6.1 defines $V^{\Delta\overline{\mathrm{QM}}}$ as the specific chemical adsorbate-substrate and adsorbate-adsorbate interactions. It is obtained in practice from two successive DFT calculations within identical periodic supercells: The first includes the adsorbate atoms and the second excludes them, while in both cases the positions of the substrate metal atoms ($\mathcal{R}_{\mathrm{slab}}$) remain unchanged. Forming the difference of these calculations thus cancels contributions of elastic interactions in the QM potential and leaves only the adsorbate-induced chemical interactions. The latter are sufficiently short-ranged to be well contained within the finite extent of computationally tractable DFT embedding cells. Even though calculated within periodic boundary conditions, $V^{\Delta\overline{\mathrm{QM}}}$ extends thus only over a finite region.

V^{Me} then provides the missing elastic contributions from substrate-substrate interactions due to lattice deformations which occur with the progressing chemical reaction. For metallic systems these elastic interactions are long-ranged [113, 114], as exemplified by

the slow decrease of the pairwise contributions as some inverse power of inter-atomic distance [115]. They are nevertheless already accurately described by many-body classical interatomic potentials, the numerical efficiency of which allows for modeling an extended MM heat bath region (cf. section 2). Several tens of thousands metal bath atoms can thus easily be included in the simulation without the evaluation of V^{Me} becoming a computational bottleneck, thereby providing a realistic description of the substrate's phononic fine structure and further ensuring that phonon propagation will not reach the boundaries of the employed simulation boxes even on a picosecond-timescale.

There is of course no conceptual limitation to stop the above methodology from being extended to include the concurrent treatment of *multiple* DFT-described reaction zones. This has in fact already been implemented in the context of this thesis and for the present purposes of following the dynamics of a single dissociative event. The specific implementation is therefore designed to substitute an initial (typically larger) embedding cell by two (or more) such cells after dissociation has taken place and substrate-mediated interactions between the reaction partners have largely vanished. The resulting "hot" embedding regions are thus centered around the individual dissociation fragments and can dynamically follow their motion over the surface. Independent treatment on the DFT level thus ensures that unphysical interactions through periodic images are suppressed, while additionally allowing to use smaller supercells and thereby introducing an efficiency gain according to the non-linear scaling of the underlying calculations. Most importantly, however, it provides the flexibility that enables application to chemical reactions for which the lateral direction of "hot" translational motion is not *a priori* clear.

The QM/Me methodology overall bears principal similarities to the ONIOM scheme of Morokuma and coworkers [116], but specifically targets forces rather than the energy function. This difference specifically exploits the short-ranged nature of $V^{\Delta\overline{\mathrm{QM}}}$ in order to avoid boundary effects and yield a QM many-body description that fully captures the chemistry of bond breaking and making. "Embedding" $V^{\Delta\overline{\mathrm{QM}}}$ in V^{Me} through Eq. 6.1 can thus complement first-principles based dynamical simulations of chemical reactions at metal surfaces with an explicit account of energy dissipation into an atomically-resolved MM heat bath. It is exactly this atomic resolution that allows for unraveling important mechanistic details of the energy conversion process, through a detailed mode-specific analysis of the underlying phononic excitations as described in the following section.

7. Projecting onto phonons

Fundamental research on the atomistic details of thermal transport has a long-standing history, partly triggered by industrial interest in e.g. heat management for electronic devices and thermal coatings. Phonon transport properties in crystalline materials are studied computationally using either lattice dynamics calculations or molecular dynamics (MD) simulations. In the context of the former, theoretical formulations for determining a solid's vibrational properties from perturbation theory have been known for quite some time [117]. Reliable quantitative evaluations, however, require accurate energies and polarizations for all phonons, as well as accurate anharmonic force constants. Anharmonicities in the atomic interactions specifically represent three- and higher-order phonon processes, and their (exact) inclusion is thus necessary for e.g. predicting thermal expansion, arriving at a finite thermal conductivity in perfect crystals, or following the evolution of non-equilibrium excitations toward the ground state [118]. First-principles interatomic force constants may of course directly be obtained from density functional perturbation theory (DFPT) [119–121] or from finite differences through the so-called frozen phonon method [122]. Such calculations, however, come at a staggering computational cost which also excludes their application in the present context of a macroscopic heat bath incorporating several tens of thousands metal atoms.

On the other hand, lattice dynamics based on more attractive classical interatomic potentials nevertheless require that the anharmonic force constants be explicitly included in the calculations. Due to a general lack of microscopic understanding with respect to multi-phonon interactions, this represents (even for three-phonon interactions) a far-from-trivial task. In most cases, theoretical predictions thus rely either on a direct fitting to experimental data [123], or on crude models that are generally consistent with empirical anharmonic parameters [124] (related to e.g. elasticity or thermal expansion). Although simple and often effective, such approaches are thereby inevitably restricted by the availability/quality of the employed input parameters and tend to exhibit limited predictive power beyond the range of cases included in the fitting procedure.

Extracting phononic information from MD simulations requires instead no *a priori* assumptions regarding the nature of thermal transport or any further input, apart from the equilibrium atomic positions and an appropriate (anharmonic) interatomic potential. Here the commonly followed recipe dictates computation of the velocity (or displacement) autocorrelation functions in order to arrive at an occupied density of phonon states, from which then also mode-resolved lifetimes can subsequently be extracted [125]. The practical bottleneck of this approach, however, lies in the requirement for extensive statistical sampling which in turn prohibits its application to computationally demanding PES descriptions or large system sizes such as the ones required here.

In the following, we describe an alternative approach towards quantitatively assessing phonon populations from MD simulations by making use of a (mathematically) rigorous mode-resolved phonon decomposition. The latter is rendered suitable for instantaneous application at any given time-step along a dynamical trajectory, thus eliminating the need for averaging over time. This already offers a prodigious advantage over methods that rely on time autocorrelation functions, in particular within first-principles based approaches for which a fully quantitative phonon analysis has thus far remained impractical

or even impossible (cf. for example Refs [126–128]). It is thereby also ideally suited to the present context of gas-surface dynamics where the breaking and making of chemical bonds specifically warrant the need for computationally expensive DFT evaluations at each MD time-step. Further relying on incorporating the description of an atomically-resolved macroscopic heat bath, as can be achieved through the QM/Me Hamiltonian (Eq. 6.1) described in the previous section, provides here an unprecedent quantitative treatment of the non-equilibrium adsorbate-phonon dynamics [24, 25]. The remaining challenge then only lies in making contact with the phonon dispersion relation in order to identify the nature of excited modes through their actual wave vector, while in the meantime circumventing the computationally formidable task of diagonalizing the dynamical matrix of a heat bath region that contains in excess of hundred thousand atoms.

We achieve this on the basis of a projection methodology that allows to represent the complex atomic displacement pattern of atoms in a large supercell region as a superposition of the normal mode displacement eigenvectors that belong to a periodic primitive cell. Phonons realized in different branches at the Γ-point in the small Brillouin zone of the supercell are thus effectively back-folded into the (larger) Brillouin zone corresponding to the chosen primitive unit. The rigorous formulation of this projection scheme was originally laid out by McGaughey and Kaviany for the monatomic ($N_{\mathrm{cell}} = 1$) bulk primitive cell of Lennard-Jones model crystals [123]. It can, of course, in principle be generalized accordingly to any problem involving "phononic details" beyond the Γ-point by employing arbitrarily large supercells of a repeating primitive unit in any number of periodic directions. For the present application on a two-dimensional slab model we thus appropriately extend it here to a polyatomic primitive cell ($N_{\mathrm{cell}} > 1$) that extends over a sufficient number of slab layers (N_{layers}), a detailed derivation of which may be found in Ref. [109]. The latter specifically contains a single atom per layer for the low-index fcc surfaces investigated in this thesis ($N_{\mathrm{cell}} = N_{\mathrm{layers}}$), while an arbitrarily large supercell can then be constructed by ($N_1 \times N_2$) repetitions in the lateral periodic directions.

The starting point is then the atomic displacement field of the bath supercell containing $N_{\mathrm{supercell}}$ ($\equiv N_1 \times N_2 \times N_{\mathrm{layers}}$) atoms. This displacement field is described in the $3N_{\mathrm{supercell}}$-dimensional vector $\boldsymbol{U}^{\mathrm{MD}}(t)$ that denotes the Cartesian displacements with respect to the equilibrium positions $\boldsymbol{R}^0$ at a given time t during the MD simulation. The vector is defined on the real-space lattice grid $\boldsymbol{L}_n$ of the atomic positions and can be transformed onto the corresponding reciprocal grid $\boldsymbol{q}_n$ of exact phonon wave vectors by means of a discrete two-dimensional spatial Fourier transform:

$$U^{\mathrm{MD}}_{\tilde{I}_\alpha}(\boldsymbol{L}_n; t) = \frac{1}{\sqrt{N_1 N_2}} \frac{1}{\sqrt{M_{\tilde{I}}}} \sum_{\boldsymbol{q}_{n'}}^{\mathrm{grid}} \left(\sum_{b'=1}^{3N_{\mathrm{layers}}} C(\boldsymbol{q}_{n'}, b'; t) \hat{u}_{\tilde{I}_\alpha}(\boldsymbol{q}_{n'}, b') \right) \mathrm{e}^{i \boldsymbol{q}_{n'} \cdot \boldsymbol{L}_n} \quad . \tag{7.1}$$

The transformation is performed component-wise with Cartesian vector coordinates $\alpha = (x, y, z)$, and for every atom in the supercell. The latter are indexed by a number $\tilde{I}$ in the primitive cell (denoting here the specific slab layer) and a two-dimensional lattice vector $\boldsymbol{L}$ leading to the desired periodic image (n) in the lateral directions. At every point $\boldsymbol{q}_{n'}$ the phonon mode expansion coefficients $C(\boldsymbol{q}_{n'}, b'; t)$, which are the key quantities of interest here, are represented in the orthonormalized basis of generally complex-valued displacement eigenvectors $\{\hat{u}_{\tilde{I}_\alpha}(\boldsymbol{q}_{n'}, b')\}_{b'} \subset \mathbb{C}^{3N_{\mathrm{layers}}}$, where b' is the phonon band index. Similar to normal modes in non-periodic systems, more complex displacement patterns can be described by superpositions of the eigenvector solutions which can be individually viewed as "Fourier modes". In fact, a truly macroscopic solid (obtained at infinite supercell sizes) practically allows for infinitely large wavelengths $\lambda = 2\pi/\|\boldsymbol{q}\|$ and thus leads to continuous wave vectors $\boldsymbol{q}$. Finally, masses ($M_{\tilde{I}}$) are separated out of the latter which are therewith given in mass-weighted coordinates as is the common convention in lattice

dynamics.

As already indicated above, here $\boldsymbol{q}$-points of the reciprocal-space grid are chosen such that the two-dimensional periodicity of the phonons is commensurate with the chosen supercell and hence described exactly. Making use of the orthonormality relations for both the discrete Fourier transform and the displacement eigenvectors greatly simplifies the task of obtaining the target $C(\boldsymbol{q}_n, b; t)$ from Eq. 7.1 and leads to the following ansatz:

$$C(\mathbf{q}_n, b; t) = \frac{1}{\sqrt{N_1 N_2}} \sum_{n}^{N_1 \times N_2} \sum_{\tilde{I}}^{N_{\text{layers}}} \sqrt{M_{\tilde{I}}} [\hat{\mathbf{u}}_{\tilde{I}}(\mathbf{q}_n, b)]^* \cdot U^{\text{MD}}_{n\tilde{I}}(t) \mathrm{e}^{-i\mathbf{q}_n \cdot (\mathbf{R}^0_{n\tilde{I}} - \mathbf{R}^0_{\tilde{I}})} \quad , \tag{7.2}$$

where the double-index $n\tilde{I}$ iterates over all $N_{\text{supercell}}$ atoms in the supercell region. The target phonon mode expansion coefficients then depend on time only through the real-space displacement field ($U^{\text{MD}}_{n\tilde{I}}$), which can be straightforwardly obtained at any time-step of a given MD trajectory.

Following the same decomposition of Eq. 7.1 and the ensuing formalism also for the velocity field $\dot{\boldsymbol{U}}^{\text{MD}}(t)$ yields corresponding velocity expansion coefficients $\dot{C}(\boldsymbol{q}_n, b; t)$. Under the harmonic approximation, the total energy of a single phonon mode can then be expressed as

$$\begin{aligned} \varepsilon^{\text{ph}}(\boldsymbol{q}_n, b; t) &= \varepsilon^{\text{ph}}_{\text{kin}}(\boldsymbol{q}_n, b; t) + \varepsilon^{\text{ph}}_{\text{pot}}(\boldsymbol{q}_n, b; t) \\ &= \frac{1}{2} |\dot{C}(\boldsymbol{q}_n, b; t)|^2 + \frac{1}{2} \omega^2(\boldsymbol{q}_n, b) |C(\boldsymbol{q}_n, b; t)|^2 \quad , \end{aligned} \tag{7.3}$$

where the two terms correspond to the kinetic and (harmonic) potential energy of the corresponding mode with frequency ω. To the extent that the harmonic approximation holds, Eq. 7.3 then forms the foundation for quantifying also the total phononic energy uptake:

$$E^{\text{ph}}_{\text{tot}}(t) = \sum_{\boldsymbol{q}_n}^{\text{grid}} \sum_{b=1}^{3N_{\text{layers}}} \varepsilon^{\text{ph}}(\boldsymbol{q}_n, b; t) \quad . \tag{7.4}$$

Energy resolved excitation spectra can thus be calculated "on the fly" through a straightforward discretization of Eq. (7.3) along the phonon energy ($\hbar\omega$) axis. While this greatly simplifies visualization, it is still the mode selectivity naturally provided by the underlying formalism that allows to focus on certain groups of modes. In the present context of gas-surface dynamics, such an analysis therefore allows for identifying the dominant energy dissipation channels [24, 25], while offering a first-principles perspective on parameters entering effective models of substrate mobility such as the prevalent surface oscillator and generalized Langevin oscillator methodologies discussed in section 5.

Part II.

Paper Summaries & Contributions

1. Ready, Set and no Action: A Static Perspective on Potential Energy Surfaces commonly used in Gas-Surface Dynamics

Authors: V. J. Bukas, J. Meyer, M. Alducin and K. Reuter.
Published in Zeitschrift für Physikalische Chemie, Volume 227, Issue 9–11, Pages 1523–1542, ISSN (Online) 2196–7156, ISSN (Print) 0942–9352, August 2013
DOI: 10.1524/zpch.2013.0410

Summary:

We review and assess continuous potential energy surface (PES) representations commonly used in gas-surface dynamics. Relying on the Born-Oppenheimer and frozen surface approximations, the energetics of O_2 adsorbing at Ag(100) are used as a showcase system to highlight the complex landscape often met in such PESs even when explicitly considering only the internal degrees of freedom of a diatomic adsorbate. With the latter being very closely intertwined, the far-from-trivial task of procuring and assessing a reliable high-dimensional interpolation is put here into focus. Employing the exact same set of *ab initio* reference data obtained within density functional theory (DFT), we construct different O_2/Ag(100) PES representations based on two state-of-the-art interpolation approaches, namely the corrugation reducing procedure (CRP) and neural networks (NN). Despite both representations flawlessly passing the typical reliability checks performed to assess the interpolation quality, we show them yielding notably different reaction probabilities for the dissociation of molecular oxygen in the low coverage regime. A thorough investigation into the global energetics and extensive configurational sampling for low-lying PES minima rationalizes this discrepancy by identifying representation deficiencies which affect the dynamical picture yet go otherwise unnoticed within the so-called "divide-and-conquer" approach. With the issue of interpolation reliability thus accentuated, we generally suggest to perform *a priori* static PES examinations while focusing on prominent topological features for iteratively refining the DFT input data grid.

Individual contributions:

This work was carried out in collaboration with Dr. Maite Alducin from the Centro de Física de Materiales (CFM) in San Sebastián. Dr. Alducin provided the DFT data [129] on which this work is based on. Dr. Jörg Meyer (who is currently an associate professor at the Leiden Institute of Chemistry) and Prof. Dr. Karsten Reuter closely supervised the project and played a significant part in co-writing/editing the manuscript. Dr. Meyer contributed particularly with substantial technical support and computational tools, including his implementation of the symmetry adapted coordinates. Dr. Jörg Behler (Ruhr–Universität,

Bochum) and Dr. Fabio Heriberto Busnengo (Instituto de Física, Rosario) provided their (Fortran) NN and CRP implementations, respectively.

I interfaced (employing the robust F2PY package) and accordingly modified the aforementioned tools for the present purposes of constructing two continuous O_2/Ag(100) PES representations as a function of all six molecular degrees of freedom. A new, convenient Python package was thus set up for evaluating the resulting representations and performing back-and-forth transformations between Cartesian and spherical coordinates. The latter turned out to be crucial for the ensuing analysis which I performed based on self-written Python routines while making extensive use of the powerful NumPy and SciPy scientific libraries. The same holds for collecting and post-processing the data generated from the extensive (quasi-classical) dynamical simulations in order to scrutinize the underlying mechanistic details and extract the presented sticking curves. I developed the scheme to globally search the PES for local minima after loosely interfacing with the Atomic Simulation Environment (ASE) [130] and its implementation of the BFGS optimization algorithm. Plotting, graphic and visualization purposes were served primarily by the user-friendly, yet highly flexible, Python-powered matplotlib package.

2. Fingerprints of energy dissipation for exothermic surface chemical reactions: O_2 on Pd(100)

Authors: V. J. Bukas, S. Mitra, J. Meyer and K. Reuter.
Published in The Journal of Chemical Physics, Volume 143, Issue 3, Eid 034705, July 2015
DOI: 10.1063/1.4926989

Summary:

Despite its progress, state-of-the-art quantitative modeling in the field of gas-surface dynamics still faces considerable challenges when it comes to faithfully reproducing experimental data. We find such a discrepancy upon comparing measured sticking curves for O_2 on Pd(100) [22] with our first-principles results. Within the latter approach, we perform molecular dynamics simulations on a neural network (NN) interpolated potential derived from density functional theory (DFT) and accounting for all six molecular degrees of freedom. Suspecting as source for the discrepancy the prevalent frozen surface (FS) approximation underlying this approach, we extend our model to additionally include surface mobility in the form of a surface oscillator (SO), and a generalized Langevin oscillator (GLO). While even a simple SO model already qualitatively changes the dynamical picture, similarly good agreement with experiment is reached at the GLO level based on two different semi-local DFT functionals (PBE and RPBE). This robustness of the simulated sticking curve does not extend to the underlying adsorption mechanism, which is predominantly directly dissociative for one functional or molecularly trapped for the other. Our results thus overall underscore the importance of overcoming the FS approximation for adsorbates heavier than the prototypical H_2, while highlighting the danger of the prevalent practice to extract corresponding mechanistic details from simple fingerprints of measured sticking data for such exothermic surface reactions.

Individual contributions:

This work was partly carried out in the context of Shubhrajyoti Mitra's MSc thesis which was performed at the Chair for Theoretical Chemistry of the TU Munich under my direct supervision. Shubhrajyoti Mitra performed the extensive DFT-RPBE calculations in order to construct the corresponding continuous PES representation. He evaluated the fitting quality and made a thorough static investigation into the global energetics. Dr. Jörg Meyer (who is currently an associate professor at the Leiden Institute of Chemistry) provided the DFT-PBE PES representation and supervised the first steps of this work. Prof. Dr. Karsten Reuter closely supervised the project during its entire course and played a significant part in co-writing/editing the manuscript. Dr. Jörg Behler (Ruhr–Universität, Bochum) and Dr. Fabio Heriberto Busnengo (Instituto de Física, Rosario) provided their (Fortran) NN and SO, GLO implementations, respectively.

Based on a convenient Python package, I interfaced (employing F2PY wrapping) and accordingly modified the aforementioned tools for the present purposes of performing classical dynamical simulations on the FS, SO, and GLO levels of theory. Extensive sampling was thus performed for each model and on both the DFT-PBE and DFT-RPBE PES representations, while including different initial O_2 translational energies, incidence angles, and surface temperatures. I collected and analyzed the generated data using self-written Python routines (while making extensive use of the powerful NumPy and SciPy scientific libraries) in order to scrutinize the underlying mechanistic details and extract the presented sticking curves. Plotting, graphic and visualization purposes were again served primarily by the user-friendly, yet highly flexible, Python-powered matplotlib package.

3. Hot Adatom Diffusion Following Oxygen Dissociation on Pd(100) and Pd(111): A First-Principles Study of the Equilibration Dynamics of Exothermic Surface Reactions

Authors: V. J. Bukas and K. Reuter.
Published in Physical Review Letters, Volume 117, Issue 14, Pages 146101–146106, September 2016
DOI: 10.1103/PhysRevLett.117.146101

Summary:

We augment *ab initio* molecular dynamics (AIMD) simulations with a quantitative account of phononic dissipation in order to study the highly non-equilibrium aftermath of exothermic surface reactions. We employ a novel embedding scheme for metallic substrates (QM/Me [23, 109]) which allows for energy to be dissipated out of a quantum-mechanically described reaction zone and into a computationally undemanding, yet reliably described, extended bath. In a first application to oxygen dissociation over Pd(100) this approach predicted "hot" O adatoms traveling ballistically over several lattice constants as a consequence of non-immediate energy transfer to the surface. Despite being similarly exothermic, much shorter O-O end distances were measured for the O_2/Pd(111) reaction [10] which might straightforwardly imply a shorter lifetime for the hyperthermal state. We reconcile this apparent intricacy by quantifying phononic dissipation at the (111) as compared to the (100) surface directly from QM/Me trajectories. This reveals in fact a much slower equilibration on Pd(111) with the experimentally predicted small net displacements resulting instead from a random-walk type diffusion. A detailed phonon analysis rationalizes the slow equilibration through long-lived Rayleigh mode excitations that spatially confine the released energy within a nanoscopic "hot spot" around the O_2 impingement region. We therefore show that experimentally accessible product end distances, which have thus far served as the sole measure for hyperthermal diffusion, may be highly misleading. Our results suggest that transient surface mobility might be more common than hitherto anticipated, with further paradigm shifts possibly required to accommodate such "hot chemistry" in our current understanding of heterogeneous catalysis.

Individual contributions:

The present work was carried out under the close supervision of Prof. Dr. Karsten Reuter, who also played a significant part in co-writing/editing the manuscript. I implemented QM/Me by loosely interfacing calculations performed independently on the levels

of density functional theory (DFT) and the classical modified embedded atom method (MEAM) [33]. Extending on the Atomic Simulation Environment (ASE) [130] served in properly communicating the coordinate and force sets obtained at the two levels of theory in order to collect the necessary ingredients for applying the QM/Me ansatz. High performance computing (HPC) resources that were generously provided by the Leibniz Rechenzentrum (LRZ) der Bayerischen Akademie der Wissenschaften (project pr85wa) enabled the formidable task of obtaining the required DFT forces at each time-step of our AIMD simulations. I thus conducted the latter on the LRZ supercomputer "SuperMUC", while heavily relying on the provided infrastructure and efficient parallel performance. The large output files containing all generated phase-space trajectory information were analyzed by self-written Python routines, while making extensive use of the ASE in-built utilities for both post-processing and visualizaton purposes. The same holds for creating movies of the O_2/Pd(100) and O_2/Pd(111) trajectories which are electronically made available as supporting material alongside the published manuscript, while graphics and plotting were created using Inkscape software and the Python-powered matplotlib package.

4. Phononic dissipation during "hot" adatom motion: A QM/Me study of O_2 dissociation at Pd surfaces

Authors: V. J. Bukas and K. Reuter.
Submitted for publication to The Journal of Chemical Physics, September 2016

Summary:

Exothermic surface chemical reactions may release several electron volts of energy. This challenges first-principles based dynamical simulations to account for adequate dissipation channels, the miscroscopic details of which remain to a large extent unresolved. Focusing here on phononic dissipation, we use the recently developed QM/Me embedding scheme [23] which offers the possibility of unraveling these details from the perspective of predictive-quality *ab initio* molecular dynamics (AIMD). We focus specifically on analyzing the role of substrate symmetry and compare the equilibration dynamics ensuing O_2 dissociation at all low-index (110), (100) and (111) Pd facets. In all cases the released reaction energy decays to the Pd substrate on a picosecond timescale, i.e. it is not instantaneous on the timescale of the actual dissociation dynamics. Despite the similarly high exothermicity of the dissociative reactions and barriers for atomic diffusion, however, we find a striking difference in the degree of hyperthermal mobility for the resulting O adatoms, i.e. they remain translationally "hot" for shorter or longer periods of time. Quantifying phononic dissipation directly from QM/Me-AIMD trajectories relates the latter to intrinsically different rates of interfacial energy exchange on the three surfaces. A detailed phonon analysis rationalizes these results by identifying dominant dissipation channels as excitations of specific groups of localized surface modes that do not necessarily lie at the lower energy end of the phononic spectrum. The thus obtained first-principles perspective on non-equilibrium adsorbate-phonon dynamics thereby underscores the sensitive dependence on details of the phononic fine structure, while questioning prevalent assumptions about energy sinks made in commonly used model bath Hamiltonians (cf. for example Refs. [26–29] and references therein).

Individual contributions:

The present work was carried out under the close supervision of Prof. Dr. Karsten Reuter, who also played a significant part in co-writing/editing the manuscript. Relying on High performance computing (HPC) resources that were generously provided by the Leibniz Rechenzentrum (LRZ) der Bayerischen Akademie der Wissenschaften on the "SuperMUC" supercomputer (project pr85wa), I performed the static stand-alone density functional Theory (DFT) calculations described in the manuscript for investigating oxygen's adsorption energetics on the three Pd(110), Pd(100), and Pd(111) surfaces. The ensuing AIMD simulations were thereafter performed and analyzed by employing the ex-

isting QM/Me implementation [24] and post-processing tools. Phonon band structures and densities of states (DOS) were calculated after loosely interfacing to the "Phonon" class of the Atomic Simulation Environment [130] and modifying the code accordingly for the present purposes of identifying and quantifying the corresponding contribution of surface modes. I developed and implemented the phonon projection scheme independently through self-written Python routines, while making extensive use of the powerful NumPy and SciPy scientific libraries. The computational task of applying this scheme at each time step of the obtained QM/Me-AIMD trajectories was distributed over several tens of SuperMUC processes for simultaneous serial evaluation. Graphics and plotting were once again created using Inkscape software and the Python-powered matplotlib package.

5. A comparative study of oxygen adsorption at Pd surfaces from Density Functional Theory

Authors: V. J. Bukas and K. Reuter.
Submitted for publication to Surface Science, October 2016

Summary:

Fundamental understanding of the bonding interactions that take place at a surface lies at the heart of all surface chemistry phenomena. As such, the study of atomic or molecular adsorption at transition metal surfaces in particular has long been a vivid area of research; nurtured also by its high industrial relevance in oxidation catalysis and the formation of technologically important metal oxides. Density functional theory (DFT) in particular has largely contributed towards establishing the microscopic understanding that we have today, while corresponding calculations for surface adsorption have matured immensely over the last two or three decades [3, 30]. Focusing here on a systematic comparison with respect to surface symmetry, we present a detailed DFT investigation into the first steps of atomic oxygen chemisorption at all three low-index Pd facets. This thus complements previous studies that focus on the trends in O adsorption within one particular surface orientation over different coverages [131, 132]. We specifically address and provide consistent data, within a uniform computational framework, for adsorption geometries, energies, work functions, and electron densities. This allows for obtaining consistent insight, and hence discerning trends, also with respect to the more subtle aspects involved in the chemisorption thermodynamics. We overall find notable O-Pd hybridization that is accompanied by minimal charge transfer from the substrate to the adsorbate. This similarity persists at different Pd facets and results in comparable binding energies for optimal O adsorption and similarly modest barriers for atomic diffusion. Subtle differences in the electronic structure are nevertheless still discernible and reflect the increasing trend in reactivity from Pd(111), over Pd(110), to Pd(100); a sequence that does not follow the order according to atom packing density due to pronounced surface relaxation effects at the open Pd(110) surface in particular.

Individual contributions:

The present work was carried out under the close supervision of Prof. Dr. Karsten Reuter, who also played a significant part in co-writing/editing the manuscript. Relying on High performance computing (HPC) resources that were generously provided by the Leibniz Rechenzentrum (LRZ) der Bayerischen Akademie der Wissenschaften on the "SuperMUC" supercomputer (project pr85wa), I performed all density functional Theory (DFT) calculations described in the manuscript for investigating the on-surface adsorption of atomic oxygen at all three Pd facets. This was accompanied by thorough bench-marking

and consistent checks with respect to the employed computational settings and technical parameters. I specifically employed self-written Python routines in combination with the in-code tools of the all-electron FHI-aims code [46] for analyzing the electronic structure and determining the position of the metal d band centers. Structure evaluations, vibrational analyses, and the determination of minimum energy paths were additionally supported by the Atomic Simulation Environment (ASE) [130]. Graphics and plotting were created using the Inkscape software, atomic structure viewers provided by Jmol and the ASE, and the Python-powered matplotlib package.

Conclusions & Outlook

In summary, the present thesis employs first-principles based MD simulations to investigate catalytically relevant surface reactions and the ensuing adsorbate thermalization. Considering the several eVs of energy that may easily be released during such processes, particular focus is put on a quantitative account of the dissipative dynamics within an accurate description of substrate phonon excitations. As the question of energy dissipation directly interfaces with the efficiency of converting chemical energy, the present research interests extend increasingly into sustainability at the larger scale.

Ultimately going beyond present limitations imposed by small simulation cells or assumptions commonly implied by system-bath coupling Hamiltonians, the novel QM/Me scheme offers novel qualitative insights into the microscopic details of phononic dissipation. Our results show a strong dependence on the underlying surface symmetry, while suggesting that hyperthermal surface diffusion might be more common than hitherto anticipated. This prediction has ground-shaking consequences for microkinetic models of surface catalysis where the elementary reaction steps of adsorption and diffusion are treated as two decoupled, statistically unrelated elementary processes [14, 15]. The underlying Markovian state-to-state hopping, which is questioned here from a first-principles perspective, may thereby easily introduce an error of several orders of magnitude in the calculation of diffusion rates. Should reactions with other adsorbates in the vicinity of the original impingement point also be stimulated this way, further paradigm shifts would be required to accommodate such "hot" chemistry, for example, in our current understanding of heterogeneous catalysis [23].

QM/Me will enable to address these aspects in systematic future studies, and also scrutinize the potential role of "hot" adatoms in other import dynamical processes such as the self-assembly of surface nanostructures, the first steps of oxide nucleation and epitaxial growth, or adsorbate-induced surface reconstructions. Allowing now also for finally reaching a detailed atomistic understanding with respect to the influence of surface temperature, corresponding QM/Me studies will establish important trends for yet more complex systems and elucidate experimentally proposed microscopic mechanisms. In this respect, a particularly interesting application is the dissociative oxygen adsorption at Ag(100), where scanning-tunneling micrsoscopy measurements have suggested an exceptional far-ranged adatom mobility of 7 or 14 surface lattice constants [11–13]. We expect here a key role to be played by the dynamically adapted embedding cells which have also been developed in the context of the present thesis, thereby additionally enabling the straightforward application to multiple "hot" reaction zones which can follow the adatoms 'wherever they go'.

Finally, efforts are already underway to apply QM/Me also within an electronically nonadiabatic context. We augment the phononic dissipation channel with electronic damping based on the local density friction approximation (LDFA) [133, 134] and employing a state-of-the-art atoms-in-molecules (AIM) charge partinioning scheme [135] to additionally account for intramolecular contributions. The efficiency of obtaining LDFA-AIM friction coefficients is particularly appealing as it adds only a slight computational overhead to direct AIMD simulations which can be easily addressed with present-day resources. Our proposed scheme will thereby finally allow for a statistically meaningful number of trajec-

tories to assess the importance of non-adiabatic effects in the presence of a realistic mobile substrate and quantitatively disentangle their contribution in the dissipative dynamics, both during dissociative surface reactions and in a vibrational damping context.

On a broader scope, the QM/Me methodology is generally suitable for application to any problem that breaks the translational symmetry of a metal in any number of periodic directions. Beyond the demonstrated relevance within a surface science context therefore, its applicability may be similarly extended to the bulk material for e.g. following interstitial diffusion, or addressing the chemistry around bulk defects and dislocations. We particularly envision QM/Me to play a prominent role in the investigation of radiation damage phenomena, where the *ab initio* treatment of nanoscale defects needs to be complemented with a realistic description of long-range elastic effects in large-scale atomistic simulations [136]. Apart from the intriguing prospect of dynamically capturing, for example, radiation-induced collision cascades from the QM/Me first-principles perspective, its application may also be highly beneficial in a "static" context for the development of future many-body interatomic potentials [23].

Acknowledgements

First and foremost, I feel the need to thank Prof. Dr. Karsten Reuter. His support was ever present, ceaseless and unwavering, whether for scientific advice or strategic guidance. This was strongly felt throughout the entire course of my Ph.D. and deserves acknowledgement above all. I would also like to deeply thank him, however, for the numerous "side-kick" opportunities I was given during this time. This includes an exceptional amount of conference traveling, my research visit to Stanford University (November 2014), the support for participating at the 65^{th} Lindau Nobel Laureate meeting (June 2015), and the chance to co-organize two of our fantastic group workshops (January 2015 & June 2016). Each and every one of these "adventures" added a special flavor to my Ph.D. experience and it is needless to say that I enjoyed them immensely.

I also owe my thanks, however, to a great number of other people. I would explicitly like to express my gratitude to all the people whom I have had the pleasure to collaborate with during my Ph.D. thesis, and to Dr. H. Fabio Busnengo for his SO, GLO code implementations. A special acknowledgement goes to Simon P. Rittmeyer for many fruitful discussions during our so-called "insiders' update meetings" (aka IUMs), his generous proof-readings of my manuscripts and presentations, and invaluable typesetting/artistic counsel. For many helpful comments and discussions, I am additionally grateful to Dr. Harald Oberhofer, Dr. Christoph Scheurer, Dr. Reinhard Maurer, Prof. John Tully, Prof. Matt Probert, and many more. For further technical support and their excellent system administrator skills, credit is definitely due to Dr. Christoph Scheurer (again), Christoph Schober, and Georg Michelitsch.

Many heartfelt thanks go in particular to past and present group members who have made this time so highly enjoyable. It certainly would not have been the same without them. And of course, my family and friends – old and new – they know how they are.

Finally, funding through the Deutsche Forschungsgemeinschaft is acknowledged within Project No. RE1509/19-1, as is generous access to CPU time through the Leibniz Rechenzentrum der Bayerischen Akademie der Wissenschaften (Project No. pr85wa).

Bibliography

[1] A. Groß, *"Theoretical Surface Science: A Microscopic Perspective"*, Advanced Texts in Physics (Springer-Verlag Berlin Heidelberg, 2003).

[2] M. Scheffler and C. Stampfl, *"Chapter 5 - Theory of Adsorption on Metal Substrates"*, in *Electronic Structure*, Vol. 2, edited by K. Horn and M. Scheffler, Handbook of Surface Science (North-Holland, 2000), p. 285.

[3] G.-J. Kroes, *"Frontiers in Surface Scattering Simulations"*, Science **321**, 794–797 (2008).

[4] A. J. Cohen, P. Mori-Sánchez, and W. Yang, *"Insights into Current Limitations of Density Functional Theory"*, Science **321**, 792–794 (2008).

[5] J. K. Nørskov, F. Abild-Pedersen, F. Studt, and T. Bligaard, *"Density functional theory in surface chemistry and catalysis"*, Proc. Natl. Acad. Sci. USA **108**, 937–943 (2011).

[6] A. Groß, *"Dynamics of Reactions at Surfaces"*, in *Modeling and Simulation of Heterogeneous Catalytic Reactions* (Wiley-VCH Verlag GmbH & Co. KGaA, 2011), p. 39.

[7] H. Brune, J. Wintterlin, R. J. Behm, and G. Ertl, *"Surface migration of "hot" adatoms in the course of dissociative chemisorption of oxygen on Al(111)"*, Phys. Rev. Lett. **68**, 624–626 (1992).

[8] J. Wintterlin, R. Schuster, and G. Ertl, *"Existence of a "Hot" Atom Mechanism for the Dissociation of O_2 on Pt(111)"*, Phys. Rev. Lett. **77**, 123–126 (1996).

[9] B. G. Briner, M. Doering, H.-P. Rust, and A. M. Bradshaw, *"Mobility and Trapping of Molecules During Oxygen Adsorption on Cu(110)"*, Phys. Rev. Lett. **78**, 1516–1519 (1997).

[10] M. Rose, A Borg, J. Dunphy, T Mitsui, D. Ogletree, and M Salmeron, *"Chemisorption of atomic oxygen on Pd(111) studied by STM"*, Surf. Sci. **561**, 69 –78 (2004).

[11] S. Schintke, S. Messerli, K. Morgenstern, J. Nieminen, and W.-D. Schneider, *"Far-ranged transient motion of hot oxygen atoms upon dissociation"*, J. Chem. Phys. **114**, 4206–4209 (2001).

[12] M.-F. Hsieh, D.-S. Lin, H. Gawronski, and K. Morgenstern, *"Hard repulsive barrier in hot adatom motion during dissociative adsorption of oxygen on Ag(100)"*, J. Chem. Phys. **131**, 174709 (2009).

[13] C. Sprodowski, M. Mehlhorn, and K. Morgenstern, *"Dissociation of oxygen on Ag(100) induced by inelastic electron tunneling"*, J. Phys.-Condens. Mat. **22**, 264005 (2010).

[14] I. Chorkendorff and J. W. Niemantsverdriet, *"Kinetics of Reactions on Surfaces"*, in *Concepts of Modern Catalysis and Kinetics* (Wiley-VCH Verlag GmbH & Co. KGaA, 2005), p. 267.

[15] K. Reuter, *"First-Principles Kinetic Monte Carlo Simulations for Heterogeneous Catalysis: Concepts, Status, and Frontiers"*, in *Modeling and Simulation of Heterogeneous Catalytic Reactions* (Wiley-VCH Verlag GmbH & Co. KGaA, 2011), p. 71.

[16] A. Carley, P. Davies, and M. Roberts, *"The Development of a New Concept: The Role of Oxygen Transients, Defect and Precursor States in Surface Reactions"*, English, Catal. Lett. **80**, 25–34 (2002).

[17]J. Barth, *"Transport of adsorbates at metal surfaces: from thermal migration to hot precursors"*, Surf. Sci. Rep. **40**, 75 –149 (2000).

[18]J. Harris and B. Kasemo, *"On precursor mechanisms for surface reactions"*, Surf. Sci. **105**, L281 –L287 (1981).

[19]W. F. Egelhoff and I. Jacob, *"Reflection High-Energy Electron Diffraction (RHEED) Oscillations at 77 K"*, Phys. Rev. Lett. **62**, 921–924 (1989).

[20]V. J. Bukas, J. Meyer, M. Alducin, and K. Reuter, *"Ready, Set and no Action: A Static Perspective on Potential Energy Surfaces commonly used in Gas-Surface Dynamics"*, Z. Phys. Chem. **227**, 1523 (2013).

[21]V. J. Bukas, S. Mitra, J. Meyer, and K. Reuter, *"Fingerprints of energy dissipation for exothermic surface chemical reactions: O_2 on Pd(100)"*, J. Chem. Phys. **143**, 034705 (2015).

[22]A. den Dunnen, S. Wiegman, L. Jacobse, and L. B. F. Juurlink, *"Reaction dynamics of initial O_2 sticking on Pd(100)"*, J. Chem. Phys. **142**, 214708 (2015).

[23]J. Meyer and K. Reuter, *"Modeling Heat Dissipation at the Nanoscale: An Embedding Approach for Chemical Reaction Dynamics on Metal Surfaces"*, Angew. Chem. Int. Edit. **53**, 4721–4724 (2014).

[24]V. J. Bukas and K. Reuter, *"Hot Adatom Diffusion Following Oxygen Dissociation on Pd(100) and Pd(111): A First-Principles Study of the Equilibration Dynamics of Exothermic Surface Reactions"*, Phys. Rev. Lett. **117**, 146101 (2016).

[25]V. J. Bukas and K. Reuter, *"Phononic dissipation during "hot" adatom motion: A QM/Me study of O_2 dissociation at Pd surfaces"*, J. Chem. Phys., *submitted* (2016).

[26]M. D. Stiles, J. W. Wilkins, and M. Persson, *"Inelastic gas-surface scattering. I. Formalism"*, Phys. Rev. B **34**, 4490–4510 (1986).

[27]B. Jackson, *"Time-dependent mean-field approach to molecule-surface scattering at finite temperatures"*, Comput. Phys. Commun. **63**, 154 –170 (1991).

[28]B. Jackson, *"Quantum and semiclassical calculations of gas-surface energy transfer and sticking"*, Comput. Phys. Commun. **80**, 119 –144 (1994).

[29]B. Jackson, *"Reduced density matrix description of gas-solid interactions: Scattering, trapping, and desorption"*, J. Chem. Phys. **108**, 1131–1139 (1998).

[30]X. Yang and A. M. Wodtke, *"Surface reaction dynamics"*, Chem. Soc. Rev. **45**, 3573–3575 (2016).

[31]M. S. Daw and M. I. Baskes, *"Semiempirical, Quantum Mechanical Calculation of Hydrogen Embrittlement in Metals"*, Phys. Rev. Lett. **50**, 1285–1288 (1983).

[32]M. S. Daw and M. I. Baskes, *"Embedded-atom method: Derivation and application to impurities, surfaces, and other defects in metals"*, Phys. Rev. B **29**, 6443–6453 (1984).

[33]M. I. Baskes, *"Modified embedded-atom potentials for cubic materials and impurities"*, Phys. Rev. B **46**, 2727–2742 (1992).

[34]L. H. Thomas, *"The calculation of atomic fields"*, Proc. Cambridge Phil. Soc. **23**, 542–548 (1927).

[35]E. Fermi, *"Eine statistische Methode zur Bestimmung einiger Eigenschaften des Atoms und ihre Anwendung auf die Theorie des periodischen Systems der Elemente"*, Zeitschrift für Physik **48**, 73–79 (1928).

[36]P. Hohenberg and W. Kohn, *"Inhomogeneous Electron Gas"*, Phys. Rev. **136**, B864–B871 (1964).

[37]W. Ritz, *"Über eine neue Methode zur Lösung gewisser Variationsprobleme der mathematischen Physik"*, Journal für die reine und angewandte Mathematik (Crelle's Journal) **1909**, 1–61 (1909).

[38]W. Kohn and L. J. Sham, *"Self-Consistent Equations Including Exchange and Correlation Effects"*, Phys. Rev. **140**, A1133–A1138 (1965).

[39]F. Jensen, *"Introduction to Computational Chemistry"*, 2nd ed. (Wiley, 2006).

[40]A. D. Becke, *"Density-functional exchange-energy approximation with correct asymptotic behavior"*, Phys. Rev. A **38**, 3098–3100 (1988).

[41]J. P. Perdew, J. A. Chevary, S. H. Vosko, K. A. Jackson, M. R. Pederson, D. J. Singh, and C. Fiolhais, *"Atoms, molecules, solids, and surfaces: Applications of the generalized gradient approximation for exchange and correlation"*, Phys. Rev. B **46**, 6671–6687 (1992).

[42]J. P. Perdew, K. Burke, and M. Ernzerhof, *"Generalized Gradient Approximation Made Simple"*, Phys. Rev. Lett. **77**, 3865–3868 (1996).

[43]J. P. Perdew, K. Burke, and M. Ernzerhof, *"Generalized Gradient Approximation Made Simple [Phys. Rev. Lett. 77, 3865 (1996)]"*, Phys. Rev. Lett. **78**, 1396–1396 (1997).

[44]B. Hammer, L. Hansen, and J. K. Nørskov, *"Improved adsorption energetics within density-functional theory using revised Perdew-Burke-Ernzerhof functionals"*, Phys. Rev. B **59**, 7413–7421 (1999).

[45]S. J. Clark, M. D. Segall, C. J. Pickard, P. J. Hasnip, M. I. J. Probert, and M. C. Payne, *"First principles methods using CASTEP"*, Z. Kristallogr. **220**, 567–570 (2005).

[46]V. Blum, R. Gehrke, F. Hanke, P. Havu, V. Havu, X. Ren, K. Reuter, and M. Scheffler, *"Ab initio molecular simulations with numeric atom-centered orbitals"*, Comput. Phys. Commun. **180**, 2175 –2196 (2009).

[47]V. J. Bukas and K. Reuter, *"A comparative study of oxygen adsorption at Pd surfaces from Density Functional Theory"*, Surf. Sci., *submitted* (2016).

[48]Y. Zhao and D. G. Truhlar, *"A new local density functional for main-group thermochemistry, transition metal bonding, thermochemical kinetics, and noncovalent interactions"*, J. Chem. Phys. **125**, 194101 (2006).

[49]M. J. Stott and E. Zaremba, *"Quasiatoms: An approach to atoms in nonuniform electronic systems"*, Phys. Rev. B **22**, 1564–1583 (1980).

[50]M. S. Daw and R. Hatcher, *"Application of the embedded atom method to phonons in transition metals"*, Solid State Commun. **56**, 697 –699 (1985).

[51]J. S. Nelson, E. C. Sowa, and M. S. Daw, *"Calculation of Phonons on the Cu(100) Surface by the Embedded-Atom Method"*, Phys. Rev. Lett. **61**, 1977–1980 (1988).

[52]J. S. Nelson, M. S. Daw, and E. C. Sowa, *"Cu(111) and Ag(111) surface-phonon spectrum: The importance of avoided crossings"*, Phys. Rev. B **40**, 1465–1480 (1989).

[53]J. Nelson, M. Daw, and E. C. Sowa, *"Embedded atom calculations of the Cu (001), (111), and (110) surface phonon spectra"*, Superlattices Microstruct. **7**, 259 –267 (1990).

[54]I. Sklyadneva, G. Rusina, and E. Chulkov, *"Vibrational states on vicinal surfaces of Al, Ag, Cu and Pd"*, Surf. Sci. **416**, 17 –36 (1998).

[55]M. Born and R. Oppenheimer, *"Zur Quantentheorie der Molekeln"*, Ann. Phys. **389**, 457–484 (1927).

[56]J. E. Lennard-Jones, *"Processes of adsorption and diffusion on solid surfaces"*, Trans. Faraday Soc. **28**, 333–359 (1932).

[57]J. H. McCreery and G. Wolken, *"A model potential for chemisorption: H2+W(001)"*, J. Chem. Phys. **63**, 2340–2349 (1975).

[58]J. H. McCreery and G. Wolken, *"Erratum: A model potential for chemisorption: H2+W(001)"*, J. Chem. Phys. **65**, 2922–2922 (1976).

[59]J. H. McCreery and G. Wolken, *"Atomic recombination dynamics on a solid surface: H2+W(001)"*, J. Chem. Phys. **64**, 2845–2853 (1976).

[60]J. H. McCreery and G. Wolken, *"Dynamics of adsorption on covered surfaces"*, J. Chem. Phys. **66**, 2316–2321 (1977).

[61]J. H. McCreery and G. Wolken, *"Atomic recombination dynamics on solid surfaces: Effect of various potentials"*, J. Chem. Phys. **67**, 2551–2559 (1977).

[62]L. Martin-Gondre, C. Crespos, P. Larregaray, J. Rayez, B. van Ootegem, and D. Conte, *"Is the {LEPS} potential accurate enough to investigate the dissociation of diatomic molecules on surfaces?"*, Chem. Phys. Lett. **471**, 136 –142 (2009).

[63]L. Martin-Gondre, C. Crespos, P. Larrgaray, J. Rayez, D. Conte, and B. van Ootegem, *"Detailed description of the flexible periodic London?Eyring?Polanyi?Sato potential energy function"*, Chem. Phys. **367**, 136 –147 (2010).

[64]G. R. Darling and S Holloway, *"The dissociation of diatomic molecules at surfaces"*, Rep. Prog. Phys. **58**, 1595 (1995).

[65]A. Groß, S. Wilke, and M. Scheffler, *"Six-Dimensional Quantum Dynamics of Adsorption and Desorption of* H_2 *at Pd(100): Steering and Steric Effects"*, Phys. Rev. Lett. **75**, 2718–2721 (1995).

[66]C. T. Rettner and D. J. Auerbach, *"Comment on "Six-Dimensional Quantum Dynamics of Adsorption and Desorption of* H_2 *at Pd(100): Steering and Steric Effects""*, Phys. Rev. Lett. **77**, 404–404 (1996).

[67]A. Groß and M. Scheffler, *"Gross and Scheffler Reply:"* Phys. Rev. Lett. **77**, 405–405 (1996).

[68]A. Groß and M. Scheffler, *"Proceedings of the 18th International Seminar on Surface Physics Steering and ro-vibrational effects on dissociative adsorption and associative desorption of H2Pd(100)"*, Prog. Surf. Sci. **53**, 187 –196 (1996).

[69]G. Wiesenekker, G. J. Kroes, and E. J. Baerends, *"An analytical six?dimensional potential energy surface for dissociation of molecular hydrogen on Cu(100)"*, J. Chem. Phys. **104**, 7344–7358 (1996).

[70]A. Groß and M. Scheffler, *"Ab initio quantum and molecular dynamics of the dissociative adsorption of hydrogen on Pd(100)"*, Phys. Rev. B **57**, 2493–2506 (1998).

[71]A. Groß, *"Reactions at surfaces studied by ab initio dynamics calculations"*, Surf. Sci. Rep. **32**, 291 –340 (1998).

[72]D. A. McCormack, G.-J. Kroes, R. A. Olsen, J. A. Groeneveld, J. N. P. van Stralen, E. J. Baerends, and R. C. Mowrey, *"Quantum dynamics of the dissociation of* H_2 *on Cu(100): Dependence of the site-reactivity on initial rovibrational state"*, Faraday Discuss. **117**, 109–132 (2000).

[73]G.-J. Kroes, A. Groß, E.-J. Baerends, M. Scheffler, and D. A. McCormack, *"Quantum Theory of Dissociative Chemisorption on Metal Surfaces"*, Acc. Chem. Res. **35**, 193–200 (2002).

[74]A. Groß, *"Ab Initio Molecular Dynamics Simulations of the Adsorption of* H_2 *on Palladium Surfaces"*, Chem. Phys. Chem. **11**, 1374–1381 (2010).

[75]G. Ertl, *"Dynamics of reactions at surfaces"*, in *Impact of Surface Science on Catalysis*, Vol. 45, Advances in Catalysis (Academic Press, 2000), p. 1.

[76]A. M. Wodtke, J. C. Tully, and D. J. Auerbach, *"Electronically non-adiabatic interactions of molecules at metal surfaces: Can we trust the Born?Oppenheimer approximation for surface chemistry?"*, Int. Rev. Phys. Chem **23**, 513–539 (2004).

[77]J. Meyer and K. Reuter, *"Electron?hole pairs during the adsorption dynamics of O_2 on Pd(100): exciting or not?"*, New J. Phys. **13**, 085010 (2011).

[78]O. Bünermann, H. Jiang, Y. Dorenkamp, A. Kandratsenka, S. M. Janke, D. J. Auerbach, and A. M. Wodtke, *"Electron-hole pair excitation determines the mechanism of hydrogen atom adsorption"*, Science **350**, 1346–1349 (2015).

[79]M. Hand and J. Harris, *"Recoil effects in surface dissociation"*, J. Chem. Phys. **92**, 7610–7617 (1990).

[80]S. A. Adelman and J. D. Doll, *"Generalized Langevin equation approach for atom/solid?surface scattering: General formulation for classical scattering off harmonic solids"*, J. Chem. Phys. **64**, 2375–2388 (1976).

[81]J. C. Tully, *"Dynamics of gas-surface interactions: Reaction of atomic oxygen with adsorbed carbon on platinum"*, J. Chem. Phys. **73**, 6333–6342 (1980).

[82]J. C. Polanyi and R. J. Wolf, *"Dynamics of simple gas?surface interaction. II. Rotationally inelastic collisions at rigid and moving surfaces"*, J. Chem. Phys. **82**, 1555–1566 (1985).

[83]M. Dohle and P. Saalfrank, *"Surface oscillator models for dissociative sticking of molecular hydrogen at non-rigid surfaces"*, Surf. Sci. **373**, 95–108 (1997).

[84]H. F. Busnengo, W. Dong, P. Sautet, and A. Salin, *"Surface Temperature Dependence of Rotational Excitation of H_2 Scattered from Pd(111)"*, Phys. Rev. Lett. **87**, 127601 (2001).

[85]H. F. Busnengo, W. Dong, and A. Salin, *"Trapping, Molecular Adsorption, and Precursors for Nonactivated Chemisorption"*, Phys. Rev. Lett. **93**, 236103 (2004).

[86]H. F. Busnengo, M. A. Di Césare, W. Dong, and A. Salin, *"Surface temperature effects in dynamic trapping mediated adsorption of light molecules on metal surfaces: H_2 on Pd(111) and Pd(110)"*, Phys. Rev. B **72**, 125411 (2005).

[87]A. Groß, *"Ab Initio Molecular Dynamics Study of Hot Atom Dynamics after Dissociative Adsorption of H_2 on Pd(100)"*, Phys. Rev. Lett. **103**, 246101 (2009).

[88]H. F. Busnengo, A. Salin, and W. Dong, *"Representation of the 6D potential energy surface for a diatomic molecule near a solid surface"*, J. Chem. Phys. **112**, 7641–7651 (2000).

[89]H. Busnengo, W. Dong, and A. Salin, *"Six-dimensional classical dynamics of H_2 dissociative adsorption on Pd(111)"*, Chem. Phys. Lett. **320**, 328 –334 (2000).

[90]R. A. Olsen, H. F. Busnengo, A. Salin, M. F. Somers, G. J. Kroes, and E. J. Baerends, *"Constructing accurate potential energy surfaces for a diatomic molecule interacting with a solid surface: H_2+Pt(111) and H_2+Cu(100)"*, J. Chem. Phys. **116**, 3841–3855 (2002).

[91]C. Crespos, M. Collins, E. Pijper, and G. Kroes, *"Multi-dimensional potential energy surface determination by modified Shepard interpolation for a molecule?surface reaction: H_2 + Pt(111)"*, Chem. Phys. Lett. **376**, 566 –575 (2003).

[92]P. N. Abufager, C. Crespos, and H. F. Busnengo, *"Modified Shepard interpolation method applied to trapping mediated adsorption dynamics"*, Phys. Chem. Chem. Phys. **9**, 2258–2265 (2007).

[93]A. Groß, A. Eichler, J. Hafner, M. J. Mehl, and D. A. Papaconstantopoulos, *"Ab initio based tight-binding molecular dynamics simulation of the sticking and scattering of O_2/Pt(111)"*, J. Chem. Phys. **124**, 174713 (2006).

[94]S. Lorenz, A. Groß, and M. Scheffler, *"Representing high-dimensional potential-energy surfaces for reactions at surfaces by neural networks"*, Chem. Phys. Lett. **395**, 210–215 (2004).

[95]S. Lorenz, M. Scheffler, and A. Groß, *"Descriptions of surface chemical reactions using a neural network representation of the potential-energy surface"*, Phys. Rev. B **73**, 115431 (2006).

[96]J. Behler, S. Lorenz, and K. Reuter, *"Representing molecule-surface interactions with symmetry-adapted neural networks"*, J. Chem. Phys. **127**, 014705 (2007).

[97]I. Goikoetxea, J. Beltrán, J. Meyer, J. I. Juaristi, M. Alducin, and K. Reuter, *"Non-adiabatic effects during the dissociative adsorption of O_2 at Ag(111)? A first-principles divide and conquer study"*, New J. Phys. **14**, 013050 (2012).

[98]G. Cybenko, *"Approximation by superpositions of a sigmoidal function"*, Math. Control Signals Syst. **2**, 303–314 (1989).

[99]K. Hornik, M. Stinchcombe, and H. White, *"Multilayer feedforward networks are universal approximators"*, Neural Networks **2**, 359–366 (1989).

[100]C. M. Handley and P. L. A. Popelier, *"Potential Energy Surfaces Fitted by Artificial Neural Networks"*, J. Phys. Chem. A **114**, 3371–3383 (2010).

[101]J. Behler, *"Neural network potential-energy surfaces in chemistry: a tool for large-scale simulations"*, Phys. Chem. Chem. Phys. **13**, 17930–17955 (2011).

[102]J. Behler, *"Constructing high-dimensional neural network potentials: A tutorial review"*, Int. J. Quantum Chem. **115**, 1032–1050 (2015).

[103]M. Shugard, J. C. Tully, and A. Nitzan, *"Dynamics of gas?solid interactions: Calculations of energy transfer and sticking"*, J. Chem. Phys. **66**, 2534–2544 (1977).

[104]J. C. Tully, G. H. Gilmer, and M. Shugard, *"Molecular dynamics of surface diffusion. I. The motion of adatoms and clusters"*, J. Chem. Phys. **71**, 1630–1642 (1979).

[105]J. C. Tully, *"Dynamics of gas-surface interactions: 3D generalized Langevin model applied to fcc and bcc surfaces"*, J. Chem. Phys. **73**, 1975–1985 (1980).

[106]M. Dohle, P. Saalfrank, and T. Uzer, *"The dissociation of diatomic molecules on vibrating surfaces: A semiclassical generalized Langevin approach"*, J. Chem. Phys. **108**, 4226–4236 (1998).

[107]D. J. Auerbach, *"Inelastic Scattering of Atoms and Molecules from Solid Surfaces"*, Phys. Scripta **1983**, 122 (1983).

[108]A. S. Sanz and S. Miret-Artés, *"Selective adsorption resonances: Quantum and stochastic approaches"*, Phys. Rep. **451**, 37 –154 (2007).

[109]J. Meyer, *"Ab initio modeling of energy dissipation during chemical reactions at transition metal surfaces"*, PhD thesis (Freie Universität Berlin, Germany, 2012).

[110]H. Lin and D. Truhlar, *"QM/MM: what have we learned, where are we, and where do we go from here?"*, English, Theor. Chem. Acc. **117**, 185–199 (2007).

[111]C. Bo and F. Maseras, *"QM/MM methods in inorganic chemistry"*, Dalton Trans., 2911–2919 (2008).

[112]N. Bernstein, J. R. Kermode, and G. Csányi, *"Hybrid atomistic simulation methods for materials systems"*, Rep. Prog. Phys. **72**, 026501 (2009).

[113]W. Kohn, *"Density Functional and Density Matrix Method Scaling Linearly with the Number of Atoms"*, Phys. Rev. Lett. **76**, 3168–3171 (1996).

[114]E. Prodan and W. Kohn, *"Nearsightedness of electronic matter"*, Proc. Natl. Acad. Sci. USA **102**, 11635–11638 (2005).

[115]G. Horton and A. Maradudin, *"Dynamical properties of solids"*, Dynamical Properties of Solids v. 1 (North-Holland, 1974).

[116]M. Svensson, S. Humbel, R. D. J. Froese, T. Matsubara, S. Sieber, and K. Morokuma, *"ONIOM: A Multilayered Integrated MO + MM Method for Geometry Optimizations and Single Point Energy Predictions. A Test for Diels-Alder Reactions and Pt(P(t-Bu)$_3$)$_2$ + H_2 Oxidative Addition"*, J. Phys. Chem. **100**, 19357–19363 (1996).

[117]A. A. Maradudin and A. E. Fein, *"Scattering of Neutrons by an Anharmonic Crystal"*, Phys. Rev. **128**, 2589–2608 (1962).

[118]N. Ashcroft and N. Mermin, *"Solid State Physics"* (Cengage Learning, 2011).

[119]S. Baroni, P. Giannozzi, and A. Testa, *"Green's-function approach to linear response in solids"*, Phys. Rev. Lett. **58**, 1861–1864 (1987).

[120]X. Gonze, *"Adiabatic density-functional perturbation theory"*, Phys. Rev. A **52**, 1096–1114 (1995).

[121]S. Baroni, S. de Gironcoli, A. Dal Corso, and P. Giannozzi, *"Phonons and related crystal properties from density-functional perturbation theory"*, Rev. Mod. Phys. **73**, 515–562 (2001).

[122]D. Vanderbilt, S. G. Louie, and M. L. Cohen, *"Calculation of anharmonic phonon couplings in C, Si, and Ge"*, Phys. Rev. B **33**, 8740–8747 (1986).

[123]A. J. H. McGaughey and M. Kaviany, *"Quantitative validation of the Boltzmann transport equation phonon thermal conductivity model under the single-mode relaxation time approximation"*, Phys. Rev. B **69**, 094303 (2004).

[124]X. Tang, C. W. Li, and B. Fultz, *"Anharmonicity-induced phonon broadening in aluminum at high temperatures"*, Phys. Rev. B **82**, 184301 (2010).

[125]M. Allen and D. Tildesley, *"Computer Simulation of Liquids"*, Oxford Science Publ (Clarendon Press, 1989).

[126]M. M. Siddick, G. J. Ackland, and C. A. Morrison, *"Constrained dynamics and extraction of normal modes from ab initio molecular dynamics: Application to ammonia"*, J. Chem. Phys. **125**, 064707, – (2006).

[127]N. de Koker, *"Thermal Conductivity of MgO Periclase from Equilibrium First Principles Molecular Dynamics"*, Phys. Rev. Lett. **103**, 125902 (2009).

[128]N. de Koker, *"Thermal conductivity of MgO periclase at high pressure: Implications for the D? region"*, Earth Planet. Sc. Lett. **292**, 392 –398 (2010).

[129]M. Alducin, H. F. Busnengo, and R. D. Muiño, *"Dissociative dynamics of spin-triplet and spin-singlet O_2 on Ag(100)"*, J. Chem. Phys. **129**, 224702 (2008).

[130]S. R. Bahn and K. W. Jacobsen, *"An object-oriented scripting interface to a legacy electronic structure code"*, English, Comput. Sci. Eng. **4**, 56–66 (2002).

[131]M. Todorova, K. Reuter, and M. Scheffler, *"Oxygen Overlayers on Pd(111) Studied by Density Functional Theory"*, J. Phys. Chem. B **108**, 14477–14483 (2004).

[132]Y. Zhang, V. Blum, and K. Reuter, *"Accuracy of first-principles lateral interactions: Oxygen at Pd(100)"*, Phys. Rev. B **75**, 235406 (2007).

[133]Y. Li and G. Wahnström, *"Nonadiabatic effects in hydrogen diffusion in metals"*, Phys. Rev. Lett. **68**, 3444–3447 (1992).

[134]J. I. Juaristi, M. Alducin, R. D. Muiño, H. F. Busnengo, and A. Salin, *"Role of Electron-Hole Pair Excitations in the Dissociative Adsorption of Diatomic Molecules on Metal Surfaces"*, Phys. Rev. Lett. **100**, 116102 (2008).

[135]S. P. Rittmeyer, J. Meyer, J. I. Juaristi, and K. Reuter, *"Electronic Friction-Based Vibrational Lifetimes of Molecular Adsorbates: Beyond the Independent-Atom Approximation"*, Phys. Rev. Lett. **115**, 046102 (2015).

[136]S. Dudarev, *"Density Functional Theory Models for Radiation Damage"*, Annu. Rev. Mater. Res. **43**, 35–61 (2013).

Part III.

Appendix: Publications

Paper #1

Ready, Set and no Action: A Static Perspective on Potential Energy Surfaces commonly used in Gas-Surface Dynamics.
V. J. Bukas, J. Meyer, M. Alducin and K. Reuter; Z. Phys. Chem. **227**, 1523 (2013).

Z. Phys. Chem. / **DOI** 10.1524/zpch.2013.0410

Ready, Set and no Action: A Static Perspective on Potential Energy Surfaces commonly used in Gas-Surface Dynamics

By Vanessa Jane Bukas[1], Jörg Meyer[1,*], Maite Alducin[2], and Karsten Reuter[1]

[1] Technische Universität München, Lichtenbergstraße 4, D-85747 Garching, Germany
[2] Centro de Física de Materiales CFM, Centro Mixto CSIC-UPV/EHU, Paseo Manuel de Lardizabal 5, 20018 San Sebastián, Spain

(Received March 8, 2013; accepted in revised form June 27, 2013)
(Published online August 5, 2013)

PES / Gas-Surface Dynamics / Dissociative Sticking Probability / Corrugation-Reducing Procedure / Neural Networks / Global Minima Search

In honoring the seminal contribution of Henry Eyring and Michael Polanyi who first introduced the concept of potential energy surfaces (PESs) to describe chemical reactions in gas-phase [Z. Phys. Chem. 12, 279–311, (1931)], this work comes to review and assess state-of-the-art approaches towards first-principle based modeling in the field of gas-surface dynamics. Within the Born-Oppenheimer and frozen surface approximations, the O_2-Ag(100) interaction energetics are used as a showcase system to accentuate the complex landscape exhibited by the PESs employed to describe the impingement of diatomics on metal substrates and draw attention to the far-from-trivial task of continuously representing them within all six molecular degrees of freedom. To this end, the same set of *ab initio* reference data obtained within Density Functional Theory (DFT) are continuously represented by two different state-of-the-art high-dimensional approaches, namely the Corrugation-Reducing Procedure and Neural Networks. Exploiting the numerically undemanding nature of the resulting representations, a detailed static evaluation is performed on both PESs based on an extensive global minima search. The latter proved particularly illuminating in revealing representation deficiencies which affect the dynamical picture yet go otherwise unnoticed within the so-called "divide-and-conquer" approach.

1. Introduction

Reflecting the ingenuity of the idea, some 80 years after the seminal contribution of Eyring and Polanyi [1] it is difficult to envision chemical reactions without following their footsteps to consider a practical consequence of the Born-Oppenheimer approximation (BOA) [2]: potential energy surfaces (PESs). Knowledge of the potential energy as a function of the atomic positions provides the basis for a most thorough molecular-level understanding of the reaction, in which prominent topological features of the PES

* Corresponding author. E-mail: joerg.meyer@ch.tum.de

like minima and saddle points play a central role. Apart from such static information, a continuous representation of the PES may also be used for explicit dynamical simulations of individual reaction events. If allowed by the numerical efficiency of the latter, appropriate averages over a sufficiently large number of trajectories can routinely be obtained using computational resources commonly available nowadays, thus giving access to the kinetics of the reaction and thereby fulfilling one of the visions of the pioneers Eyring and Polanyi [1].

Although all the more accurate BOA-based numerical solutions of the Schrödinger equation have become available during the last eight decades [3], the dimensionality of the problem still remains a major limitation to employing the PES concept in practice. As demonstrated by Eyring and Polanyi [1] for simple reactions involving triples and quadruples of atoms in gas phase, a comprehensive understanding of the PES topology can even visually be obtained along two reaction coordinates. For higher dimensions this becomes an increasingly challenging dilemma which research on gas-surface interactions has been battling with for a long time [4,5]: In contrast to gas-phase reactions, the presence of the solid surface destroys the overall rotational and translational symmetry of the overlaying adsorbate species. Consequently, a description based on intramolecular (in particular) distances alone is no longer possible [6], thus inflicting an intrinsically higher dimensionality already for diatomics. In the meantime, the interaction of localized molecular bonds with the extended electronic manifold in particular of catalytically interesting metal surfaces gives rise to complex corrugated PES topologies that cannot readily be described by a reduced number of reaction coordinates. It is therefore not surprising that extensive first-principles based work focusing on prototypical H_2 adsorbates has shown that at least all six *molecular* degrees of freedom need to be explicitly considered in order to arrive at a quantitative understanding of central kinetic parameters such as (dissociative) sticking probabilities on rigid surfaces [7–9].

The exponential growth of computational power has allowed for evaluating thousands of trajectories through molecular dynamics (MD) simulations [10,11] already some 30 years ago – when basing the representation of the high-dimensional PES on classical interatomic potentials (CIPs) with "simple" analytical forms (like *e.g.* the Morse potentials used by Eyring and Polanyi [1]). Nowadays, kinetic quantities requiring statistical averaging over even orders of magnitude more trajectories can, in fact, readily be obtained for (such) numerically convenient PESs, also *e.g.* as a function of initial kinetic energy and varying incidence angles [5]. It soon became clear, however, that even the semi-empirical CIPs – with the London-Eyring-Polanyi-Sato (LEPS) potential as the most prominent example – are severely challenged in capturing the complex bond breaking and making involved in a dissociative adsorption or recombination event [11] (although promising steps towards more accurate parametrizations from first principles have recently been reported [5,12,13]).

On the other hand, *ab initio* electronic structure calculations, even if based on computationally efficient semi-local density-functional theory (DFT), have been far too expensive to allow for an on-the-fly evaluation of the PES. As heralded by first determinations of sticking coefficients through *ab initio* molecular dynamics (AIMD) [14], this situation might just be changing, at least in cases where less extensive statistical sampling can be accepted. Nevertheless, the huge number of trajectories required to properly determine small reaction probabilities of *e.g.* $\lesssim 1\%$ [15] practically excludes

direct application of AIMD for many systems for some time still to come. This is particularly true when taking into account nuclear quantum effects, which can be significant for the aforementioned prototypical H_2 adsorbates [8,16].

Given this situation, the state-of-the-art is still defined to its larger extent by a divide-and-conquer type approach. The 6D PES of a diatomic interacting with a frozen surface is first mapped discretely by first-principles calculations and subsequently "continued in between" (ensuring differentiability up to at least first order). The actual dynamical simulations are finally conducted on this (numerically undemanding) continuous representation by solving the appropriate classical or quantum mechanical equations of motion. While conceptually appealing, the practical bottleneck of this approach is the difficulty of procuring *and* assessing a reliable differentiable interpolation in high (in fact even just six) dimensions that usually are very closely intertwined.

Particularly the latter point shall be the major topic of the present contribution. With a number of high-dimensional interpolation techniques suggested and employed in the context of gas-surface dynamics [17–28], we will focus here on the prevalent corrugation-reducing procedure (CRP) [17–19] and neural networks (NNs) [29,30] with proper symmetry adaption [24–26,28]. Providing a nice showcase for the PES complexity often met in gas-surface dynamics, we use these two techniques to continuously represent a given DFT data set for O_2 at Ag(100) from Alducin *et al.* [31]. After comparing and highlighting the methodological differences of both approaches in Sect. 2, we show in Sect. 3 that the two representations yield notably different reaction probabilities for the oxygen molecule, despite flawlessly passing the typical reliability checks performed to assess the interpolation quality. We therefore perform a thorough investigation into the global energetics of the two representations both in terms of 2D visualizations and of identifying the energetically low lying minima through extensive configurational sampling. This is found a particularly illuminating approach not only in regionally evaluating the accuracy of the PES representations, but also in providing an insightful picture into the intricate PES topologies. For the O_2/Ag(100) system it rationalizes the discrepancies found for important dynamical observables within the two interpolation schemes, thereby highlighting the issue of the interpolation reliability and suggesting to generally perform *a priori* static PES examinations within the divide-and-conquer approach.

2. Methodology

2.1 Coordinate systems

As indicated in the introduction and depicted in Fig. 1, the 'full-dimensional' representation of the interaction between a diatomic molecule and a rigid substrate surface corresponds to a six-dimensional problem. Straightforwardly, the molecular degrees of freedom can be expressed in terms of the Cartesian coordinates of the two adsorbate constituent atoms A and B

$$\boldsymbol{R}^{\text{cart}} = (\underbrace{X_\text{A}, Y_\text{A}, Z_\text{A}}_{\boldsymbol{R}_\text{A}}, \underbrace{X_\text{B}, Y_\text{B}, Z_\text{B}}_{\boldsymbol{R}_\text{B}}) , \tag{1}$$

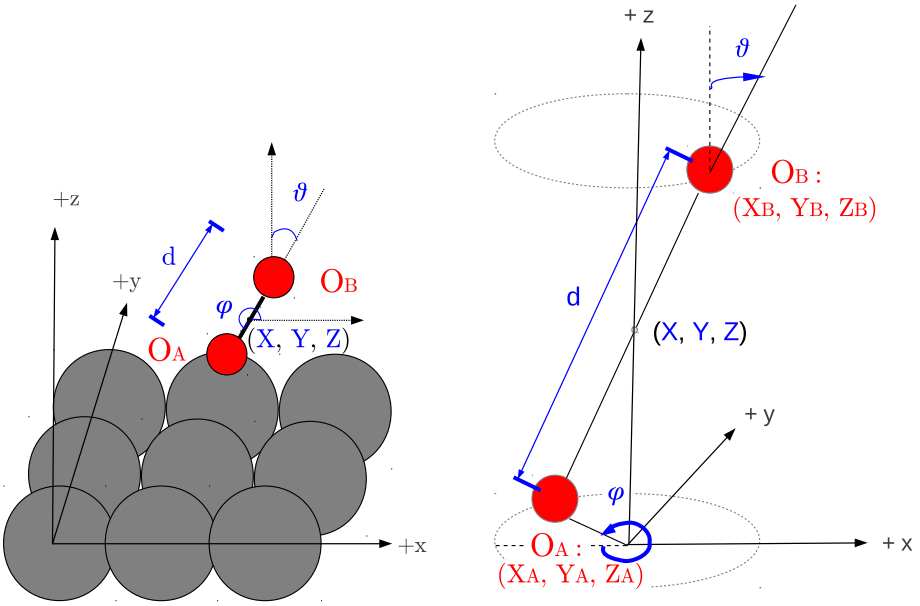

Fig. 1. Illustration of the 6D coordinate systems used to represent diatomic molecules above a frozen surface. Position and orientation of the molecule can be equivalently described by Cartesian $\boldsymbol{R}^{\text{cart}} = (X_\text{A}, Y_\text{A}, Z_\text{A}, X_\text{B}, Y_\text{B}, Z_\text{B})$ or spherical $\boldsymbol{R}^{\text{sph}} = (X, Y, Z, d, \vartheta, \varphi)$ coordinates. The left panel depicts the spherical representation of the adsorbate-surface system with the axes origin located in the surface plane on a top site. The right panel provides a more detailed illustration of the molecular orientation (ϑ, φ) within the spherical representation and the equivalent Cartesian representation.

where for all what is to follow, the origin of the coordinate system is located in the top layer of the Ag(100) surface at the position of a silver atom (top site, *cf.* Figs. 1 and 2). Another representation that more directly conveys equivalent configurations due to surface-induced symmetry as summarized by Fig. 2 is based on spherical coordinates

$$\boldsymbol{R}^{\text{sph}} = (\underbrace{X, Y, Z}_{\boldsymbol{R}}, d, \vartheta, \varphi)\,, \tag{2}$$

with the molecular center of mass $\boldsymbol{R}$, d the molecule's internuclear distance, and (ϑ, φ) the polar and azimuth angle, respectively, as defined in Fig. 1.

While $\boldsymbol{R}^{\text{cart}}$ can be obtained from $\boldsymbol{R}^{\text{sph}}$ without any ambiguities

$$\boldsymbol{R}_{\text{A,B}} = \boldsymbol{R} \mp \frac{m_{\text{B,A}}}{M}\, d\, (\sin\vartheta\cos\varphi, \sin\vartheta\sin\varphi, \cos\vartheta)\,, \tag{3}$$

we emphasize that special care must be taken with properly defining the inverse transformation $\boldsymbol{R}^{\text{sph}}(\boldsymbol{R}^{\text{cart}})$:

$$\boldsymbol{R} = \frac{m_\text{A}}{M}\boldsymbol{R}_\text{A} + \frac{m_\text{B}}{M}\boldsymbol{R}_\text{B} \tag{4a}$$

$$d = \sqrt{\underbrace{(X_\text{B} - X_\text{A})^2 + (Y_\text{B} - Y_\text{A})^2}_{d_\parallel^2} + \underbrace{(Z_\text{B} - Z_\text{A})^2}_{d_\perp^2}} \tag{4b}$$

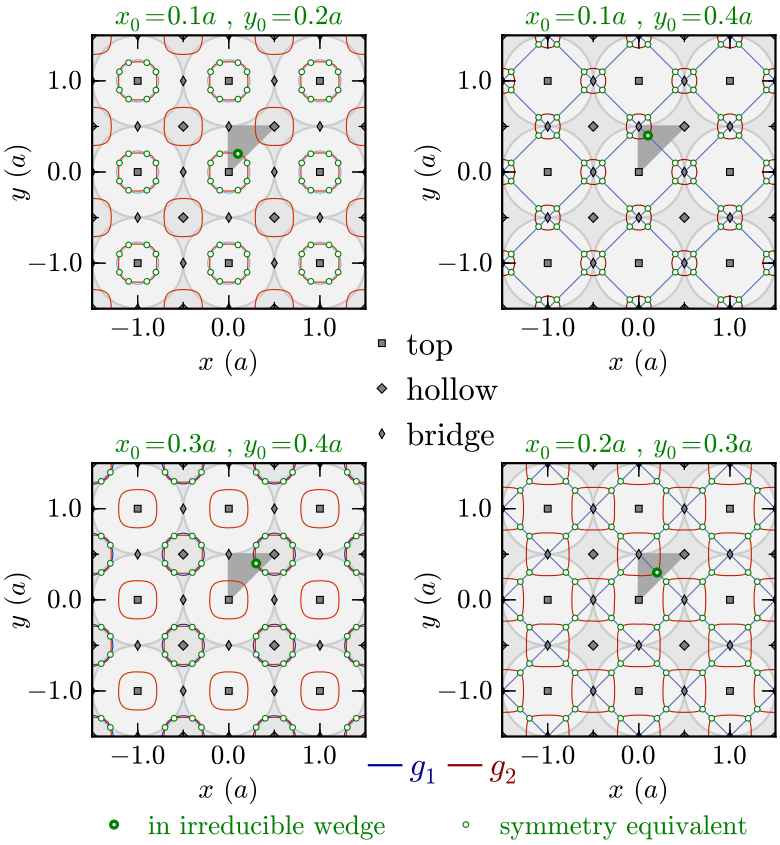

Fig. 2. Examples for symmetry equivalent lateral coordinates on the Ag(100) surface given in units of the surface lattice constant a. For different points (x_0, y_0) (thick green circle) in the indicated triangular irreducible wedge (dark gray area), in each panel the equivalents are the intersection points (thin green circles) of contour lines of the functions g_1 (blue) and g_2 (red) as defined by Eqs. (6). Contour values of g_1 and g_2 are given by $g_1(x_0, y_0)$ and $g_2(x_0, y_0)$, respectively. In addition to the translation symmetry, note the different local point group symmetry around the high symmetry sites of the surface: top and hollow sites feature four (left panels), whereas the bridge sites feature only two mirror planes perpendicular to the surface (right panels) – thus resulting in the aforementioned triangular irreducible wedge. Surface atoms are indicated by the large light gray circles, with the one in the center of the plot defining the top site at which the origin is located.

$$\vartheta = \arccos\left(\frac{Z_\mathrm{B} - Z_\mathrm{A}}{d}\right) \cdot \frac{180^\circ}{\pi} \qquad \in [0^\circ, 180^\circ] \tag{4c}$$

$$\varphi = \mathrm{H}(Y_\mathrm{A} - Y_\mathrm{B}) \cdot 360^\circ + \mathrm{sign}(Y_\mathrm{B} - Y_\mathrm{A}) \arccos\left(\frac{X_\mathrm{B} - X_\mathrm{A}}{d_\parallel}\right) \cdot \frac{180^\circ}{\pi} \qquad \in [0^\circ, 360^\circ)\,, \tag{4d}$$

where $m_{\mathrm{A,B}}$ is the mass of atoms A, B and $M = m_\mathrm{A} + m_\mathrm{B}$ the mass of the entire molecule. The distances $d_\parallel$ and $d_\perp$ are the components of the internuclear distance d in the xy plane and along the z axis, respectively. Particular care must be taken in defining the validity ranges and reference directions of the angular variables. The convention that has been chosen here (and depicted in Fig. 1) has the polar angle ϑ restricted to $[0^\circ, 180^\circ]$ as configurations with $\vartheta \in (180^\circ, 360^\circ)$ may be described by equivalent counterparts in the aforementioned interval by rotating an additional 180° in φ. Accordingly,

the Heaviside (or step) function H and the sign function are used in Eq. (4d) in order to ensure that configurations in all four quadrants are mapped to the correct value of $\varphi \in [0°, 360°]$. Note that permutation symmetry of homo-nuclear diatomics is deliberately not included here, thus distinguishing $\boldsymbol{R}^{\text{sph}}(\boldsymbol{R}_\text{A}, \boldsymbol{R}_\text{B}) \neq \boldsymbol{R}^{\text{sph}}(\boldsymbol{R}_\text{B}, \boldsymbol{R}_\text{A})$. The proper one-to-one mapping established here by Eqs. (3) and (4) is crucial for the global minima search described in Sect. 2.5 below, as this involves frequent back-and-forth transformations in order to identify symmetry-equivalent configurations.

In this context and even more so for the neural network interpolation described in Sect. 2.3, symmetry adapted coordinates defined (for homo-nuclear diatomics) in a similar way to Ref. [28] are of particular importance. These map configurations that are equivalent by the permutation- and surface-induced symmetries (*cf.* Fig. 2) to the same $\boldsymbol{Q}(\boldsymbol{R}^{\text{cart}}, \boldsymbol{R}^{\text{sph}}) \in \mathbb{R}^9$,

$$Q_{1,3} = \frac{1}{2} \sum_{I \in \{A,B\}} \exp\left(-\frac{1}{2} Z_I\right) \cdot g_{1,2}(X_i, Y_i) \tag{5a}$$

$$Q_{2,4} = \prod_{I \in \{A,B\}} \exp\left(-\frac{1}{2} Z_I\right) \cdot g_{1,2}(X_i, Y_i) \tag{5b}$$

$$Q_{5,6} = \exp\left(-\frac{1}{2} Z\right) \cdot g_{1,2}(X, Y) \tag{5c}$$

$$Q_7 = \exp\left(-\frac{1}{2} Z\right) \tag{5d}$$

$$Q_8 = d \tag{5e}$$

$$Q_9 = [\cos(\vartheta)]^2 \ , \tag{5f}$$

where

$$g_1(x, y) = \frac{1}{4}\left[\cos\left(\frac{2\pi}{a} x\right) + \cos\left(\frac{2\pi}{a} y\right)\right] + \frac{1}{2} \tag{6a}$$

$$g_2(x, y) = \frac{1}{4}\left[\cos\left(\frac{2\pi}{a} x\right) \cdot \cos\left(\frac{2\pi}{a} y\right)\right] + \frac{1}{2} \ , \tag{6b}$$

incorporate the periodicity of the square-shaped surface lattice with the lattice constant a. As illustrated in Fig. 2, these have been constructed such that symmetry-equivalent points (x, y) in the surface plane result in the same pair of function values $(g_1(x, y),\ g_2(x, y))$, with a detailed account provided in Ref. [32].

2.2 DFT data

Based on the above spherical coordinate system, a discrete set of *ab initio* total-energy data were calculated within DFT by Alducin *et al.* in order to describe the adiabatic interaction of O_2 with a (rigid) Ag(100) surface [31]. Briefly summarized, the set comprises data for 12 different so-called elbow cuts through the PES, *i.e.* for molecular configurations of defined lateral position of the O_2 center of mass (X,Y) and defined molecular orientation (ϑ,φ). Within every elbow, total energies were calculated over

a (Z,d) grid, in which the molecule's distance from the surface Z varies from 0 to 4.5 Å (typically in steps of 0.25 Å) for 10 values of the internuclear distance d (chosen between 0.9 and 2.5 Å). Thus a *regular* (Z, d) grid was constructed containing 2250 energy values of the target PES

$$V_{6D}\left(\boldsymbol{R}_i^{sph}\right) = E_{O_2@Ag(100)}\left(\boldsymbol{R}_i^{sph}\right) - E_{Ag(100)} - E_{O_2}\,, \tag{7}$$

and further augmented by values from the molecular O_2 binding curve for large distances from the surface $Z \geq 4.5$ Å. The *ab initio* total energies of the clean surface ($E_{Ag(100)}$), isolated oxygen molecule (E_{O_2}) and the interacting system ($E_{O_2@Ag(100)}$) were obtained within a plane-wave basis set with a cut-off energy of 515 eV and ultrasoft pseudopotentials as implemented in the VASP code [33–38]. The exchange-correlation energy was calculated within the generalized gradient approximation (GGA) due to Perdew and Wang (PW91) [39], and the Ag(100) surface was modeled in a supercell geometry containing a five-layer slab, a (2×2) surface unit-cell, and a vacuum distance of 20.89 Å [31].

2.3 Continuous PES representations

Based on the DFT data set described above, two different techniques are employed within the present work to obtain PES representations that can be continuously evaluated along with concomitant forces. The prevalent corrugation-reducing procedure (CRP) [17,18] recognizes that a large part of the difficulties behind the interpolation of a six-dimensional function V_{6D} describing the PES of a diatomic at a solid surface arises from the large energy variations connected *e.g.* with the strongly repulsive regions at short molecule-surface distance. Much of this corrugation, however, is equally encountered when the constituent isolated atoms approach the surface. The central idea of CRP lies therefore in decomposing the 6D molecular PES V_{6D} into a superposition of the 3D atom-surface interactions $\mathcal{R}_{A,B}$ for both atoms (at their coordinates in the diatomic) and a smoother function $\mathcal{I}^{CRP}$,

$$V_{6D}^{CRP}\left(\boldsymbol{R}^{sph}, \boldsymbol{R}^{cart}\right) = \mathcal{I}^{CRP}\left(\boldsymbol{R}^{sph}\right) + \mathcal{R}_A\left(\boldsymbol{R}_A\right) + \mathcal{R}_B\left(\boldsymbol{R}_B\right)\,. \tag{8}$$

$\mathcal{I}^{CRP}$ becomes then a more convenient target for the interpolation. In practice, this obviously requires additional *ab initio* data for the construction of continuous representations of $\mathcal{R}_{A,B}$, which simplifies to a single function in the present case of a homonuclear diatomic. However, the lower dimensionality of $\mathcal{R}_{A,B}$ makes this a much simpler task – including a proper incorporation of symmetry [18]. In this like in many preceding works, $\mathcal{I}^{CRP}$ is then obtained for an arbitrary configuration $\boldsymbol{R}^{sph}$ within the range covered by the discrete set $\{\boldsymbol{R}_i^{sph}\}$ for which DFT energies $\{V_{6D}(\boldsymbol{R}_i^{sph})\}$ are available. This is typically done by decoupling the six-dimensional problem into four at most two-dimensional independent interpolation steps, which can be schematically summarized as follows:

1. $\mathcal{I}_0^{CRP}\left(\left\{\boldsymbol{R}_i^{sph}\right\}\right) \xrightarrow{(Z_i,d_i)\text{: splines}} \mathcal{I}_1^{CRP}(Z, d\,;\, \{X_i, Y_i, \vartheta_i, \varphi_i\})$
2. $\mathcal{I}_1^{CRP}(Z, d\,;\, \{X_i, Y_i, \vartheta_i, \varphi_i\}) \xrightarrow{\varphi_i\text{: Fourier}} \mathcal{I}_2^{CRP}(Z, d, \varphi\,;\, \{X_i, Y_i, \vartheta_i\})$
3. $\mathcal{I}_2^{CRP}(Z, d, \varphi\,;\, \{X_i, Y_i, \vartheta_i\}) \xrightarrow{(X_i,Y_i)\text{: Fourier}} \mathcal{I}_3^{CRP}(X, Y, Z, d, \varphi\,;\, \{\vartheta_i\})$

4. $\mathcal{I}_3^{\mathrm{CRP}}(X, Y, Z, d, \varphi\,;\,\{\vartheta_i\}) \xrightarrow{\vartheta_i:\,\mathrm{splines}} \mathcal{I}_4^{\mathrm{CRP}}(X, Y, Z, d, \vartheta, \varphi)$
   with $\mathcal{I}_4^{\mathrm{CRP}}(X, Y, Z, d, \vartheta, \varphi) \equiv \mathcal{I}^{\mathrm{CRP}}(\boldsymbol{R}^{\mathrm{sph}})$.

The interpolation functions employed in steps two to four are chosen according to generally expected energy variation in these degrees of freedom, and are carefully adapted to its symmetry [17,18].

Neural networks (NNs) as the second prevalent interpolation approach are a highly flexible, non-linear model originally inspired by neuroscience [30]. Even with utmost mathematical rigor they are shown to be capable of approximating any PES to – at least in principle – arbitrary accuracy [40,41]. This motivates to target $V_{6\mathrm{D}}$ directly and equally in its full six dimensionality, allowing to capture intertwinement of degrees of freedom which are treated independently in the prevalent interpolation strategy hitherto employed in the CRP context described above. Further unlike the latter, the input data are not required to fall on regular grids, thus enabling the addition of individual points depending on the desired accuracy in certain PES "regions" [26]. Extrapolation capabilities of NNs beyond the coordinate ranges of the input data can also supersede those of the above described individual interpolations due to the inherent limitations of the underlying fixed analytic forms employed in CRP [30]. However, this inherent flexibility comes as a mixed blessing: Correct symmetry properties can only be guaranteed by presenting symmetry adapted coordinates to a NN [26,28,32], like those introduced in Sect. 2.1. The NN thus acts as function $\mathcal{F}^{\mathrm{NN}}(\boldsymbol{Q})$ for the continuous PES representation according to

$$V_{6\mathrm{D}}^{\mathrm{NN}}(\boldsymbol{R}^{\mathrm{cart}}, \boldsymbol{R}^{\mathrm{sph}}) = \mathcal{F}^{\mathrm{NN}}(\boldsymbol{Q}(\boldsymbol{R}^{\mathrm{cart}}, \boldsymbol{R}^{\mathrm{sph}}))\,. \tag{9}$$

In practice and as further detailed in preceding work [25], various multilayer feed-forward NNs of different topologies are fitted (aka "*trained*" in NN lingo) to the DFT input data, after some (166 in the present case) randomly selected entries have been moved from the training into a so-called test set. During the training iterations (aka "*epochs*"), the latter set is employed to monitor the extrapolation abilities. Using the adaptive extended Kalman filter (EKF) algorithm including the modifications described in [25] for training, the sensitivity of the NN is further focused on the energetically presumably most relevant parts of the PES by assigning training weights to the input data according to

$$\omega_{\boldsymbol{Q}_i}\left(V_{6\mathrm{D}}\left(\boldsymbol{R}_i^{\mathrm{sph}}\right)\right) = \alpha\,\exp\left(-\beta\,V_{6\mathrm{D}}\left(\boldsymbol{R}_i^{\mathrm{sph}}\right)\right)\,. \tag{10}$$

The parameters α and β are chosen in the present work so that Eq. (10) maps the energy interval of the DFT data $[-0.25\,\mathrm{eV};\,+2.5\,\mathrm{eV}]$ to

$$\left[\frac{1}{\omega_{\boldsymbol{Q}_i}(+2.5\,\mathrm{eV})};\,\frac{1}{\omega_{\boldsymbol{Q}_i}(-0.25\,\mathrm{eV})}\right] = \left[\frac{1}{500};\,1\right].$$

Out of over 70 different attempts we obtained the best fit presented in Sect. 3.1 below for a $\{9-25-25-1\,ttl\}$ NN topology (see *e.g.* Refs. [25,26] for details on this notation) and the EKF parameters $\lambda(0) = 0.9610$ and $\lambda_0 = 0.99670$.

2.4 Dynamical simulations

The dynamics on both the CRP and NN PESs are analyzed with quasi-classical trajectory calculations that include the initial zero point energy of the O_2 molecule. A classical microcanonical distribution of the internuclear distance d and its conjugate momentum p_d is used for the molecule in the quasi-classical equivalent of its ground rovibrational state, which was found equal to 97.5 meV [31]. All results are derived from the evaluation of 10 000 trajectories, starting at a distance of $Z = 9$ Å from the surface, where the PES value for O_2 at its equilibrium bond length $d_{eq} = 1.24$ Å is zero in both PES representations.

Along the trajectory calculations, the following reaction events are distinguished:

1. dissociation, when the molecule's internuclear distance reaches the value $d = 2.4$ Å ($\approx 2d_{eq}$) with a positive radial velocity;
2. reflection, when the molecular center reaches the initial starting distance of 9 Å above the surface and with a positive Z-velocity; and
3. molecular trapping, when the molecule is neither dissociated or reflected after 15 ps.

This classification is the basis to arrive at the central kinetic parameters analyzed in this work, namely the dissociative sticking coefficient and molecular trapping probability, defined as averages over the obtained trajectory data, *i.e.* the fraction of correspondingly classified trajectories over the total simulated trajectories for the given initial kinetic energy.

2.5 Global minima search

The low computational cost associated with the evaluation of energies and forces on the continuous PES representations allows for extensive configurational sampling in the search for energetically low lying minima. We thus employ a rather brute-force scheme that involves a large number of individual independent geometry optimizations starting from different initial configurations. In these initial configurations the O_2 molecule has random lateral positions within the irreducible wedge of the fcc(100) surface unit-cell (*cf.* Fig. 2), random distances from the surface and bond lengths between 1.0–2.5 Å and any angular orientation. Each configuration is subject to local geometry optimization within the *Atomic Simulation Environment* (ASE) [42] until residual forces on the O atoms fall below 0.001 eV/Å. The thus optimized geometries are identified as on-surface adsorption states, if the O_2 distance from the surface is positive ($Z > 0$) and its bond length falls within the range [1 Å, 2.5 Å]. Despite the use of symmetry-reduced initial configurations, minimization paths can easily lead out of the irreducible wedge and thus yield potentially symmetry-equivalent minima. The symmetry-adapted coordinates described in Sect. 2.1 were correspondingly used to conveniently compare to results from previous iterations and finally establish the database of unique adsorption states discussed below. The rate with which new such states were added to the set was continuously monitored during the sampling run, and used as a criterion to stop the search. After 10,000 geometry optimizations on each PES representation, this criterion suggested that all inequivalent low-energy minima had been identified.

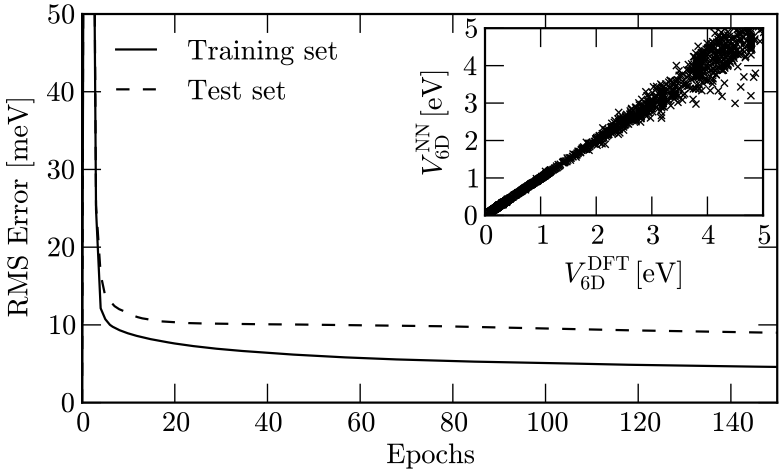

Fig. 3. Evolution of the training and test root mean square error (RMSE) as a function of the number of *epochs* performed during the Neural Network training. The inset shows the resulting Neural Network energies with respect to the corresponding DFT input data.

3. Results and discussion

3.1 Interpolation errors *vs.* reaction probabilities

The reliability assessment of a continuous PES representation within the divide-and-conquer approach is hitherto commonly restricted to an evaluation of the interpolation or fitting quality. Within the CRP strategy, the accuracy is correspondingly checked by comparing interpolated values with calculated DFT data not included in the interpolation procedure. In the earlier work of Alducin *et al.* [31] such checks indicated errors to fall below 100 meV for a number of different molecular configurations at distances $Z \geq 1.5$ Å. Within the NN approach this kind of performance check is already included in the fitting procedure itself by monitoring the evolution of the root mean square error (RMSE) with each epoch, *cf.* Sect. 2.3. For the best fit achieved in the present work the latter is depicted in Fig. 3, arriving at train and test set RMSEs of 4.59 meV and 8.99 meV, respectively, when terminating the NN training after 150 epochs. The inset of Fig. 3 shows the resulting deviation of the fitted energies to the reference DFT values, which – as expected by the choice of the assigned weights – increases in the more repulsive (and allegedly dynamically less relevant) regions of the PES.

The errors obtained with both approaches are *en par*, if not smaller than those reported in a number of preceding divide-and-conquer studies, and would generally be considered as reflecting faithful state-of-the-art PES representations. Still, such assessment (even though standard) is obviously only based on those points included in the *ab initio* data set, which in the present case does not include lower-symmetry points, see the discussion below. That this represents a major shortcoming is prominently illustrated by the different results obtained in the dynamical simulations on these two PESs summarized in Fig. 4: These differences center on the dissociative adsorption dynamics of the system, whereas quite similar results are obtained for molecular trapping at low incidence energies. For the normal incidence case shown in Fig. 4, this specifically amounts to an onset of the dissociative sticking probability at about 1.05 eV in the CRP case, while the onset is delayed to 1.6 eV for the NN representation. With

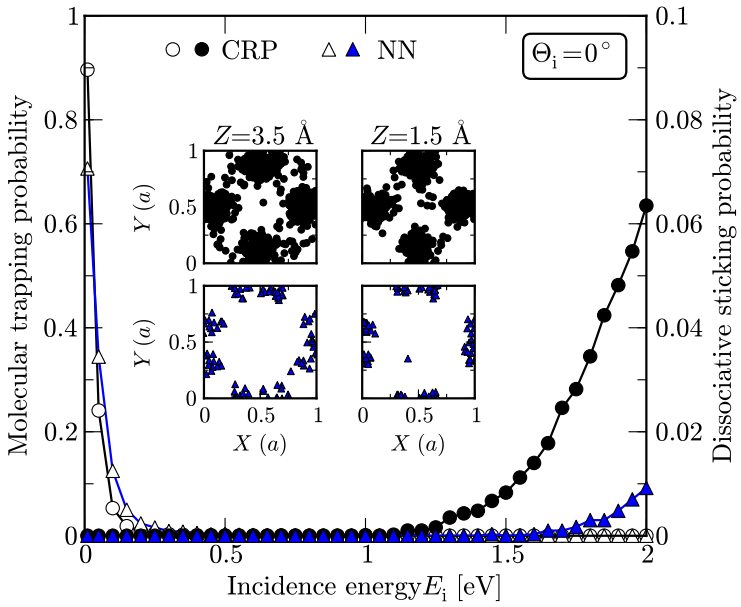

Fig. 4. Molecular trapping (open symbols) and dissociative sticking (filled symbols) probabilities of O_2 impinging at normal incidence $\Theta_i = 0^\circ$ on the Ag(100) surface as a function of the incidence kinetic energy E_i. The insets show the position of the molecular center over the unit cell, when the dissociating molecules are at $Z = 3.5$ Å (left panels) and $Z = 1.5$ Å (right panels) for an incidence energy of 2.0 eV. Note that the same coordinate system as in Fig. 2 is used, *i.e.* surface atoms are located at the corners of the depicted unit cell. In all cases, circles and triangles correspond to data obtained for the CRP- and NN-PES representation, respectively.

a monotonously rising dissociative sticking probability, this shift in the onset leads to much higher values in the CRP case at higher incidence energies, which *e.g.* with 0.06 at $E_i = 2.0$ eV surpasses the equivalent NN probability by more than 500%. The same trend is observed for various incidence angles tested, indicating a much higher reactivity of the CRP representation in general with the dissociative sticking probability already starting to rise at significantly lower incidence kinetic energies.

3.2 Differences in reaction mechanism

In terms of absolute values for the sticking probability, the differences between the two approaches might not appear too worrisome at first sight. Due to the large number of trajectories employed in the averaging, they are, however, statistically significant. As such, the huge relative discrepancies question the divide-and-conquer approach in its very core regime inaccessible to the alternative direct AIMD ansatz, namely the quantitative determination of very low reaction probabilities.

Since both PES representations are based on the exact same DFT data, the differences must derive from interpolation deficiencies that go unnoticed in the traditional quality indicators based on fitting errors. As a first step towards understanding the source of the problem and establishing protocols to overcome it, we focus on an analysis of the dissociation mechanism. Ideally, this will provide insight into which parts or topological features of the PES are central to the sticking coefficient. In this respect, the original work on the CRP PES by Alducin *et al.* emphasized the role of high energy bar-

riers of about 1.05 eV between bridge and hollow sites at a distance of 1–2 Å above the surface [31]. They reflect molecules with low incidence energies, while molecules with a kinetic energy large enough to surmount them are subsequently capable of sufficiently approaching the surface to finally dissociate in the vicinity of the Ag(100) bridge sites.

Meticulous searches for minimum energy paths performed *via* the Nudged Elastic Band (NEB) method within the present work, revealed such barriers to also exist along the most energetically favorable path traced towards dissociation within the NN representation. This suggests that the latter yields at least a qualitatively similar reaction mechanism as the CRP representation; a suspicion that we find fully confirmed by the trajectory data shown in the insets of Fig. 4. Analyzed is the O_2 center of mass position over the surface unit-cell of ultimately dissociating molecules as they first reach a surface distance of $Z = 3.5$ Å (left panels) and $Z = 1.5$ Å (right panels) for an incidence energy of 2.0 eV. Indeed, in both PES representations the molecules predominantly accumulate around the bridge position, underscoring the relevance of this PES "region" for the dissociation mechanism in both representations. However, in the NN case (reflecting the lower dissociative sticking probability) this is a significantly smaller number of trajectories. Furthermore, by comparing the distributions of the trajectories in both insets in detail, one notices that in the CRP case dissociating trajectories are found to be homogeneously distributed within the vicinity of the bridge sites, whereas for the NN particularly in the direction towards the hollow sites no dissociating trajectories can be found. This indicates PES interpolation deficiencies in this area to be primarily responsible for the differing reaction probabilities obtained with the two representations.

3.3 Picturing the PES "landscape": a visual comparison

A most straightforward way to investigate if and how the two interpolation approaches give rise to different topologies in those PES regions that the preceding analysis identified as most influential for the dynamical behavior is to visually compare suitable two-dimensional (2D) cuts through the two 6D PES representations and include the actual *ab initio* data. Figure 5 depicts three corresponding cuts: A (d–Z) elbow cut over the bridge site and for alignment of the molecular axis along the [001] direction ($\vartheta = \varphi = 90°$), *i.e.* in the direction of the neighboring hollow sites; a (ϑ–φ) angular plot over the bridge site and at a surface distance of 1.5 Å, *i.e.* somewhere at the Z of the dissociation barriers; and a (X–Y) lateral corrugation plot at the same distance from the surface and for the most favorable angular orientation identified in the (ϑ–φ) cut (that again points towards the hollow sites). Additionally shown are the coordinates of the actual DFT data grid in each 2D cut. By construction, the DFT values at these grid points are exactly reproduced by the interpolation technique employed in the CRP approach (*cf.* Sect. 2.3). In contrast, within the NN representation they are only fitted and the marker size at the grid point reflects the corresponding error.

Consistent with the weight factors assigned upon training and with the initially discussed small global fitting errors, specifically the dynamically relevant low energy points are very well reproduced by the NN. At the high density of DFT data points in the (d–Z) elbow plot, this (or the exact reproduction of the DFT values in the CRP case) is enough to rather unambiguously determine the continuous representation within the

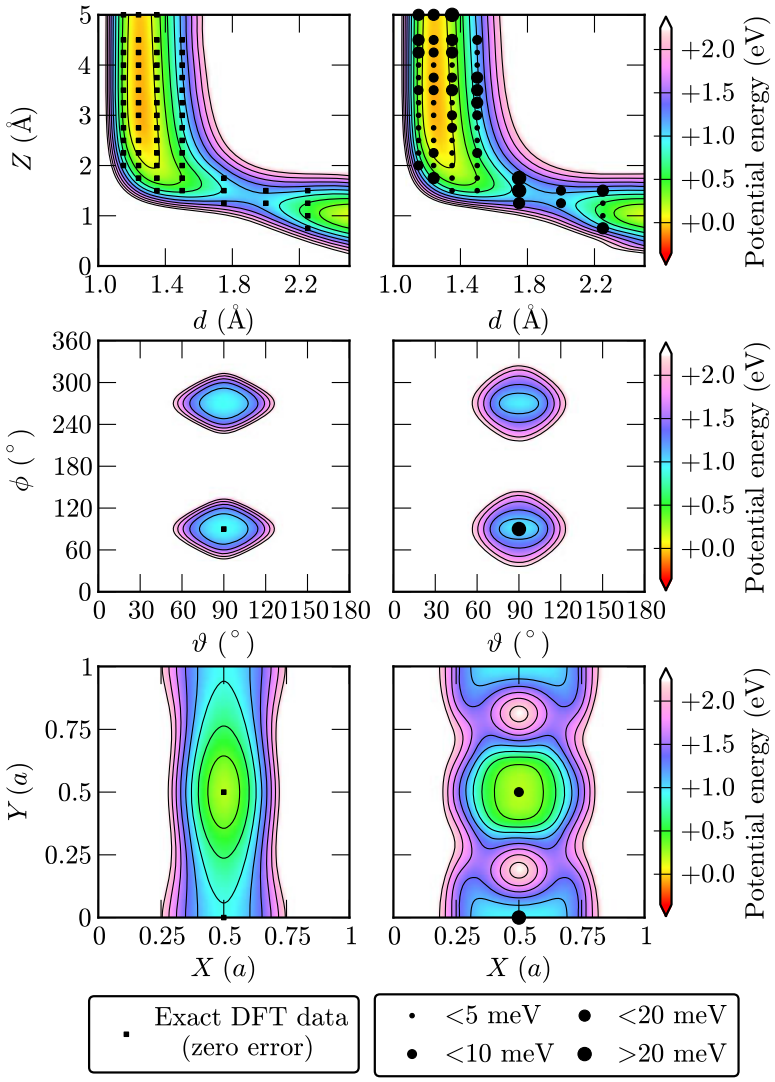

Fig. 5. Equivalent representations of the CRP (left) and NN (right) potential energy surfaces. All panels represent two-dimensional cuts through the 6D PESs: for $X = 0.5\,a$, $Y = 0$ and $\vartheta = \varphi = 90°$ (top); for $X = 0.5\,a$, $Y = 0$, $Z = 1.5$ Å and $d = 1.75$ Å (middle); for $Z = 1.5$ Å, $d = 1.75$ Å and $\vartheta = \varphi = 90°$ (bottom). The black points outline the underlying DFT grid with the marker shape and size illustrating the corresponding errors of the interpolated representation as explained in the figure's legend.

corresponding plane, resulting in the remarkable resemblance of both plots shown in the upper panels of Fig. 5. This also holds for all other eleven elbows contained in the DFT data set (not shown). Despite the much sparser supporting grid (of in fact only five inequivalent DFT data points), the same still seems to be valid in the angular (ϑ–φ) plane shown in the middle panels of Fig. 5 (where only a single of the five DFT points falls within the depicted energy range). In the lateral (X–Y) plane, however, along which DFT sampling is noticeably "poor", both representations exhibit significant differences in the levels of corrugation and overall features of the PES landscape, with the NN PES featuring an overall more complex topology. Similar conclusions are drawn from a large number of 2D cuts analogous to those of Fig. 5 for which (some) DFT data points are available. These cuts generally reflect a higher degree of "creativ-

ity" of the NN in describing the PES within areas that are sparsely supported by *ab initio* data.

In principle, differences in the description of sparsely supported PES areas are not surprising, but in fact to be expected: If imagining the continuous PES to be like a carpet that has been nailed to the floor at specific points (by locally minimizing the RMSE with respect to the DFT data), "bumps" and "folds" can freely reveal themselves "between" the (more or less) fixed points within both approaches. That there are more such "bumps" and "folds" in the NN case is hereby not related to targeting the more corrugated V_{6D} with the NN rather than targeting the smoother interpolation function $\mathcal{I}^{CRP}$ used in CRP. Similar to recent work by Ludwig and Vlachos [43], but including proper treatment of symmetry, we have also set an equivalent $\tilde{\mathcal{F}}^{NN}(\{\boldsymbol{Q}_i(\boldsymbol{R}_i^{cart}, \boldsymbol{R}_i^{sph})\})$ function as the target for the global fitting in symmetry adapted coordinate space with the NN (*cf.* Sect. 2). Pronounced differences in the lateral dimensions, however, are still obtained for the different representations. Consequently, the disentanglement into independent interpolation steps employed in CRP (*cf.* Sect. 2.3) is instead identified as the cause for the altogether smoother CRP-PES. In particular, the Fourier interpolation in (X, Y) does include physical assumptions about the PES behavior in these degrees of freedom which are absent in the NN case. The aforementioned mixed blessing of the latter is thus nicely exemplified: On the one hand, it can produce the observed "creative" PES representations. On the other hand, this can also allow to better capture more complex PES topologies that are correlationally induced by all six molecular coordinates and which are then beyond the flexibility of the functional form of the Fourier interpolation. The latter is *e.g.* reflected by the lower root mean square error of the NN test set described in Sect. 3.1.

Altogether, the 2D cuts presented in Fig. 5 nicely complement the understanding derived from the mechanistic analysis: The $(d\text{-}Z)$ elbow cuts over the bridge site confirm that both PES representations yield similar barriers for this dissociation path that wants the molecular axis parallel to the surface and steered into a side-on orientation along the [001] direction. In contrast, the markedly different PES topologies encountered in the XY plane suggest that the consequences on the sticking probabilities can be attributed to the influence of "bumps" and "folds" of both representations "in between" these elbows. We turn in the following therefore, to locating such topological PES features, and prominently the minima, which as we will show not only helps to further pinpoint and understand the source of the dynamical discrepancies, but also provides a general protocol to assess the PES interpolation beyond the level of fitting errors.

3.4 PES topology: in search of local minima

When applying the global search scheme described in Sect. 2.5 to both PES representations a significantly different and surprisingly high number of local minima is obtained. 21 and 7 bonded (with $V_{6D} < 0$) molecular configurations are detected for the CRP and NN PESs, respectively. Some of these minima are rather shallow minima on the continuous representations, and thus not all of them are likely to correspond to physically meaningful adsorptive structures.

These minima are plotted in Fig. 6 as a function of their vertical distance Z from the surface. A detailed analysis of trajectory ensembles (*vide infra*) excludes the en-

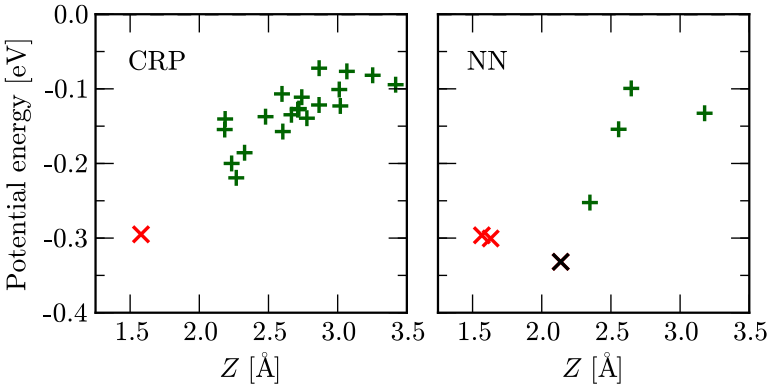

Fig. 6. Potential energy of the local minima configurations detected for the CRP (left) and NN (right) PES representations as a function of their corresponding distance from the surface, Z. In both cases, different symbols are used to conveniently set apart the low-energy structures (crosses) from the more 'shallow' minima located further away from the surface (plusses). Note in particular, the NN global minimum (marked in black) that has no counterpart in the CRP representation.

trance channel as having a major influence on the dynamics by effectively steering the impinging molecules into orientations or impact sites of different reactivity within the two PES representations. We therefore suspect minima closest to the surface to have the biggest influence on the dissociation dynamics (if there is any), imagining them to be most effective for an activation of the molecular bond, *i.e.* transfer of energy into the d coordinate. Clearly separated from the rest, only one such minimum is observed for the CRP representation at a surface distance of approximately 1.58 Å and an adsorption energy of *ca.* −300 meV. This minimum is scrupulously reproduced within the NN representation, which, however, exhibits two additional minima (at $Z = 1.63$ Å and 2.14 Å) in a similar energy range. Since one of these corresponds in fact to even the unique global minimum of the NN representation $M_{\mathrm{NN}} = (X_{\mathrm{min}} = 0.25\,a, Y_{\mathrm{min}} = 0.5\,a, Z_{\mathrm{min}} = 2.14$ Å, $d_{\mathrm{min}} = 1.28$ Å, $\vartheta_{\mathrm{min}} = 90°, \varphi_{\mathrm{min}} = 90°)$ in the irreducible wedge (*cf.* Fig. 2), we start by focusing our analysis on its influence.

Returning to the examination of 2D cuts through the PES representations, the upper part of Fig. 7 visualizes similarly large differences in the lateral degrees of freedom in the vicinity of this NN global minimum as discussed already in Sect. 3.3. In order to analyze the influence on the dynamics, we have also included (X, Y) coordinates of molecules with $E_i = 2$ eV that pass through the close vicinity of this plane as detailed in the figure's caption. Other than in the inset of Fig. 4, we now concentrate on all those trajectories that dissociate on the CRP PES and whose equivalent counterparts (*i.e.* starting from the exact same initial conditions) are reflected in the case of the NN. This particular choice of depicted trajectories (CRP dissociating and NN reflected) indicates that the dynamical discrepancies are not to be traced back to effects of molecular steering, but are rather due to the different topology of the PES representations in regions close to the surface. Still, this ensemble does not pass through M_{NN} itself, such that the minimum itself can not directly be held responsible for their radically different outcome. Instead, the trajectory distribution is more or less centered around repulsive "bumps" only existing in the NN representation shown in Fig. 7 at $(0.5\,a, 0.5\,a \pm 0.25\,a, Z_{\mathrm{min}}, d_{\mathrm{min}}, \vartheta_{\mathrm{min}}, \varphi_{\mathrm{min}})$. Both "bumps" can be identified with

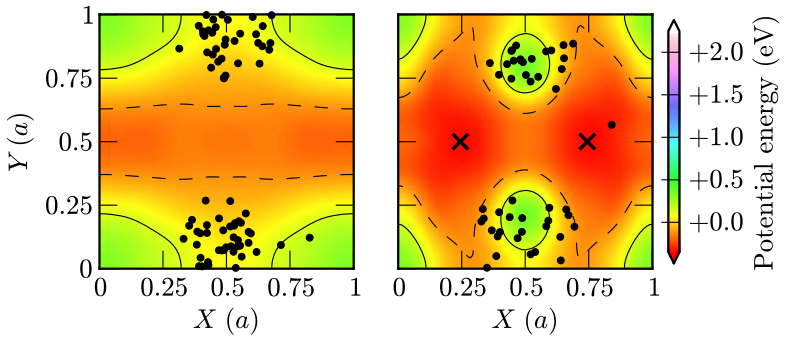

Fig. 7. Equivalent two-dimensional cuts of the CRP (left) and NN (right) PES representations similar to the lower panel of Fig. 5. The (X–Y) plots correspond to $Z_{\min}$, $d_{\min}$, $\vartheta_{\min}$ and $\varphi_{\min}$, *i.e.* they are cuts along the lateral plane through the NN global minimum at ($X_{\min} = 0.25\,a$, $Y_{\min} = 0.5\,a$, $Z_{\min} = 2.14$ Å, $d_{\min} = 1.28$ Å, $\vartheta_{\min} = 90°$, $\varphi_{\min} = 90°$) in the irreducible wedge (*cf.* Fig. 2). Note that due to the symmetry of the angular coordinates ($\vartheta_{\min}, \varphi_{\min}$), a horizontal and vertical mirror plane perpendicular to the surface through the hollow site (*i.e.* the center of the panels) is preserved from the clean Ag(100) surface symmetry within these cuts. Consequently, there is also a symmetry equivalent counterpart of the NN global minimum at ($\tilde{X}_{\min} = a - X_{\min}, Y_{\min}, Z_{\min}, d_{\min}, \vartheta_{\min}, \varphi_{\min}$). Both minima are marked by black crosses. The black circles correspond to trajectory data and show the respective positions of the molecular center in this cut plane (folded back into the unit cell) for molecules that pass closely through this cut plane, *i.e.* $(Z, d, \vartheta, \varphi) \in [Z_{\min}, d_{\min} \pm 0.05$ Å, $\vartheta_{\min} \pm 30°, \varphi_{\min} \pm 20°]$. Other than in the inset of Fig. 4), only equivalent trajectories starting from the same initial conditions with an incidence energy of 2.0 eV are included that dissociate on the CRP (left) but are reflected on the NN PESs (right).

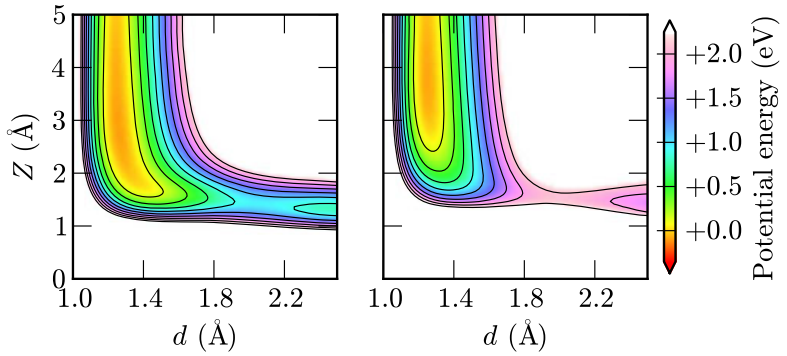

Fig. 8. Equivalent two-dimensional cuts of the CRP (left) and NN (right) PES representations similar to the upper panel of Fig. 5. The (d–Z) elbow plots are shown for $X_{\min}$, $Y_{\min}$, $\vartheta_{\min}$ and $\varphi_{\min} - 90°$, *i.e.* the coordinates of the "bumps" identified in Fig. 7 backfolded in the irreducible wedge (see text).

a symmetry equivalent representative $B_{\mathrm{NN}} = (X_{\min}, Y_{\min}, Z_{\min}, d_{\min}, \vartheta_{\min}, \varphi_{\min} - 90°)$ in the irreducible wedge (*cf.* Fig. 2) with $V_{6\mathrm{D}}^{\mathrm{NN}}(B_{\mathrm{NN}}) \approx +0.3$ eV. This motivates picturing the NN PES representation like in Sect. 3.3 at this "suspicious location" within the close vicinity of M_{NN} also in the other degrees of freedom. Figure 8 compares CRP and NN elbow plots for a corresponding molecular configuration. While the CRP PES still shows a dissociation path with a barrier of about 1 eV equivalent to the one directly encountered at the bridge site (*cf.* upper part of Fig. 5), its NN counterpart is by more than 1 eV steeper. Very similar trends are also observed for other elbows corresponding to different angular orientations of the molecule. For molecules therefore with a kinetic energy just sufficient to traverse the minimum energy path all these configu-

rations would already lead to dissociation within the CRP PES yet be repelled by the much higher barriers on the NN PES.

This fully rationalizes the observed differences in reaction probabilities shown in Fig. 4 in terms of the differing degree of creativity for the CRP and NN pictures discussed previously: While the DFT data grid is dense enough to yield the same qualitative dissociation mechanism in both representations, additional "bumps" in the NN representation yield a much smaller lateral extent of this dominant dissociation pathway and thereby lead to a significantly reduced dissociation probability. Additional single-point DFT calculations performed in these regions indeed reveal large representation errors of ≈ 240 meV and confirm the interpretation of the "bumps" as unphysical products of the NN fit. Correspondingly large errors associated with the NN local minima (of which a detailed account may be found in supplementary materials) further suggest that the additional "bumps" and "folds" tend to go hand in hand, thus also resulting in a differing amount of extremal points on the PES, as indicated in the present case by the differing number of low-energy minima identified on the NN and CRP PESs.

In a more general context however, whether such topological features are real or spurious – and correspondingly which PES representation is to be trusted more – cannot be answered *a priori*, but only by iteratively refining the DFT data grid and thus successively reducing the interpolation freedom. Preceding any detailed dynamical simulations, a static global minimum search as performed here appears therefore as a suitable and computationally undemanding general protocol to assess the interpolation quality beyond the level of an arbitrarily chosen test set of *ab initio* data: Particularly PES regions around the identified minima should be supported by a sufficiently dense DFT data grid – if not in the original data set, then at least through iterative refinement. While not at all being a conceptual limitation of the central idea behind CRP, this is more conveniently carried out within the present NN implementation at the moment and also more important for the latter at least in the present case.

4. Conclusions and outlook

In summary, we have presented a systematic comparison of continuous potential energy surface (PES) representations commonly used in gas-surface dynamics within the divide-and-conquer approach. Employing the exact same set of *ab initio* data [31] for the showcase system O_2 on Ag(100) such six-dimensional PES representations according to two prevalent schemes, namely the Corrugation-Reducing Procedure (CRP) and Neural Networks (NNs), were found to yield largely differing dissociative sticking probabilities, despite flawlessly passing commonly employed representation quality checks. In particular for statistical quantities with low probabilities (such as the dissociative sticking probability focused on here) direct *ab initio* molecular dynamics is unlikely to replace the divide-and-conquer approach in the near future. This being the case, the reported results are particularly irritating and dictate the development of protocols to more reliably assess and refine the representation quality.

To this end and complementing an evaluation through explicit dynamical trajectory simulations we emphasize the value of a static evaluation of the obtained PES. In the spirit of Eyring and Polanyi, this concerns foremost the imperative visualization

along suitable 2D cuts. In the present case this allowed to trace the differences in reaction probabilities back to systematic differences of the two approaches in areas that are only sparsely sampled by DFT input data. With the latter conventionally concentrated in (Z, d) elbow cuts, this applies especially to lateral degrees of freedom, where we found the NN PES representation to exhibit a much more complex topology with additional "bumps" and "folds". In contrast, the physical assumptions embodied in the Fourier interpolation that is used for these lateral degrees of freedom within the decoupled, at most two-dimensional interpolation steps employed in prevalent CRP versions necessarily yield a much smoother description.

For the showcase system, the additional "bumps" were shown to lead to a significantly reduced lateral extent of the dominant dissociation pathway and thereby to the much reduced dissociation probability obtained with the NN PES representation. Both here and in general it is *a priori* impossible to judge which of the two strategies yields the more reliable global representation: The flexibility of the NN approach, directly targeting the six-dimensional PES and its full topology, can allow to foresee/reproduce PES features which the CRP approach with its decoupling strategy systematically excludes. This can extend to (technical) inconsistencies of the underlying *ab initio* data, which spin-polarized density-functional calculations for systems – like the present one – that exhibit a spin transition are particularly prone to. On the other hand, this high flexibility brings along the risk of a high "creativity" and spurious artifacts in sparsely sampled PES regions.

Ultimately, the only reliable answer as to the more faithful representation can be given by explicit *ab initio* molecular dynamics simulations. Yet, this is precisely what the divide-and-conquer approach tries to avoid. Alternatively, one could always argue to construct "better" *ab initio* training sets, *e.g.* including more data at low-symmetry sites. In an increasing dimensionality of the problem this becomes a more and more delicate task with unclear outcome though. In our view, a more controlled approach centers on an iterative refinement of the input data density in sparsely sampled PES areas and in particular in those that are relevant for the dynamics. In understanding the role of additional "bumps" and "folds" created by the NN approach, we propose that a global minima search provides a most helpful (and practically manageable) tool to guiding such a refinement endeavor. In a first place one would simply want a continuous PES representation to yield a qualitatively correct topology and therefore knowledge of the representation's low-energy minima always comprises a good starting point. Much more, however, the added value of locating low-energy regions of the PES lies in their general likelihood of influencing the system's dynamics. Even if this is not the case – as for the dissociative sticking studied here – the aforementioned "bumps" and "folds" (aka topological features) necessarily go hand in hand. A global search for the latter is in this respect a useful (and numerically undemanding) complement to a dynamical trajectory analysis on the PES representation, which would tediously have to be repeated for different incidence energies or angles. The knowledge of the minima can then also directly be employed to steer a visual PES exploration by focusing on 2D cuts that go through their positions. As we have demonstrated here, such a look in the vicinity of these minima can reveal "bumps", which in case of sparse DFT data sampling around the latter quickly raises suspicions about them being artifacts of the continuous representation. In this manner, regions of the PES are identified for which adding further

data points and pinpointing the PES "carpet" will most effectively increase the reliability of the continuous representation. This holds in particular when not having a second such representation at hands for comparison, which after all corresponds to the usual working situation.

References

1. H. Eyring and M. Polanyi, Z. Phys. Chem. Abt. B **12** (1931) 279.
2. M. Born and R. Oppenheimer, Ann. Phys. **20** (1927) 457, DOI:10.1002/andp.19273892002.
3. "The Nobel Prize in Chemistry 1998 awarded to W. Kohn, and J. Pople", available from world wide web: http://www.nobelprize.org/nobel_prizes/chemistry/laureates/1998 [cited February, 1, 2013].
4. G.-J. Kroes, Science **321** (2008) 794, DOI:10.1126/science.1157717.
5. R. Diez Muino and H. F. Busnengo (Eds.), "Dynamics of Gas-Surface Interactions: Atomic-Level Understanding of Scattering Processes at Surfaces", Springer Series in Surface Science, Berlin (2013).
6. T. J. Frankcombe, M. A. Collins, and D. H. Zhang, J. Chem. Phys. **137** (2012) 144701, DOI:10.1063/1.4757149.
7. A. Groß and M. Scheffler, Prog. Surf. Sci. **53** (1997) 187, DOI:10.1016/S0079-6816(96)00016-0.
8. A. Groß, Surf. Sci. Rep. **32** (1998) 291, DOI:10.1016/S0167-5729(98)00008-9.
9. G.-J. Kroes, A. Groß, G.-J. Baerends, M. Scheffler, and D. A. McCormack, Acc. Chem. Res. **35**, (2002) 193, DOI:10.1021/ar010104u.
10. J. H. McCreery and G. Wolken Jr, J. Chem. Phys. **63** (1975) 2340, DOI:10.1063/1.431663.
11. J. H. McCreery and G. Wolken Jr, J. Chem. Phys. **67** (1977) 2551, DOI:10.1063/1.435222.
12. L. Martin-Gondre, C. Crespos, P. Larrégaray, J. C. Rayez, B. van Ootegem, and D. Conte, Chem. Phys. Lett. **471** (2009) 136, DOI:10.1016/j.cplett.2009.01.046.
13. L. Martin-Gondre, C. Crespos, P. Larrégaray, J. C. Rayez, D. Conte, and B. van Ootegem, Chem. Phys. **367** (2010) 146, DOI:10.1016/j.chemphys.2009.11.012.
14. A. Groß and A. Dianat, Phys. Rev. Lett. **98** (2007) 206107, DOI:10.1103/PhysRevLett.98.206107.
15. A. Groß, ChemPhysChem **11** (2010) 1374, DOI:10.1002/cphc.200900818.
16. G.-J. Kroes, Prog. Surf. Sci. **60** (1999) 1, DOI:10.1016/S0079-6816(99)00006-4.
17. H. F. Busnengo, W. Dong, and A. Salin, Chem. Phys. Lett. **320** (2000) 328, DOI:10.1016/S0009-2614(00)00239-6.
18. H. F. Busnengo, A. Salin, and W. Dong, J. Chem. Phys. **112** (2000) 7641, DOI:10.1063/1.481377.
19. R. A. Olsen, H. F. Busnengo, A. Salin, M. F. Somers, G.-J. Kroes, and E. J. Baerends, J. Chem. Phys. **116** (2002) 3841, DOI:10.1063/1.1446852.
20. C. Crespos, M. A. Collins, E. Pijper, and G.-J. Kroes, Chem. Phys. Lett. **376** (2003) 566, DOI:10.1016/S0009-2614(03)01033-9.
21. C. Crespos, M. A. Collins, E. Pijper, and G.-J. Kroes, J. Chem. Phys. **120** (2004) 2392, DOI:10.1063/1.1637337.
22. P. N. Abufager, C. Crespos, and H. F. Busnengo, Phys. Chem. Chem. Phys. **18** (2007) 2258, DOI:10.1039/B617209A.
23. A. Groß, A. Eichler, J. Hafner, M. J. Mehl, and D. A. Papaconstantopoulos, J. Chem. Phys. **124** (2006) 174713, DOI:10.1063/1.2192512.
24. S. Lorenz, A. Groß, and M. Scheffler, Chem. Phys. Lett. **395** (2004) 210, DOI:10.1016/j.cplett.2004.07.076.
25. S. Lorenz, M. Scheffler, and A. Groß, Phys. Rev. B **73** (2006) 115431, DOI:10.1103/PhysRevB.73.115431.
26. J. Behler, S. Lorenz, and K. Reuter, J. Chem. Phys **127** (2007) 014705, DOI:10.1063/1.2746232.

27. J. Meyer and K. Reuter, New J. Phys. **13** (2011) 085010, DOI:10.1088/1367-2630/13/8/085010, arXiv:1104.4212[cond-mat].
28. I. Goikoetxea, J. Beltrán, J. Meyer, M. Alducin, J. I. Juaristi, and K. Reuter, New J. Phys. **14** (2012) 013050, DOI:10.1088/1367-2630/14/1/013050 arXiv:1201.5514[cond-mat].
29. J. B. Witkoskie and D. J. Doren, J. Chem. Theory Comput. **1** (2005) 14 DOI:10.1021/ct049976i.
30. J. Behler, Phys. Chem. Chem. Phys. **13** (2011) 17930, DOI:10.1039/C1CP21668F.
31. M. Alducin, H. F. Busnengo, and R. Diez Muino, J. Chem. Phys. **129** (2008) 224702, DOI:10.1063/1.3012354.
32. J. Meyer, *Ab initio* Modeling of Energy Dissipation during Chemical Reactions at Transition Metal Surfaces, Ph.D. thesis, Freie Universität Berlin (2012), available from world wide web: http://www.diss.fu-berlin.de/diss/receive/FUDISS_thesis_000000036188 [cited February, 1, 2013].
33. G. Kresse and J. Hafner, Phys. Rev. B **47** (1993) 558, DOI:10.1103/PhysRevB.47.558.
34. G. Kresse and J. Hafner, Phys. Rev. B **49** (1994) 14251, DOI:10.1103/PhysRevB.49.14251.
35. G. Kresse and J. Furthmüller, Phys. Rev. B **54** (1996) 11169, DOI:10.1103/PhysRevB.54.11169.
36. G. Kresse and J. Furthmüller, Comp. Mater. Sci. **6** (1996) 15, DOI:10.1016/0927-0256(96)00008-0.
37. D. Vanderbilt, Phys. Rev. B **41** (1990) 7892, DOI:10.1103/PhysRevB.41.7892.
38. G. Kresse and J. Hafner, J. Phys.-Condens. Mat. **6** (1994) 8245, DOI:10.1088/0953-8984/6/40/015.
39. J. P. Perdew and Y. Wang, Phys. Rev. B **45** (1992) 13244, DOI:10.1103/PhysRevB.45.13244.
40. G. Cybenko, Math. Control Signal. Syst. **2** (1989) 303, DOI:10.1007/BF02551274.
41. K. Hornik, M. Stinchcombe, and H. White, Neural Networks **2** (1989) 359, DOI:10.1016/0893-6080(89)90020-8.
42. S. R. Bahn and K. W. Jacobsen, Comput. Sci. Eng. **4** (2002) 56, DOI:10.1109/5992.998641.
43. J. Ludwig and D. G. Vlachos, J. Chem. Phys. **127** (2007) 154716, DOI:10.1063/1.2794338.

Paper #2

Fingerprints of energy dissipation for exothermic surface chemical reactions: O_2 on Pd(100). V. J. Bukas, S. Mitra, J. Meyer and K. Reuter; J. Chem. Phys. **143**, 034705 (2015).

THE JOURNAL OF CHEMICAL PHYSICS **143**, 034705 (2015)

Fingerprints of energy dissipation for exothermic surface chemical reactions: O_2 on Pd(100)

Vanessa J. Bukas,[1,a)] Shubhrajyoti Mitra,[1] Jörg Meyer,[2] and Karsten Reuter[1,3]
[1]*Chair for Theoretical Chemistry and Catalysis Research Center, Technische Universität München, Lichtenbergstr. 4, D-85747 Garching, Germany*
[2]*Gorlaeus Laboratories, Leiden Institute of Chemistry, Leiden University, P.O. Box 9502, 2300 RA Leiden, The Netherlands*
[3]*SUNCAT Center for Interface Science and Catalysis, SLAC National Accelerator Laboratory and Stanford University (USA), 443 Via Ortega, Stanford, California 94035-4300, USA*

(Received 27 May 2015; accepted 7 July 2015; published online 20 July 2015)

We present first-principles calculations of the sticking coefficient of O_2 at Pd(100) to assess the effect of phononic energy dissipation on this kinetic parameter. For this, we augment dynamical simulations on six-dimensional potential energy surfaces (PESs) representing the molecular degrees of freedom with various effective accounts of surface mobility. In comparison to the prevalent frozen-surface approach, energy dissipation is found to qualitatively affect the calculated sticking curves. At the level of a generalized Langevin oscillator model, we achieve good agreement with experimental data. The agreement is similarly reached for PESs based on two different semi-local density-functional theory functionals. This robustness of the simulated sticking curve does not extend to the underlying adsorption mechanism, which is predominantly directly dissociative for one functional or molecularly trapped for the other. Completely different adsorption mechanisms therewith lead to rather similar sticking curves that agree equally well with the experimental data. This highlights the danger of the prevalent practice to extract corresponding mechanistic details from simple fingerprints of measured sticking data for such exothermic surface reactions. © *2015 AIP Publishing LLC.* [http://dx.doi.org/10.1063/1.4926989]

I. INTRODUCTION

Accurate knowledge of the sticking coefficient of molecules at transition metal surfaces is generally valuable in view of the relevance of this kinetic parameter in a wide range of applications such as heterogeneous catalysis. On more reactive surfaces (often desirable), dissociation can already happen alongside the adsorption process. Sticking data may then further provide information on the underlying adsorption mechanism. On the other hand, a sticking coefficient is an averaged kinetic quantity, comprising contributions from initially varying translational and rotational molecular impingement. To what extent sticking data really reflect mechanistic details is thus an open question.[1] From a modeling perspective, there is vice versa the question of how well these underlying details need to be described to arrive at reliable sticking coefficients that can in turn, e.g., be employed in microkinetic models.[2]

Aiming to answer these questions, intense fundamental research has been conducted to obtain an atomic-scale understanding of the reaction pathways and dynamics governing the adsorption process. Supersonic molecular beam techniques at low-index single crystal surfaces have made an unequivocal contribution in this respect, providing sticking coefficient data for a wide range of well-defined initial conditions of incidence energy and angle, as well as resolved rotational or vibrational state.[3] In terms of dissociative adsorption, corresponding data have been traditionally analyzed to distinguish regimes of direct or indirect adsorption.[4] The former essentially suggests immediate dissociation upon impact with the surface. The latter alludes to the notion of equilibration with the surface in a temporary intermediate (molecular) state which serves as a precursor to dissociation. Detailed studies of prototypical diatomics have especially served to establish general trends for sticking curves, i.e., certain signatures are seen to indicate one or the other adsorption mechanism.[5] A dependence of sticking data on substrate temperature is for instance believed to reflect precursor-mediated adsorption, considering the kinetic competition between dissociation and desorption from such a precursor state.

Such trends have met an overall intriguing consistency over a range of studied systems. Notwithstanding, one needs to recognize that a bulk of corresponding work has been done for (dissociative) H_2 adsorption, where a clearcut distinction might be facilitated by the relatively "smooth" molecule-surface interaction. Upon presence of π-orbital involving molecular bonds, the corresponding potential energy surface (PES) becomes significantly more intricate, which could prohibit such a direct extraction of mechanistic insight into measured sticking data. A characteristic example for this is the adsorption of N_2 on W(110), where measured sticking curves eluded a simple interpretation on the basis of the aforementioned experimental trends.[5] In fact, seemingly contradictory evidence from molecular beam measurements could only be reconciled through explicit dynamical simulations, which revealed a complex interplay between the direct and indirect adsorption mechanisms depending on initial conditions.[6] The contribu-

a)Electronic mail: vanessa.bukas@ch.tum.de

tion of these processes was shown to arise from characteristics of the gas-surface interaction far from the surface and could only be captured within an accurate high-dimensional description of the PES involving all molecular degrees of freedom.

Similar complexities can be expected for the adsorption of O_2, a key process in oxidation catalysis. In fact, the typically large exothermocity of this process on transition metal surfaces adds yet another facet, namely, the question of energy dissipation. Considering its influence, e.g., on the aforementioned kinetic competition of dissociation or desorption from a precursor state, the question is how much this affects measured sticking curves and the established trends in terms of fingerprints. From a modeling perspective, it again adds the question of how well the dissipative dynamics needs to be accounted for. The latter is particularly relevant, as a fully quantitative account of phononic energy dissipation in explicit *ab initio* molecular dynamics (MD) simulations is still highly demanding, when aiming for sufficient statistical averaging and the full computation of energy-dependent sticking curves.[7,8] Highly appealing is therefore more effective treatments of surface mobility.[9–13] The potential sensitivity of O_2 sticking curves to the details of energy dissipation then makes a comparison to high-quality experimental data particularly valuable to gauge the accuracy of such effective approaches or vice versa the level of detail required to account for.

With this motivation, we focus in the present work on the adsorption of O_2 on clean Pd(100). Recent molecular beam experiments found the initial sticking probability $S_0(E_i, T_s)$ for this system to be independent of substrate temperature T_s and only weakly increasing with incident kinetic energy E_i.[14] In terms of the classical trends, this suggested an interpretation in the form of a predominantly direct dissociation mechanism with, at most, some reaction paths that include a modest activation barrier. At low E_i and T_s, however, the contribution from a partly equilibrated molecular-precursor was conjectured in order to rationalize the independence on surface coverage and deviation from normal energy scaling under those conditions.[14] We scrutinize this interpretation through dynamical simulations on a first-principles six-dimensional (6D) PES that accounts for all molecular degrees of freedom and which we suitably augment with effective treatments of surface mobility. Accounting in some respects for the latter is found to substantially change the calculated sticking curve $S_0(E_i, T_s)$, i.e., the latter is indeed sensitive to energy dissipation. Intriguingly, this holds for both direct and indirect adsorption mechanisms, either of which we obtain as dominant when basing the simulations on PESs obtained with two different density-functional theory (DFT) functionals. The uncertainties introduced by current semi-local DFT functionals thus prohibit a clear identification of the dominant adsorption mechanism. They also do not allow to fully disentangle whether the approximate treatment of substrate mobility or the deficiencies in the underlying DFT energetics are the primary reason for remaining small differences to the experimental data. All these intricacies nevertheless point already at this stage at the limitations of trying to directly deduce insight into the character of the adsorption process from measured sticking curves alone.

II. METHODS

The O_2-Pd(100) interaction energetics are obtained by spin-polarized DFT calculations, using either the exchange correlation functional due to Perdew, Burke, and Ernzerhof (PBE)[15,16] or due to Hammer, Hansen and Nørskov (RPBE)[17] to approximately assess the uncertainties introduced by prevalent semi-local functionals (see below). Electronic states are described with a plane wave basis set using a cutoff energy of 400 eV as implemented in the `CASTEP` code,[18] together with ultrasoft pseudopotentials (USPPs)[19] as bundled in the Materials Studio 6.0 database. These USPPs have been obtained with Vanderbilt's original generator[19] using the PBE functional. By comparing to a few converged all-electron calculations based on the FHI-aims code,[20] we have verified that the pseudopotential-induced error[21,22] in the O_2-Pd(100) interaction energies is not larger than 100 meV.[23] Within a periodic supercell model, the surface is represented by five-layer slabs which are separated by a vacuum distance of 15 Å and which are (3×3) multiples of the primitive surface unit cell of Pd(100). Calculations are performed using a $(4 \times 4 \times 1)$ Monkhorst-Pack grid[24] for k-point sampling.

More than 6000 DFT energies are calculated for various high- and low-symmetry configurations of the oxygen molecule above the frozen Pd(100) surface. These provide the basis for constructing a continuous representation of the adiabatic PES within all six molecular degrees of freedom (V_{6D}) for each of the two DFT functionals based on symmetry-adapted neural networks as pioneered by Behler and Reuter[25] for fcc(111) surfaces. Details about the present implementation can be found in Refs. 23, 26, and 27, including an adaption for fcc(100) surfaces in particular. We note that the resulting DFT-PBE PES has already been employed previously in Refs. 8, 23, and 28. Exactly the same recipe is followed here to obtain the continuous PES within the RPBE functional. See the supplementary material[29] for more details about the quality of both NN PES representations. Minima and barrier searches on these PESs have been conducted with a stochastic sampling method described in earlier work[27] and with the Nudged Elastic Band (NEB) method as implemented within the `Atomic Simulation Environment` (ASE),[30] respectively.

Classical MD simulations are performed on the resulting numerically efficient continuous PES representations. The effect of including the initial zero point energy of the O_2 molecule within a quasi-classical treatment was additionally investigated but found to have a negligible effect on the resulting dynamics. Focusing only on the molecular degrees of freedom, such simulations do not allow for phononic energy dissipation and will henceforth be denoted with frozen surface (FS). A first account of surface mobility can be incorporated on the level of the 3D surface oscillator (SO) model.[9] Here, the surface is mimicked by an oscillator which is assigned the mass (m_{SO}) of a single Pd atom and is permitted to move as a whole in all three directions within a harmonic potential. The associated (3×3) frequency matrix $\hat{\omega}_{SO}$ is assumed to be diagonal with values corresponding to a well localized surface mode of the Pd surface:[8,23] $\hbar\omega_{SO_{xx}} = \hbar\omega_{SO_{yy}} = 16$ meV and $\hbar\omega_{SO_{zz}} = 11$ meV. The O_2-phonon coupling is then described by a 3D-space rigid

shift $\mathbf{R}_{SO} = (X_{SO}, Y_{SO}, Z_{SO})$ of V_{6D}, and the MD equations of motion in this approximation are given by

$$\frac{\partial^2 \mathbf{R}_{A,B}}{\partial t^2} = -\frac{1}{m_{A,B}} \nabla_{\mathbf{R}_{A,B}} V_{6D}(\mathbf{R}_A - \mathbf{R}_{SO}; \mathbf{R}_B - \mathbf{R}_{SO}), \quad (1a)$$

$$\frac{\partial^2 \mathbf{R}_{SO}}{\partial t^2} = -\frac{1}{m_{SO}} \nabla_{\mathbf{R}_{SO}} V_{6D}(\mathbf{R}_A - \mathbf{R}_{SO}; \mathbf{R}_B - \mathbf{R}_{SO}) - \hat{\omega}_{SO}^2 \cdot \mathbf{R}_{SO}, \quad (1b)$$

where $m_{A/B}$ and $\mathbf{R}_{A/B}$ are the masses and Cartesian coordinates of the two individual oxygen atoms A and B.

The effect of a bulk thermal bath is approximately included within the generalized Langevin oscillator (GLO) approach.[10–12] Here, the SO is coupled to a further 3D so-called ghost oscillator of equal mass, $m_{GLO} = m_{SO}$, and frequency matrix $\hat{\omega}_{GLO} = \hat{\omega}_{SO}$. The same frequencies are also used to describe the SO-GLO coupling through a (3×3) coupling matrix $\hat{\Lambda}_{SO-GLO} = \hat{\omega}_{SO}$. The ghost oscillator is subject to frictional and random forces in order to account for energy dissipation and thermal fluctuations, respectively. As originally proposed by Adelman and Doll,[10] the former are described through an isotropic and diagonal damping matrix $\hat{\gamma}_{GLO} = \gamma_{GLO}\hat{\mathbf{I}} = \pi\omega_D/6\,\hat{\mathbf{I}}$, where ω_D is the Pd bulk Debye frequency.[23,31] Finally, the random force is a Gaussian white noise source W with a variance of $(2k_B T_s \gamma_{GLO}/m_{GLO}\Delta t)^{1/2}$, where k_B is the Boltzmann constant and Δt is the MD time integration step. The resulting equations of motion within the GLO model are thereby as follows:

$$\frac{\partial^2 \mathbf{R}_{A,B}}{\partial t^2} = -\frac{1}{m_{A,B}} \nabla_{\mathbf{R}_{A,B}} V_{6D}(\mathbf{R}_A - \mathbf{R}_{SO}; \mathbf{R}_B - \mathbf{R}_{SO}), \quad (2a)$$

$$\frac{\partial^2 \mathbf{R}_{SO}}{\partial t^2} = -\frac{1}{m_{SO}} \nabla_{\mathbf{R}_{SO}} V_{6D}(\mathbf{R}_A - \mathbf{R}_{SO}; \mathbf{R}_B - \mathbf{R}_{SO}) - \hat{\omega}_{SO}^2 \cdot \mathbf{R}_{SO} + \hat{\Lambda}_{SO-GLO} \cdot \mathbf{R}_{GLO}, \quad (2b)$$

$$\frac{\partial^2 \mathbf{R}_{GLO}}{\partial t^2} = -\hat{\omega}_{GLO}^2 \cdot \mathbf{R}_{GLO} + \hat{\Lambda}_{SO-GLO} \cdot \mathbf{R}_{SO} - \hat{\gamma}_{GLO} \frac{\partial \mathbf{R}_{GLO}}{\partial t} + W(\Delta t). \quad (2c)$$

We note that this GLO implementation and specific choice of parameters follow that of earlier works regarding H_2 adsorbing on or scattered from the Pd(111) and Pd(110) surfaces.[32–34] We nevertheless systematically tested the dependence on the specific parameter values by varying the oscillation frequencies entering $\hat{\omega}_{SO}$, $\hat{\omega}_{GLO}$, and $\hat{\Lambda}_{SO-GLO}$ by one order of magnitude, by varying the damping coefficient γ_{GLO} by two orders of magnitude, as well as by doubling the mass m_{SO}. This had little effect on the simulation results as will be further specified below.

The initial sticking coefficient at normal O_2 incidence was determined from classical MD trajectories with the O_2 molecule initially with its center of mass at a distance $Z = 9$ Å from the surface, where the PES value for oxygen at its equilibrium bond length $d_{eq} = 1.24$ Å is zero in both the DFT-PBE and DFT-RPBE PES representations. The initial molecular orientation and lateral center of mass position were sampled using a conventional Monte Carlo procedure. All statistical quantities are obtained by averaging over 5000 trajectories for each value of incidence energy E_i and substrate temperature T_s. Individual trajectories were integrated up to 10 ps in order to reach the following classification in terms of molecular adsorption, dissociative adsorption, or reflection: A trajectory was classified as dissociative whenever the O_2 internuclear distance d reached twice its equilibrium value ($d \geq 2d_{eq}$) and is further increasing at this time ($\dot{d} > 0$), while reflection was concluded when the molecular center reached its initial starting distance above the surface with a positive Z-velocity. All trajectories where neither dissociation nor reflection occurred up to the 10 ps integration time were classified as trapped.

III. RESULTS AND DISCUSSION

A. Experimental sticking versus dynamics within the frozen surface approximation

Figure 1 shows the initial sticking probability $S_0(E_i, T_s)$ at normal incidence as recently measured by molecular beam experiments.[14] Sticking is generally high (≥70%) within the entire range of investigated incidence energies and largely identical at the two substrate temperatures investigated, 100 K and 400 K. The overall weak increase with incidence energy and independence of substrate temperature was interpreted to reflect predominantly direct dissociative adsorption.[14] From additional data taken at finite coverages and oblique angles of incidence, some contribution from a partly equilibrated molecular-precursor was nevertheless speculated at low (E_i, T_s).

Even without explicit dynamical simulations, the overall high reactivity can already be gleaned directly from the calculated O_2-Pd(100) interaction potential. From a global search on the continuous 6D DFT-PBE PES representation,[27] we identify as most stable molecular adsorption state a configuration in which the O_2 molecule centers side-on above the Pd(100) hollow site with its molecular axis oriented along the [001] direction, i.e., in the direction of the neighboring hollow sites. This molecular well can be reached along a barrierless entrance channel as visible in the 2D (elbow) cut through the PES shown in Fig. 2. The calculated minimum energy path to dissociation also included in Fig. 2 exhibits a dissociation barrier out of this

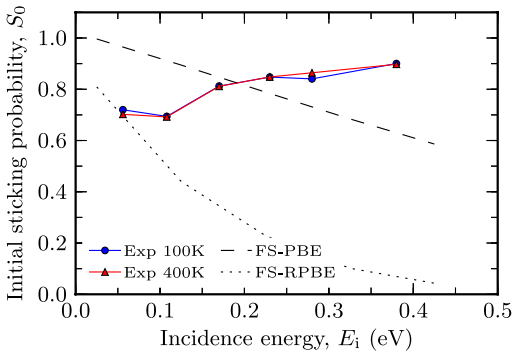

FIG. 1. Initial sticking probability $S_0(E_i, T_s)$ of O_2 on Pd(100) as a function of incidence energy E_i and at normal angle of incidence. Experimental data for two substrate temperatures, $T_s = 100$ K (solid blue line) and 400 K (solid red line), are reproduced from Ref. 14. Theoretical sticking probabilities are calculated in the temperature-independent frozen-surface (FS) approximation, using either DFT-PBE (dashed black line) or DFT-PRBE (dotted black line) energetics.

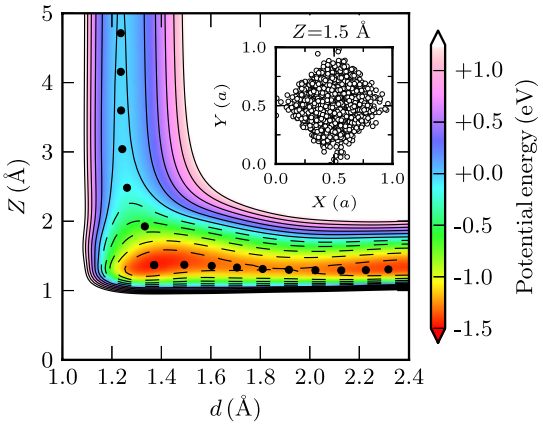

FIG. 2. Contour plot of a 2D cut through the 6D O_2/Pd(100) DFT-PBE PES depicting the existence of a pronounced molecular chemisorption well. Shown is the energy profile as a function of the vertical distance of the O_2 center of mass Z and the O_2 bond length d for a O_2 molecule in a side-on configuration with the molecular axis oriented along the [001] direction. Additionally shown by black markers is the minimum energy path towards dissociation as obtained from a NEB calculation. Black contour lines indicate 250 meV energy increments. Inset: Lateral O_2 center of mass positions (X,Y) over the surface unit-cell for the ultimately dissociating trajectories as molecules with $E_i = 25$ meV first reach a surface distance of $Z = 1.5$ Å (see text).

well of E_{diss} = 200 meV. This is a small value compared to the actual depth of the molecular well of $E_b = -1.45$ eV with respect to the gas phase. Even if a fraction of this energy gained upon adsorption is quickly transferred to internal molecular degrees of freedom, such a small barrier should thus be readily surmounted. Based on highly consistent DFT-PBE energetics ($E_b = -1.52$ eV, $E_{diss} = 120$ meV), this was the conclusion taken by Liu and Evans, who correspondingly classified the dissociative adsorption process as essentially non-activated.[35] The overall high reactivity measured in the experiment seems to support this assignment, as well as the general notion to assume an approximately unity sticking coefficient in coarse-grained microkinetic simulations whenever static total energy calculations identify a barrierless entrance channel to adsorption.[2,36–38]

Aiming to scrutinize such mechanistic assignments made on the basis of the static PES alone, we proceed with the classical trajectory calculations. Evaluating the fraction of reflected and adsorbing trajectories yields the theoretical sticking coefficient at a given incidence energy. Within the frozen-surface approximation, i.e., restriction to the 6D PES, the resulting sticking curve $S_0(E_i)$ is necessarily independent of substrate temperature and is compared to the experimental sticking curves in Fig. 1. Confirming the expectations from the attractive DFT-PBE PES, the theoretical sticking is rather high at low E_i and therewith in the same ballpark as the experimental data. For these low incidence energies, there is thus no qualitative disagreement with experiment at the level of semi-local DFT as, e.g., in case of the enigmatic O_2 at Al(111) system.[39,40] This is not too surprising considering that a major break-down of the electronic adiabaticity of the adsorption process had been invoked as one possible reason behind the O_2/Al(111) discrepancy.[39,41] This unlikely applies to Pd(100), which exhibits a very high electronic density-of-states at the Fermi level and for which only small energy losses to electron-hole pairs during O_2 adsorption have been calculated.[28]

In terms of overall (rough) magnitude, the favorable agreement of experimental and theoretical sticking extends over the entire range of incidence energies shown in Fig. 1. Nevertheless, there is a disturbing difference in trend with E_i. In contrast to the measured slight rise of sticking with E_i, the calculated FS sticking curve shows a continuous decline. This decline is in fact even more pronounced when calculating the sticking curve on the basis of the DFT-RPBE PES, cf. Fig. 1. Repeating the above static analysis also for this PES, we find its topology to be qualitatively very similar to that of the DFT-PBE PES. Important quantitative differences are therefore nicely summarized in terms of the two dynamically relevant quantities, E_b and E_{diss}. In line with the general construction idea of the RPBE functional,[17] the molecular well is much more shallow in the DFT-RPBE PES ($E_b = -0.85$ eV), while reflecting the concomitant weaker bond activation, the dissociation barrier is with E_{diss} = 400 meV about twice as high as at the DFT-PBE level. Even though the ratio of these two quantities is thus much less favorable, on purely energetic grounds, dissociative adsorption would nevertheless still be classified as non-activated even at the DFT-RPBE level, i.e., the molecules gain much more energy upon adsorption than is needed to overcome the dissociation barrier.

The decline of the sticking curve with E_i obtained with both functionals is thus a purely dynamical effect. Aiming to extract its origin, we analyze the trajectories in more detail. First of all, this trajectory analysis largely confirms the dynamical relevance of the minimum energy path depicted in Fig. 2. Independent of the incidence energy and for both functionals (as well as all later surface mobility treatments), essentially all trajectories leading to adsorption show the molecules accumulating first around the hollow molecular chemisorption well. This preference for adsorption above hollow is exemplified in the inset of Fig. 2 which analyzes the lateral O_2 center of mass positions over the surface unit-cell for the ultimately dissociating dynamical trajectories as the molecules first reach a surface distance of Z = 1.5 Å. The data shown correspond to E_i = 25 meV and the PBE functional, with equivalent findings obtained at all other incidence energies and for DFT-RPBE.

After arrival at the molecular chemisorption state, the fate of the molecules is almost instantaneously decided at low E_i at the DFT-PBE level. This is demonstrated by the time distribution shown in Fig. 3(a), which indicates after which time a trajectory has been classified as dissociated, reflected, or trapped. Recall that trapping is assigned to all molecules that have neither dissociated nor reflected after 10 ps simulation time, which is why the corresponding fraction is shown at this time bin in Fig. 3. As apparent from Fig. 3(a), essentially all trajectories dissociate in a rather direct fashion, i.e., within several picoseconds and thus after a minimal number of surface rebounds (typically <5). This is completely different at the DFT-RPBE level, where almost all trajectories instead end up being trapped, cf. Fig. 3(b). The different reactivities of the two DFT PESs (E_b and E_{diss}) thus do have a significant effect in terms of entirely changing the dominant adsorption mechanism from direct (DFT-PBE) to indirect (DFT-RPBE).

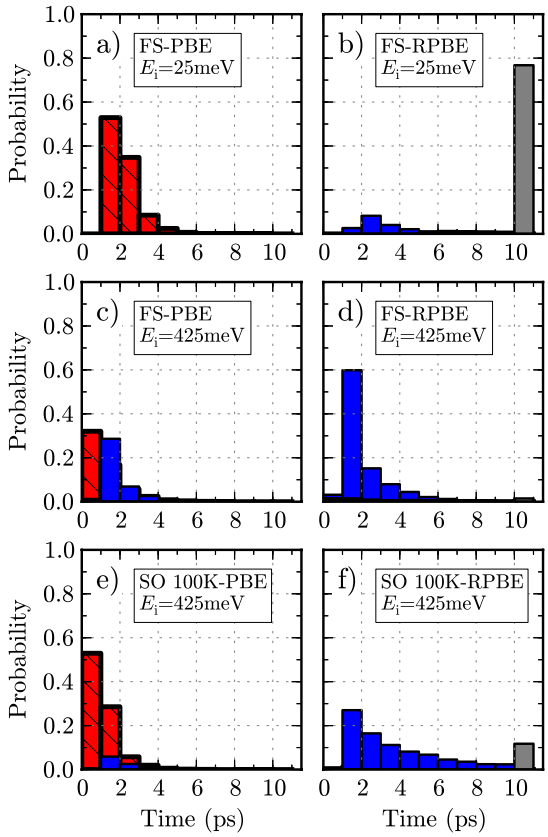

FIG. 3. Time distribution characterizing events of reflection (blue), direct dissociation (shaded red), and molecular trapping (gray) as classified within the performed MD simulations. Trapping is assigned if neither dissociation nor reflection has occurred after 10 ps simulation time, which is why the corresponding fraction is shown at this time bin. Left and right panels refer to trajectories calculated on the basis of the DFT-PBE and DFT-RPBE PES descriptions, respectively, while the employed level of theory and initial conditions (E_i and T_s) are as reported in the corresponding panel labels. We note that summing up the red and gray bars yields the initial sticking probabilities S_0 of the respective functional at the particular incidence energies E_i and surface temperatures T_s shown in Figs. 1 and 4.

At low incidence energies, this does not show up in the sticking coefficient though, as already a small amount of energy transfer to internal vibrational, rotational, or lateral translational degrees of freedom is sufficient to prevent immediate desorption, and since, molecules correspondingly trapped in the surface potential are being counted as contributing towards sticking. We note that in the absence of any other dissipation mechanism within the FS approximation, such trapped molecules would in fact eventually be able to desorb. Notwithstanding, the time scale for a corresponding transfer of energy back into the perpendicular translational motion would be rather long. In reality, other dissipation channels would have set in during this time, which is why it is reasonable to count these trajectories as contributing to the sticking coefficient. Also, the rather arbitrarily set maximum integration time of 10 ps should in this respect not matter, as we have verified by applying the trapping classification already after 8 ps.

While the PES differences thus do not show up at low E_i, they do increasingly at larger incidence energies. Corresponding fast molecules are less efficiently steered to direct dissociation. Neither is the energy transfer to internal degrees of freedom efficient enough anymore to quickly remove the large excess kinetic energy and trap them in the surface potential. As shown in Figs. 3(c) and 3(d) for the largest E_i = 425 meV, we thus find for both PES descriptions a large number of molecules that are reflected very quickly from the surface. Without efficient trapping, only the decreasing fraction of molecules that already starts from configurations favorable for a more or less direct dissociation mechanism can contribute to the decreasing sticking seen in Fig. 1. Such a mechanism is generally disfavored by a smaller acceleration into a more shallow adsorption well and a higher barrier to surmount, which is why the concomitant decline of $S_0(E_i)$ with E_i is also much more pronounced at the DFT-RPBE level.

From a bulk of work on O_2 adsorption on late transition metals,[41] the PBE and RPBE functionals can be seen as popular representatives for opposite ends within the range of current gradient-corrected functionals, with the prior likely more on the overbinding side and the latter possibly slightly underbinding. Within the understanding of the just presented dynamical analysis, concomitant uncertainties in the energetic description of the molecular chemisorption well (E_b and E_{diss}) at the semi-local DFT level are nevertheless unlikely to cause the wrong trend of the sticking curve with E_i as compared to the experimental data. Rather than the overall attractiveness of the PES, the major reason for the decline of the calculated sticking curves lies in an insufficient ability to trap the molecules in the chemisorption well. This thus points more to a weakness of the FS approximation, in which such a trapping can only result from energy transfer into molecular rovibrational degrees of freedom. In reality, this can also come from inelastic collisions with the surface atoms, which suggests the necessity to include some degree of surface mobility into the modeling.

B. Surface mobility on the level of SO and GLO models

We introduce a first account of energy exchange with the lattice through the SO model and show the derived initial O_2/Pd(100) sticking probabilities for substrate temperatures of T_s = 100 K and 400 K in Fig. 4. On the basis of the DFT-PBE energetics, and compared to the equivalent description within the FS approximation, we indeed observe the qualitative change expected from our preceding dynamical analysis, namely, a considerable increase in high-energy sticking (up to as much as 25% for E_i = 425 meV). This almost completely lifts the decline with E_i seen at the FS level. With the SO model now generally allowing for temperature dependence, the resulting essentially constant $S_0(E_i, T_s)$ is nevertheless only weakly dependent on T_s and thus in seemingly good agreement with experiment.

The mechanistic analysis of the PBE-based adsorptive trajectories reveals the relevance of the same reaction pathway above hollow as found in the FS dynamics and depicted in Fig. 2. Additionally, the short reaction/reflection times analyzed in Fig. 3(e) once again suggest that the fate of impinging molecules is almost instantaneously determined and direct dissociation takes place essentially upon first impact

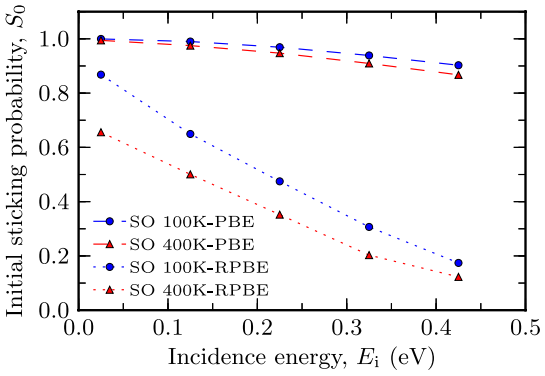

FIG. 4. Comparison of the initial sticking probability $S_0(E_i, T_s)$ of O_2 on Pd(100) as calculated within the surface oscillator model (SO) for normal angle of incidence and varying incidence energy E_i. Data are shown for substrate temperatures of $T_s = 100$ K (blue circles) and 400 K (red triangles), using either DFT-PBE (dashed lines) or DFT-PRBE (dotted lines) energetics.

with the surface. The differences in reactivity compared to the FS case do therefore not originate from the activation of different reaction pathways or adsorption mechanisms. We instead rationalize the increased SO sticking at high E_i with the improved efficiency of direct dissociation above hollow due to an enhanced steering of impinging fast molecules in the now "elastic" surface potential. The energy transfer to the surface possible within the SO model simply dampens the perpendicular translational motion of highly accelerated O_2 already upon first impact. This increases the probability that they will be effectively captured by the attractive potential and subsequently led to dissociation. This picture arises from the analysis of the significant amount of trajectories that start from the exact same initial conditions and yet are reflected within the FS but dissociated within the SO model. The corresponding energy profiles reveal the simultaneous onset of the O_2-Pd(100) interaction and the SO kinetic energy, and therewith underline the decisive role of the SO energy uptake in ultimately determining the trajectory outcome.

Quantifying this SO energy uptake in fact reveals that considerable amounts of energy are transferred back and forth between the O_2 molecule and the SO even on the short time scales until dissociation. At the moment when the trajectories fulfill the dissociation criterion, an average of 350 meV (considering the sum of kinetic and potential energies of the oscillator) is stored in the SO for $T_s = 100$ K and a low incidence energy of 25 meV. For the fast molecules with $E_i = 425$ meV, this value even increases up to 510 meV. In the absence of any further dissipation channel, the SO is thus severely overheated. As a result, one may expect that the promotion of direct dissociation over "proper" molecular trapping is to some degree artificial and that the agreement with the experimental sticking curve on the DFT-PBE SO level is thereby merely fortuitous.

This view is indeed supported by the results obtained with the DFT-RPBE PES, where, as already indicated, dissociation is generally less favored due to the limited accessibility of the corresponding transition state. Here, the partial damping on account of the surface mobility also succeeds in trapping the molecules, but only for a slightly extended period of time compared to the FS situation. This is visible from the extended reflection time distribution in Fig. 3(f) compared to Fig. 3(d). The ongoing strong energy exchange between trapped molecules and hot SO thus promotes in this case rather a delayed reflection than (equally artificially) facilitating dissociation. The resulting sticking curve at the DFT-RPBE SO level shown in Fig. 4 correspondingly still exhibits the strong decline with incidence energy.

Suspecting the lack of further energy dissipation channels as a major limitation in the present application of the SO model, we proceed with classical trajectory calculations that now include a coupling to a bulk thermal bath within the GLO approach. At first glance, application of the GLO model on the basis of the DFT-PBE PES has an almost inconsequential effect on sticking as compared to the results obtained within the SO approximation. Figure 5 now shows an entirely constant unity sticking coefficient independent of both E_i and T_s. Analysis of the underlying GLO trajectories nevertheless reveals again substantial changes that are fully consistent with the expectations from the SO analysis. Also at the DFT-PBE level, there is now a contribution of molecular trapping to the total sticking, i.e., the GLO succeeds at least to some extent in removing the artificially enhanced direct dissociation seen at the SO level. The average amount of energy stored in the SO itself at the moment when trajectories fulfill the dissociation criterion is now reduced to 210 meV (260 meV) at $E_i = 25$ meV (425 meV) and $T_s = 100$ K, as compared to the 350 meV (510 meV) found before within the SO model. Owing to the non-equilibrium nature of O_2 dissociation on Pd(100),[23] this is still far away from the thermal equilibrium value of a surface atom $2 \times \frac{3}{2} k_B T_s \approx 25$ meV even within the limitations of the GLO model, but still suggests more efficient surface equilibration. The latter is also reflected in the dependence of the trapping contribution to the overall sticking on the (E_i, T_s) conditions summarized in Fig. 6. As expected for a (largely) equilibrated molecular precursor, this contribution depends only weakly on the initial incidence energy, but instead sensitively on the substrate temperature. As also shown in Fig. 6, the varying excess kinetic energy of molecules

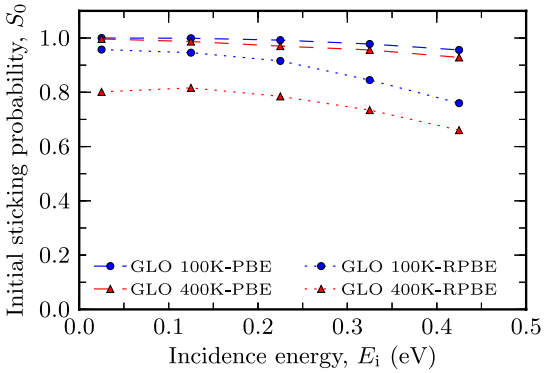

FIG. 5. Comparison of the initial sticking probability $S_0(E_i, T_s)$ of O_2 on Pd(100) as calculated within the generalized Langevin oscillator model (GLO) for normal angle of incidence and varying incidence energy E_i. Data are shown for substrate temperatures of $T_s = 100$ K (blue circles) and 400 K (red triangles), using either DFT-PBE (dashed lines) or DFT-PRBE (dotted lines) energetics.

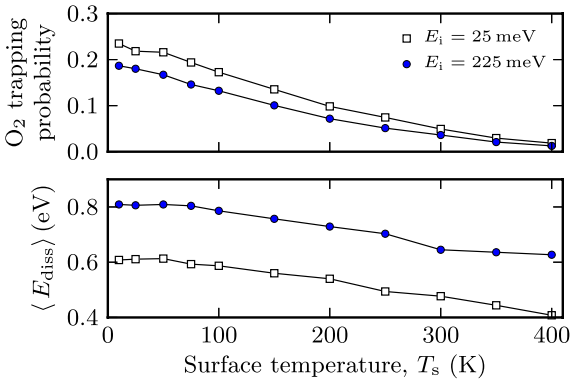

FIG. 6. Top panel: Temperature dependence of the probability of molecular trapping within the GLO model and using the DFT-PBE energetics. Bottom panel: Average amount of energy dissipated into the GLO heat bath for the corresponding trapped trajectories. Data are shown for incident energies of $E_i = 25$ (open squares) and 225 meV (closed circles).

with different E_i is thus successfully drained into the heat bath, i.e., the average energy dissipated into the bath is for every substrate temperature precisely by 200 meV higher for molecules impinging with E_i = 225 meV as compared to those impinging with E_i = 25 meV.

On the basis of the DFT-RPBE energetics, molecular trapping remains the only adsorption mechanism also at the GLO level. Allowing for "dissipated" energy to leave the SO into the heat bath, however, now suppresses the artificial possibility that some fraction of this energy is returned to the adsorbate and thereby induces desorption. This removes the delayed reflection times observed within the equivalent SO results, cf. Fig. 3(f), and yields a largely increased sticking coefficient at high incidence energies. The resulting DFT-RPBE GLO sticking curves shown in Fig. 5 exhibit only a weak decline with E_i. They also exhibit only a weak dependence on substrate temperature. This is rather intriguing in view of the predominance of the precursor mechanism, which is generally believed to be fingerprint in the form of a sensitive substrate temperature dependence. Overall, the DFT-RPBE GLO curve agrees therewith now rather well with the experimental data, at least similarly well as the DFT-PBE GLO sticking curve, cf. Fig. 5.

This is, in fact, a rather intriguing, if not disturbing result. At the GLO level, both DFT-PBE and DFT-RPBE descriptions yield rather similar sticking curves, and this despite predicting completely different adsorption mechanisms: Predominantly, direct dissociation with a small contribution of molecular trapping at low substrate temperatures within DFT-PBE versus completely indirect dissociation within DFT-RPBE. Compared to the experimental data, both functional levels reach indeed the same achievements and exhibit the same shortcomings. They correctly predict a near-unity sticking over the range of studied incidence energies with if at all only a weak dependence on substrate temperature. Yet, both fail to reproduce the measured slight increase in sticking with E_i, or more precisely they overestimate the experimental sticking at low E_i.

Dissipation seems to affect much more the high incidence energy part of the sticking curves. This view is also supported by the robustness of the obtained sticking results when varying the parameters entering the GLO model as described in Section II. All in all, these variations lead only to insignificant variations of $S_o(E_i, T_s)$ within a few percent. In turn, the uncertainties in the semi-local DFT description of the actual chemisorption well (E_b and E_{diss}) do critically affect the actual adsorption mechanism, yet again do not seem to propagate to the total sticking curve. In light of the dynamical analyses performed for the FS, SO, and GLO models, we suggest that a slightly incorrect description of the entrance channel part of the PES can be one reason for the remaining small discrepancy — within these effective treatments of dissipation. Presently, unaccounted small activation barriers in this channel for some molecular configurations are likely to specifically affect the total sticking at low incidence energies and could therewith constitute the "missing ingredient" to a fully quantitative agreement with experiment.

Unless there is a problem in the experimental data, the obvious and systematic limitation of these models is an equally likely cause: Reducing the phononic fine structure of the Pd surface into computationally convenient augmentations of the frozen-surface within the O_2-Pd(100) interaction cannot, by construction, account for the energy exchange with an entire layer of moving surface atoms. Only detailed future studies including all these degrees of freedom will allow to completely capture the influence of surface mobility on the calculated sticking curves.

IV. SUMMARY AND CONCLUSIONS

We presented a detailed calculation of the initial sticking coefficient of O_2 at Pd(100) based on classical trajectory calculations on first-principles 6D potential energy surfaces. The specific motivation was to elucidate the role of energy dissipation during the exothermic surface reaction by augmenting the 6D dynamics with various effective accounts of surface mobility, as well as to assess in how much classical trends in the sticking data reveal the underlying adsorption mechanism. To our knowledge for the first time, we observe that an account of energy dissipation leads to qualitative changes of the calculated sticking curve as compared to the prevalent frozen-surface approximation. Compared to the much more frequently studied adsorption of H_2 (also at Pd surfaces[32–34]), this might not come as altogether surprising in view of the much smaller mass mismatch of oxygen with palladium. It is, however, remarkable with respect to the rather similar N_2 on W(110) system[6] ($\frac{m_N}{m_W} \approx \frac{14}{184}$). Intermediate in its mass ratio compared to H_2/Pd ($\frac{m_H}{m_{Pd}} \approx \frac{1}{106}$) and O_2/Pd ($\frac{m_O}{m_{Pd}} \approx \frac{16}{106}$), it exhibits PES characteristics intriguingly similar to that of O_2/Pd(100), i.e., non-activated paths to dissociation alongside a precursor molecular well. Yet, the N_2/W(110) sticking curve showed no change when applying effective treatments beyond the frozen-surface approach.

The hierarchical application of FS, SO, and GLO models reveals how the calculated sticking curves sensitively respond to details of energy exchange with the substrate. Already some degree of energy exchange as provided by the SO model enhances the steering of highly accelerated impinging O_2, while "proper" molecular trapping necessitates an account of further

bulk dissipation channels as in the GLO. The large amount of energy released in the exothermic reaction otherwise simply leads to an overheating of the SO degree of freedom. Compared to the N_2/W(110) system, one important difference to note is the considerably deeper molecular well in the corresponding FS-PES description ($E_b = -0.39$ eV[42] and -0.85 eV, respectively, within DFT-RPBE) which leads to a significantly increased acceleration of impinging molecules and requires more than twice as much energy to be dissipated upon reaching the molecular state. The latter may also hint towards a different response of the real phonons — potentially mitigated by the different phononic properties of the bare surfaces alone. It might thus comprise a key discriminating characteristic, which could be further elucidated by more conceptually and computationally demanding studies including a more realistic phonon heat bath.[8]

For two different PES representations based on the DFT-PBE and DFT-RPBE functionals, we correspondingly obtain at the GLO level a rather satisfying agreement with experimental sticking data.[14] This in principle appealing robustness of the simulation results with respect to the uncertainties of semi-local DFT energetics does not extend to the level of the underlying adsorption mechanism though. The more attractive DFT-PBE energetics predicts a predominantly direct dissociation mechanism with some amount of molecular trapping at low substrate temperatures. The less attractive DFT-PRBE energetics instead predicts adsorption almost exclusively via the molecular precursor state.

Completely different adsorption mechanisms therewith lead to rather similar sticking curves that agree equally well with the experimental data. Independent of the small quantitative discrepancies that remain in either case with respect to experiment, this clearly demonstrates that an unambiguous deduction of the adsorption mechanism from the initial sticking data alone is not feasible for this system. Such fingerprinting may work for simpler adsorption systems with smoother potential energy surfaces. At the latest for reactions with high degree of exothermicity dedicated calculations explicitly accounting for high-dimensional potential energy surfaces including substrate mobility at best in the form of moving surface atoms are required to establish the mechanistic details. These details can still be very important not only in light of fundamental understanding but also for coarse-grained microkinetic models.[35,43]

ACKNOWLEDGMENTS

We thank H. F. Busnengo for providing his SO and GLO implementations as well as many stimulating discussions. Funding through the Deutsche Forschungsgemeinschaft is acknowledged within Project No. RE1509/19-1, as is generous access to CPU time through the Leibniz Rechenzentrum der Bayerischen Akademie der Wissenschaften (Project No. pr85wa).

[1]M. Morris, M. Bowker, and D. A. King, in *Simple Processes at the Gas-Solid Interface*, Comprehensive Chemical Kinetics Vol. 19, edited by C. H. Bamford, C. F. H. Tipper, and R. G. Compton (Elsevier, 1984), pp. 1–179.
[2]M. K. Sabbe, M.-F. Reyniers, and K. Reuter, Catal. Sci. Technol. **2**, 2010 (2012).
[3]L. Vattuone, G. Bracco, M. Smerieri, L. Savio, and M. Rocca, in *Dynamics of Gas-Surface Interactions*, Springer Series in Surface Sciences Vol. 50, edited by R. D. Muiño and H. F. Busnengo (Springer, 2013), pp. 1–23.
[4]P. D. Nolan, M. C. Wheeler, J. E. Davis, and C. B. Mullins, Acc. Chem. Res. **31**, 798 (1998).
[5]J. Davis and C. Mullins, Surf. Sci. **380**, L513 (1997).
[6]M. Alducin, R. Díez Muiño, H. F. Busnengo, and A. Salin, Phys. Rev. Lett. **97**, 056102 (2006).
[7]A. Gross, ChemPhysChem **11**, 1374 (2010).
[8]J. Meyer and K. Reuter, Angew. Chem., Int. Ed. **53**, 4721 (2014).
[9]M. Hand and J. Harris, J. Chem. Phys. **92**, 7610 (1990).
[10]S. A. Adelman and J. D. Doll, J. Chem. Phys. **64**, 2375 (1976).
[11]J. C. Tully, J. Chem. Phys. **73**, 6333 (1980).
[12]J. C. Polanyi and R. J. Wolf, J. Chem. Phys. **82**, 1555 (1985).
[13]A. Gross, "Ab initio molecular dynamics simulations of the O_2/Pt(1 1 1) interaction," Catal. Today (in press).
[14]A. den Dunnen, S. Wiegman, L. Jacobse, and L. B. F. Juurlink, J. Chem. Phys. **142**, 214708 (2015).
[15]J. P. Perdew, K. Burke, and M. Ernzerhof, Phys. Rev. Lett. **77**, 3865 (1996).
[16]J. P. Perdew, K. Burke, and M. Ernzerhof, Phys. Rev. Lett. **78**, 1396 (1997).
[17]B. Hammer, L. Hansen, and J. K. Nørskov, Phys. Rev. B **59**, 7413 (1999).
[18]S. J. Clark, M. D. Segall, C. J. Pickard, P. J. Hasnip, M. I. J. Probert, and M. C. Payne, Z. Kristallogr. **220**, 567 (2005).
[19]D. Vanderbilt, Phys. Rev. B **41**, 7892 (1990).
[20]V. Blum, R. Gehrke, F. Hanke, P. Havu, V. Havu, X. Ren, K. Reuter, and M. Scheffler, Comput. Phys. Commun. **180**, 2175 (2009).
[21]M. Fuchs, M. Bockstedte, E. Pehlke, and M. Scheffler, Phys. Rev. B **57**, 2134 (1998).
[22]A. Kiejna, G. Kresse, J. Rogal, A. D. Sarkar, K. Reuter, and M. Scheffler, Phys. Rev. B **73**, 035404 (2006).
[23]J. Meyer, "*Ab initio* modeling of energy dissipation during chemical reactions at transition metal surfaces," Ph.D. thesis, Freie Universität Berlin, Germany (2012).
[24]H. J. Monkhorst and J. D. Pack, Phys. Rev. B **13**, 5188 (1976).
[25]J. Behler, S. Lorenz, and K. Reuter, J. Chem. Phys. **127**, 014705 (2007).
[26]I. Goikoetxea, J. Beltrán, J. Meyer, M. Alducin, J. I. Juaristi, and K. Reuter, New J. Phys. **14**, 013050 (2012).
[27]V. J. Bukas, J. Meyer, M. Alducin, and K. Reuter, Z. Phys. Chem. **227**, 1523 (2013).
[28]J. Meyer and K. Reuter, New J. Phys. **13**, 085010 (2011).
[29]See supplementary material at http://dx.doi.org/10.1063/1.4926989 for details on the quality of the continuous PES representations obtained on the level of PBE and RPBE-DFT.
[30]S. R. Bahn and K. W. Jacobsen, Comput. Sci. Eng. **4**, 56 (2002).
[31]B. W. Veal and J. A. Rayne, Phys. Rev. **135**, A442 (1964).
[32]H. F. Busnengo, W. Dong, P. Sautet, and A. Salin, Phys. Rev. Lett. **87**, 127601 (2001).
[33]H. F. Busnengo, W. Dong, and A. Salin, Phys. Rev. Lett. **93**, 236103 (2004).
[34]H. F. Busnengo, M. A. Di Césare, W. Dong, and A. Salin, Phys. Rev. B **72**, 125411 (2005).
[35]D.-J. Liu and J. W. Evans, Phys. Rev. B **89**, 205406 (2014).
[36]K. Reuter and M. Scheffler, Phys. Rev. B **73**, 045433 (2006).
[37]J. Rogal, K. Reuter, and M. Scheffler, Phys. Rev. Lett. **98**, 046101 (2007).
[38]J. Rogal, K. Reuter, and M. Scheffler, Phys. Rev. B **77**, 155410 (2008).
[39]J. Behler, B. Delley, S. Lorenz, K. Reuter, and M. Scheffler, Phys. Rev. Lett. **94**, 036104 (2005).
[40]F. Libisch, C. Huang, P. Liao, M. Pavone, and E. A. Carter, Phys. Rev. Lett. **109**, 198303 (2012).
[41]C. Carbogno, A. Gross, J. Meyer, and K. Reuter, in *Dynamics of Gas-Surface Interactions*, Springer Series in Surface Sciences Vol. 50, edited by R. D. Muiño and H. F. Busnengo (Springer, 2013), pp. 389–419.
[42]G. A. Bocan, R. Díez Muiño, M. Alducin, H. F. Busnengo, and A. Salin, J. Chem. Phys. **128**, 154704 (2008).
[43]D.-J. Liu, A. Garcia, J. Wang, D. M. Ackerman, C.-J. Wang, and J. W. Evans, Chem. Rev. **115**, 5979 (2015).

Paper #3

Hot Adatom Diffusion Following Oxygen Dissociation on Pd(100) and Pd(111): A First-Principles Study of the Equilibration Dynamics of Exothermic Surface Reactions. V. J. Bukas and K. Reuter; Phys. Rev. Lett. **117**, 146101 (2016).

Hot Adatom Diffusion Following Oxygen Dissociation on Pd(100) and Pd(111): A First-Principles Study of the Equilibration Dynamics of Exothermic Surface Reactions

Vanessa J. Bukas* and Karsten Reuter
Chair for Theoretical Chemistry and Catalysis Research Center, Technische Universität München, Lichtenbergstraße 4, D-85747 Garching, Germany
(Received 30 March 2016; published 28 September 2016)

We augment *ab initio* molecular dynamics simulations with a quantitative account of phononic dissipation to study the hyperthermal adsorbate dynamics resulting from a noninstantaneous energy dissipation during exothermic surface chemical reactions. Comparing the hot adatom diffusion ensuing O_2 dissociation over Pd(100) and Pd(111) we find experimentally accessible product end distances to form a rather misleading measure for the lifetime of this hyperthermal state. The lifetime is particularly long at Pd(111) where a random-walk-type diffusion leads only to small net displacements. A detailed phonon analysis rationalizes the slow equilibration through long-lived Rayleigh mode excitations that spatially confine the released energy within a nanoscopic "hot spot" around the impingement region.

DOI: 10.1103/PhysRevLett.117.146101

There is a long-standing notion that exothermic surface reactions may result in products that are not instantaneously thermalized and thus exhibit a high transient mobility. The prospect of such species acting as "hot" precursors in subsequent reaction steps can strongly influence rates, e.g., in heterogeneous catalysis [1], while their excessive mobility has also been suggested to play a vital role in epitaxial growth mechanisms at low temperatures [2]. Concepts embracing such "hot reactions" have become increasingly established over the past decades [3], yet stimulate groundbreaking implications for prevalent assumptions still fundamentally relied upon in models of chemical kinetics [4]. Assuming instantaneous equilibration at a constant global temperature results, for example, in the Markovian state-to-state hopping that underlies all present-day microkinetic formulations in surface catalysis [5,6].

In the case of dissociative adsorption events, the actual adsorption and any subsequent diffusion of the dissociated products are thereby treated as decoupled, statistically unrelated thermal processes. This presumption is challenged by persistent experimental reports of hyperthermal diffusion or so-called "hot-adatom motion" ensuing the (exothermic) dissociative oxygen adsorption at metal surfaces [7–13]. Corresponding scanning tunneling microscopy studies rely on well-defined single crystal surfaces and controlled dosage in ultrahigh vacuum to produce highest quality data. Working at temperatures that are sufficiently low to suppress thermal diffusion, the transient motion is then inferred from recorded separation distances of adatom pairs in the low-coverage regime.

Even though not undisputed [14], the by far largest separations reported this way are more than 14 surface lattice constants (SLCs) in the case of dissociative O_2 adsorption at Al(111) [7]. While this may be rationalized with the exceptionally large exothermicity of this reaction, other factors like substrate symmetry must also play a role for the dissipation mechanism. Otherwise it is difficult to reconcile the 7–14 SLC separations found for O_2 at Ag(100) [11–13] with the small O-O separations peaking at two SLCs that have been recorded on more reactive Pt-group (111) transition metal surfaces [8,10].

Unable to explicitly access the picosecond dynamical motion, these experiments have unfortunately so far not allowed for any deeper mechanistic analysis or an extraction of the lifetime of the hyperthermal state. The recent development of the QM/Me (quantum mechanics/metal) embedding scheme instead offers this possibility from the perspective of predictive-quality first-principles simulations [15]. This scheme augments a density-functional theory (DFT) based quantum mechanical description of the immediate reaction zone with a quantitative treatment of phononic dissipation into an extended classical heat bath and thus allows to directly follow the dissipation dynamics through *ab initio* molecular dynamics (AIMD) simulations. In a first application to oxygen dissociation over Pd(100) QM/Me indeed predicted a nonimmediate energy transfer to the substrate with the resulting hot O adatoms traveling ballistically over four SLCs [15].

Here, we specifically analyze the role of substrate symmetry and compare this to O_2 dissociation over Pd(111), where previous experiments found hot-adatom motion leading only to shorter O-O separations around $\sqrt{3}$ or 2 times the surface lattice constant [10]. Fully reproducing these experimental end distances, our QM/Me-AIMD simulations intriguingly reveal a much slower equilibration on Pd(111); i.e., the O adatoms on Pd(111) remain hot for a much longer time than on Pd(100). The shorter end distances result instead from the (111) substrate symmetry, which only allows for a random-walk-type diffusion as compared to the directed motion along the

surface channels of the Pd(100) surface. A detailed phonon analysis furthermore relates the slower equilibration dynamics to the random-walk induced excitation of long-lived low-energy surface phonon modes that prevents an efficient dissipation of the reaction energy into the substrate bulk. Hitherto monitored O-O end distances are thus a rather misleading measure of the lifetime of the hyperthermal state.

The QM/Me embedding scheme effectively separates long-range elastic contributions due to displaced substrate atoms from the adsorbate-induced chemical interactions [15]. The latter are then sufficiently short ranged to be captured in periodic-boundary DFT supercell calculations, treating electronic exchange and correlation (xc) at the level of the semilocal Perdew-Burke-Ernzerhof (PBE) functional [16]. As shown in Fig. 1, these supercells contain three layer slabs with a (9×3) and (6×6) surface unit cell for Pd(100) and Pd(111), respectively. The long-range lattice deformation that occurs with the progressing chemical reaction as well as the concomitant phononic dissipation are in turn accounted for through a cubic bath of 125,000 Pd atoms described at the level of the modified embedded atom method (MEAM) [17]. This large bath size provides a quantitative description of the phononic band structure and ensures that phonon propagation has not yet reached the bath boundaries even for the longer AIMD trajectories (3 ps) considered in this work. The QM/Me-AIMD simulations are carried out within the Atomic Simulation Environment (ASE) [18] by loosely interfacing the `FHI-aims` all-electron DFT code [19] and the `LAMMPS` [20] implementation of the MEAM potential. At the employed computational settings, cf., Supplemental Material (SM) [21], and a time step of $\Delta t = 2.5$ fs, a high-quality molecular dynamics energy conservation within 0.5 meV per atom reflects a numerically well-defined Hamiltonian with negligible embedding-induced errors.

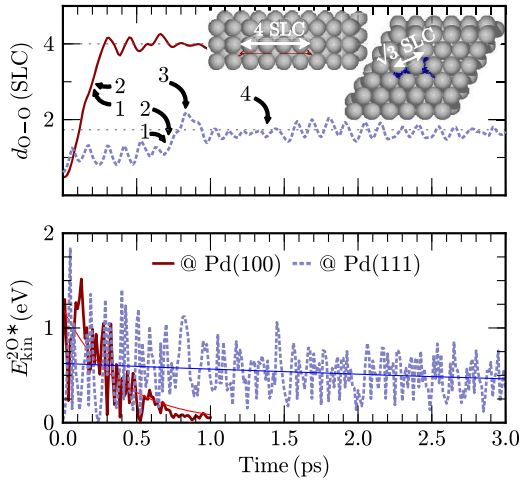

FIG. 1. Dynamical information extracted from QM/Me-AIMD trajectories for O_2 dissociating on Pd(100) (solid) and Pd(111) (dashed lines). Top panel: O-O separation distances in units of the surface lattice constant (SLC $\sim$ 2.79 Å). Hyperthermal adatom hops between neighboring hollow sites are numbered and schematically represented in a top view of the DFT-described reaction zones in the figure's insets (movies of the trajectories are available electronically in Ref. [21]). Lower panel: Oxygen kinetic energies E_{kin}^{2O*} demonstrating the picosecond time scale of energy transfer to the Pd(100) and Pd(111) phononic systems. Note the significantly different decay rates on the two surfaces as estimated from an exponential fit of the data (thin lines).

At Pd(100) a direct dissociation mechanism via one dominant entrance channel [26] provides suitable initial conditions of particular statistical relevance for the QM/Me-AIMD trajectory shown in Fig. 1. This channel steers the impinging O_2 molecule to dissociate side on and with its molecular axis centered above a fourfold hollow site [15]. To initialize trajectories in the precursor-mediated dissociation over Pd(111) [27] we focus instead on the relevant transition states (TS) between molecular and dissociative adsorption as identified via nudged elastic band (NEB) [28] calculations. The trajectory shown in Fig. 1 results specifically from the TS for the dissociation of a molecular precursor in the top-face-centered-cubic(FCC)-bridge configuration, i.e., with the O_2 center of mass essentially above a threefold FCC hollow site and the molecular axis oriented along the $[1\bar{2}1]$ direction. On both surfaces, the O_2 molecule is only given a negligibly small initial kinetic energy, so that both reactions are dominated by the large intrinsic exothermicity of the dissociation event.

Figure 1 illustrates the ensuing equilibration dynamics during both trajectories, where d_{O-O} directly measures the adatom separation distance as a function of time. The decay of the adsorbate kinetic energies presented in the lower panel shows both reactions to give rise to translationally hot products that are not instantaneously thermalized. The resulting transient mobility is marked by a series of hyperthermal diffusive hops between neighboring binding sites that occur on a ps time scale and are indicated by arrows in Fig. 1. Specifically, two such hops yield a largely increasing d_{O-O} on Pd(100) as the adatoms travel along the [001] surface channels and promptly equilibrate over hollow sites at four SLCs ($\sim$11.2 Å) apart. A random-walk-type diffusion is instead found on the densely packed Pd(111) surface that has the adatoms primarily trapped in the vicinity of hollow sites. Collisions with neighboring Pd atoms randomize the direction of the O lateral motion so that even the four barrier crossings counted along the presented 3 ps trajectory eventually lead only to the occupation of FCC adsorption sites at a much smaller distance of $\sqrt{3}$ times the SLC ($\sim$4.8 Å). Trajectories started at the dissociative TS above FCC or hexagonal-close-packed (HCP) hollow sites (not shown) lead to similarly short end distances (in the range of 1–3 SLCs) of which the most common is two times the SLC, exactly as seen in experiment [10].

The formation of hot adatoms on both surfaces does not come as altogether too surprising given the similarly high exothermicity of the dissociative reactions [2.3 vs 2.7 eV for O_2 on Pd(100) and Pd(111) at DFT-PBE level, respectively] and barriers for atomic diffusion (179 vs 327 meV). Difficult to reconcile on purely energetic grounds, however, is the markedly longer lifetime predicted for this hyperthermal phase on Pd(111). Even after 3 ps Fig. 1 reveals intriguingly hot adsorbates with fluctuations in kinetic energy on the order of 0.5 eV, i.e., an effective temperature amounting to several thousands of kelvin. Similarly long equilibration times are obtained in a total of nine other trajectories starting from the different TSs and slightly varying initial conditions. In all cases we observe a random-type walk with much longer absolute distances traveled than suggested by the small final equilibrium separation. Computed decay constants suggest an average of 10 ps to a full thermalization that is to be contrasted with the much shorter 1.2 ps obtained for the reaction at Pd(100), cf., Fig. 1.

These substantially different equilibration rates on the two surfaces arise from qualitative differences in the phononic response that already set in during the very early stages of the O_2 dissociation dynamics. We directly access this phononic information from the QM/Me-AIMD trajectories through the projection scheme originally laid out by McGaughey and Kaviany [29], yet appropriately extended here for the polyatomic primitive cell of a two-dimensional slab model [30]. In short, backfolding Γ-point phonons into the (original) larger primitive Brillouin zone defines mode-specific expansion coefficients that can in turn be used for evaluating the energy contained within a single harmonic phonon mode. Instantaneous application at any given AIMD time step can thus quantify phononic energy uptake "on the fly" without the need for averaging over time, while the underlying mode selectivity allows us to focus on certain groups of modes. In particular the surface phonons obviously form a very prominent group in this context and are classified here as modes whose displacement eigenvector is localized to at least 20% in the two outermost slab layers.

Figure 2(b) shows a corresponding phonon excitation spectrum calculated at $t = 75$ fs along the O_2/Pd(100) trajectory, i.e., when dissociation is right in progress with the O-O distance having reached about one SLC. Intriguingly, despite their negligible spectral weight illustrated by the also shown phononic DOS, surface modes have taken up more than a third of the total energy that has been dissipated into the substrate at that time. Quite in contrast to what is predominantly assumed about energy sinks in model bath Hamiltonians (cf., for example, Refs. [31–33] and references therein), it is thereby not the low-frequency Rayleigh modes that become dominantly excited, even though they lie energetically below the onset of the bulk part of the spectrum [30]. The energy

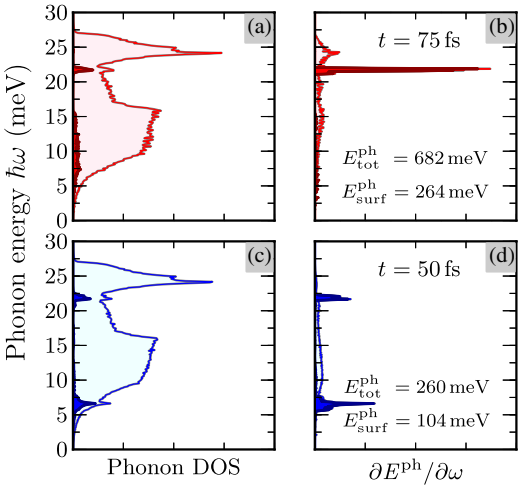

FIG. 2. Rightmost panels: Energy resolved phonon excitation spectra during the early stages of O_2 dissociation on Pd(100) (top) and Pd(111) (bottom). The total amount of phononic energy ($E^{\rm ph}_{\rm tot}$) along with the fraction assigned to surface modes ($E^{\rm ph}_{\rm surf}$) are noted. Leftmost panels: The corresponding Pd equilibrium DOS calculated for 40-layer slabs are shown for reference. In all cases the contribution of localized surface modes is indicated by thick blue/red lines.

is instead highly concentrated in a surface optical phonon band, which lies in a pseudogap of bulk modes at frequencies of 21–23 meV as shown in the SM. Analyzing the mode eigenvectors, this unexpected result can be rationalized by the preferred binding site of the O adatoms. Rather than indenting the topmost substrate layer upon impingement, which is the picture suggesting a predominant excitation of corresponding Rayleigh modes, the dissociating O atoms penetrate directly into the hollow sites and subsequently diffuse laterally over bridge sites along one of the [001] surface channels. Along this motion they rather push the top-layer Pd atoms laterally away, which corresponds exactly to the purely longitudinal displacement pattern of the modes belonging to the aforementioned surface optical phonon band.

Figure 2(d) reveals a rather different phonon excitation spectrum upon O_2 dissociation at the Pd(111) surface. Here, the random-walk-type diffusion mechanism rather leads to a weighted phonon population that essentially follows the surface DOS and has the larger fraction of the released chemical energy contained within low-frequency acoustic phonons. Behold some quantitative variations; this characteristic excitation of notoriously long-lived Rayleigh waves [34] at short wavelengths, cf., insets in Fig. 3, is consistently obtained for all QM/Me-AIMD trajectories starting from the different dissociative TSs. With their small group velocities, cf., SM, these modes efficiently confine the released energy within a small reaction zone around the impingement region. As reflected by the nonmonotonic behavior in the total phononic energy uptake, cf., SM, this

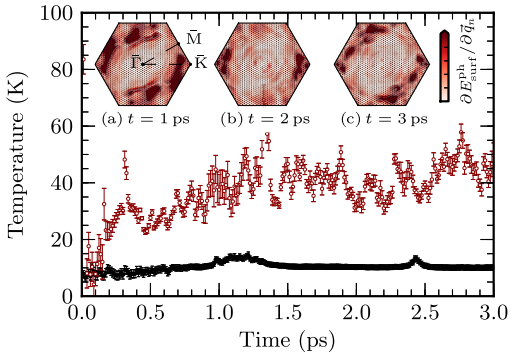

FIG. 3. Time-dependent temperature profiles for the Pd(111) surface hot spot (open) and bulk thermal bath (closed markers) as extracted from respective Planckian distributions at every QM/Me-AIMD time step (standard errors indicate the fit quality). Insets (a)–(c): Distribution of surface phonon energy (E^{ph}_{surf}) over the two-dimensional surface Brillouin zone at the noted times. The coloring is based on a linear interpolation between values at exact phonon wave vectors ($\vec{q}_n$, black markers) at which the energy of all phonon branches has been summed.

promotes a back and forth energy exchange between the O adatoms and the surface Pd atoms. In contrast, the (sub-ps) anharmonic decay of the highly populated surface optical modes at Pd(100) quickly dissipates the energy at a constant rate of ~2 meV/fs into the bulk at a concomitant much shorter lifetime of the hyperthermal state.

The situation at Pd(111) carries thus all characteristics of a phonon hot spot [35], in which the energy released into the phononic system stays confined in a nanoscopic region. After 3 ps we indeed find about one half of the system's total kinetic energy to still be within the confines of the DFT supercell, i.e., in the immediate reaction zone. Within this region phonon-phonon coupling quickly establishes a quasiequilibrium phonon distribution that is sufficiently well described by a Planckian distribution. This allows us to assign a local phonon temperature that we contrast in Fig. 3 to a similarly assigned phonon temperature of the Pd bulk modes. These results confirm a minimal coupling of the two subsystems over the entire course of the QM/Me-AIMD trajectory, with the surface hot spot eventually reaching an effective temperature that is five times larger than its bulk counterpart and still rising. The small extent of the hot spot leads thereby to an enormous effective energy density of the order of 2.7 eV/10 nm^3 ~ 10 J/cm^3 created by a singular molecular event. Even though modern high-fluency laser pulses reach even higher absorbed energy densities than this [36], much of this energy is there primarily deposited into electron-hole (*e-h*) pairs, which efficiently dissipate this energy over a larger volume. At present, our electronically adiabatic theory does not account for this dissipation channel at all. However, we do not expect this channel to be large. Using the calculated average velocity of all Pd atoms in the QM reaction zone over the course of the QM/Me-AIMD trajectory to evaluate the accumulated loss due to electronic friction [37], we arrive at a rough estimate of only 22 meV after 3 ps. This suggests that the "hot chemistry" ensuing the exothermic surface reaction is qualitatively different to laser-driven photochemistry, where particularly for chemisorbed adsorbates the excitation of hot electrons is generally believed to play a crucial role [41].

Similarities might instead be higher for radiation damage aspects like the transient recoil of nuclei under neutron bombardment. The presented QM/Me methodology is generally suitable for application to any problem that breaks a metal's translational symmetry in any number of periodic directions. Beyond its relevance within the surface science context (for instance to address adsorbate-induced reconstructions), it may therefore readily be employed to follow bulk diffusion or address the chemistry around bulk defects and dislocations [42].

In conclusion, we have studied the equilibration dynamics ensuing the exothermic O_2 dissociation at Pd(100) and Pd(111). The obtained *ab initio* molecular dynamics results indicate that hitherto considered product end distances provide a misleading measure of the transient hot adatom mobility that results from a noninstantaneous dissipation of the released energy. The lifetime of this hyperthermal state might be particularly long precisely in situations where the substrate symmetry or higher surface coverages enforce a random-walk-type diffusion. While leading to small net displacements, this type of diffusion favors the excitation of long-lived Rayleigh surface phonon modes, which efficiently confine the released chemical energy within a nanoscopic hot spot around the impingement region. This suggests that transient mobility might be more common than hitherto anticipated, possibly extending particularly to systems where it has been dismissed on the basis of nearest-neighbor-type end distances. From the computed decay constants, we estimate an average of 10 ps to a full thermalization of the O adatoms at Pd(111). With an initial kinetic energy corresponding to several thousands of kelvin this is a long time to induce hot chemistry.

S. P. Rittmeyer is thanked for the nonadiabatic energy loss estimate and for many stimulating discussions. Funding through the Deutsche Forschungsgemeinschaft is acknowledged within Grant No. RE1509/19-1, as is generous access to CPU time through the Leibniz Rechenzentrum der Bayerischen Akademie der Wissenschaften (Grant No. pr85wa).

*vanessa.bukas@ch.tum.de

[1] J. Harris and B. Kasemo, Surf. Sci. **105**, L281 (1981).
[2] W. F. Egelhoff and I. Jacob, Phys. Rev. Lett. **62**, 921 (1989).
[3] A. Carley, P. Davies, and M. Roberts, Catal. Lett. **80**, 25 (2002).

[4] G. Ertl, in *Impact of Surface Science on Catalysis*, Advances in Catalysis Vol. 45 (Academic Press, New York, 2000), pp. 1–69.
[5] I. Chorkendorff and J. W. Niemantsverdriet, in *Concepts of Modern Catalysis and Kinetics* (Wiley-VCH Verlag GmbH & Co. KGaA, Weinheim, Germany, 2005), pp. 267–299.
[6] K. Reuter, in *Modeling and Simulation of Heterogeneous Catalytic Reactions* (Wiley-VCH Verlag GmbH & Co. KGaA, Weinheim, Germany, 2011), pp. 71–111.
[7] H. Brune, J. Wintterlin, R. J. Behm, and G. Ertl, Phys. Rev. Lett. **68**, 624 (1992).
[8] J. Wintterlin, R. Schuster, and G. Ertl, Phys. Rev. Lett. **77**, 123 (1996).
[9] B. G. Briner, M. Doering, H.-P. Rust, and A. M. Bradshaw, Phys. Rev. Lett. **78**, 1516 (1997).
[10] M. Rose, A. Borg, J. Dunphy, T. Mitsui, D. Ogletree, and M. Salmeron, Surf. Sci. **561**, 69 (2004).
[11] S. Schintke, S. Messerli, K. Morgenstern, J. Nieminen, and W.-D. Schneider, J. Chem. Phys. **114**, 4206 (2001).
[12] M.-F. Hsieh, D.-S. Lin, H. Gawronski, and K. Morgenstern, J. Chem. Phys. **131**, 174709 (2009).
[13] C. Sprodowski, M. Mehlhorn, and K. Morgenstern, J. Phys. Condens. Matter **22**, 264005 (2010).
[14] M. Schmid, G. Leonardelli, R. Tschelienig, A. Biedermann, and P. Varga, Surf. Sci. **478**, L355 (2001).
[15] J. Meyer and K. Reuter, Angew. Chem., Int. Ed. Engl. **53**, 4721 (2014).
[16] J. P. Perdew, K. Burke, and M. Ernzerhof, Phys. Rev. Lett. **77**, 3865 (1996); **78**, 1396 (1997).
[17] M. I. Baskes, Phys. Rev. B **46**, 2727 (1992).
[18] S. R. Bahn and K. W. Jacobsen, Comput. Sci. Eng. **4**, 56 (2002).
[19] V. Blum, R. Gehrke, F. Hanke, P. Havu, V. Havu, X. Ren, K. Reuter, and M. Scheffler, Comput. Phys. Commun. **180**, 2175 (2009).
[20] S. Plimpton, J. Chem. Phys. **117**, 1 (1995).
[21] See Supplemental Material at http://link.aps.org/supplemental/10.1103/PhysRevLett.117.146101 for a detailed description of the employed computational settings, phonon dispersion, energy uptake, and movies of the presented QM/Me-AIMD trajectories. The Supplemental Material includes the additional Refs. [22–25].
[22] A. Eichler, F. Mittendorfer, and J. Hafner, Phys. Rev. B **62**, 4744 (2000).
[23] C. Carbogno, A. Gross, J. Meyer, and K. Reuter, in *Dynamics of Gas-Surface Interactions*, edited by R. D. Muiño and H. F. Busnengo, Springer Series in Surface Sciences Vol. 50 (Springer, New York, 2013), pp. 389–419.
[24] D.-J. Liu and J. W. Evans, Phys. Rev. B **89**, 205406 (2014).
[25] H. J. Monkhorst and J. D. Pack, Phys. Rev. B **13**, 5188 (1976).
[26] V. J. Bukas, S. Mitra, J. Meyer, and K. Reuter, J. Chem. Phys. **143**, 034705 (2015); V. J. Bukas, J. Meyer, M. Alducin, and K. Reuter, Zeitschrift für Physikalische Chemie **227**, 1523 (2013).
[27] P. Sjövall and P. Uvdal, Chem. Phys. Lett. **282**, 355 (1998); P. Nolan, B. Lutz, P. Tanaka, and C. Mullins, Surf. Sci. **419**, L107 (1998).
[28] G. Henkelman, B. P. Uberuaga, and H. Jónsson, J. Chem. Phys. **113**, 9901 (2000).
[29] A. J. H. McGaughey and M. Kaviany, Phys. Rev. B **69**, 094303 (2004).
[30] J. Meyer, Ph.D. thesis, Freie Universität Berlin, 2012.
[31] M. D. Stiles, J. W. Wilkins, and M. Persson, Phys. Rev. B **34**, 4490 (1986).
[32] M. Hand and J. Harris, J. Chem. Phys. **92**, 7610 (1990).
[33] B. Jackson, Comput. Phys. Commun. **80**, 119 (1994).
[34] S.-I. Tamura, Phys. Rev. B **30**, 610 (1984).
[35] J. C. Hensel and R. C. Dynes, Phys. Rev. Lett. **39**, 969 (1977).
[36] M. Bonn, S. Funk, C. Hess, D. N. Denzler, C. Stampfl, M. Scheffler, M. Wolf, and G. Ertl, Science **285**, 1042 (1999).
[37] The accumulated nonadiabatic energy loss due to electronic friction [38] is estimated as $\eta = \int_0^{\Delta t} dt \eta \langle v \rangle^2(t)$, where $\langle v \rangle^2(t)$ is the average velocity per Pd atom in the reaction zone and $\Delta t = 3$ ps is the length of the QM/Me-AIMD trajectory. The respective electronic friction coefficient η is evaluated for a Pd atom embedded in jellium [39] with an electronic density equal to the Wigner-Seitz radius of bulk Pd [40].
[38] J. I. Juaristi, M. Alducin, R. DiezMuiño, H. F. Busnengo, and A. Salin, Phys. Rev. Lett. **100**, 116102 (2008); S. P. Rittmeyer, J. Meyer, J. I. Juaristi, and K. Reuter, Phys. Rev. Lett. **115**, 046102 (2015).
[39] A. Arnau, P. Echennique, and R. Ritchie, Nucl. Instrum. Methods Phys. Res. **33**, 138 (1988).
[40] V. Moruzzi, J. Janak, and A. Williams, in *Calculated Electronic Properties of Metals*, edited by V. Moruzzi, J. Janak, and A. Williams (Pergamon, New York, 1978), pp. 1–10.
[41] P. Saalfrank, Chem. Rev. **106**, 4116 (2006); I. Lončarić, M. Alducin, P. Saalfrank, and J. I. Juaristi, Phys. Rev. B **93**, 014301 (2016).
[42] S. Dudarev, Annu. Rev. Mater. Res. **43**, 35 (2013).

Paper #4

Phononic dissipation during "hot" adatom motion: A QM/Me study of O_2 dissociation at Pd surfaces. V. J. Bukas and K. Reuter; J. Chem. Phys., *accepted for publication* (2016)

Phononic dissipation during "hot" adatom motion: A QM/Me study of O_2 dissociation at Pd surfaces

Vanessa J. Bukas[1, a)] and Karsten Reuter[1]
Chair for Theoretical Chemistry and Catalysis Research Center, Technische Universität München, Lichtenbergstr. 4, D-85747 Garching, Germany

(Dated: 21 December 2016)

We augment *ab initio* molecular dynamics simulations with a quantitative account of phononic dissipation to study the non-equilibrium aftermath of the exothermic oxygen dissociation at low-index (111), (100), and (110) Pd surfaces. Comparing the hyperthermal diffusion arising from a non-instantaneous dissipation of the released chemical energy, we find a striking difference in the resulting "hot" adatom lifetime that is not overall reflected in experimentally recorded product end distances. We rationalize this finding through a detailed mode-specific phonon analysis and identify the dominant dissipation channels as qualitatively different groups of localized surface modes that ultimately lead to intrinsically different rates of dissipation to the Pd bulk. The thus obtained first-principles perspective on non-equilibrium adsorbate-phonon dynamics thereby underscores the sensitive dependence on details of the phononic fine structure, while questioning prevalent assumptions about energy sinks made in commonly used model bath Hamiltonians.

PACS numbers: 34.35.+a,68.43.Bc,82.53.St,63.22.-m

I. INTRODUCTION

Surface diffusion is a vital step in a number of important surface dynamical processes such as epitaxial growth, the self-assembly of surface nanostructures, or catalytically relevant chemical reactions. The prevalent notion of thermal diffusion presupposes the adsorbate's continuous equilibration with the surface and correspondingly predicts a temperature dependence dictated by the substrate temperature. This is contrasted by the concept of hyperthermal transient mobility, which results from the intrinsic exothermicity of an immediately preceding elementary step like (dissociative) adsorption. The hyperthermal diffusion is then governed by the delayed energy dissipation to the underlying substrate rather than the substrate's overall temperature. A corresponding transient mobility has been proposed recurrently, and attracts increasing attention for instance in view of its ability to generate "hot" precursors for subsequent reaction steps[1]. Ensuing for example the (exothermic) dissociative oxygen adsorption, resulting hot O adatoms have been suggested to promote oxide nucleation at low temperatures[2] while also offering promises for opening up low-energy pathways in oxidation catalysis[3].

Despite this suspected importance it has hitherto proven rather challenging to really grasp such hyperthermal diffusion processes even in the idealized regime of single-crystal surfaces and ultra-high vacuum (UHV). Experiments providing the required atomic spatial resolution are unable to explicitly access the picosecond dynamical motion. Instead, the hyperthermal motion is at best indirectly inferred in scanning tunneling microscopy (STM) studies performed at temperatures that are sufficiently low to suppress thermal diffusion. Such studies focused heavily on the dissociative and highly exothermic adsorption of O_2 at transition metal surfaces[4–9]. An ensuing transient mobility is there derived from recorded larger separation distances of adatom pairs; an indirect procedure that has caused quite some controversy[10].

Predictive-quality theoretical work would provide the necessary spatial and temporal resolution, yet has struggled with the necessity to both provide a reliable account of the quantum-mechanical (QM) surface chemical interactions and the heat dissipation into the phononic degrees of freedom. Straightforward *ab initio* molecular dynamics (AIMD) simulations in computationally tractable supercell geometries suffer from unphysical phonon reflections at the periodic boundaries and an inadequate description of the phononic band structure. Alternatively pursued Langevin-type approaches remove the phonon reflections in finite-size supercells by relying on bath Hamiltonians to describe the phononic degrees of freedom, cf. for example Refs 11–13. The practical bottleneck here are the assumptions that have to be made with respect to the bath Hamiltonian. With very little generally known about adsorbate-surface or surface-bath coupling constants, rather crude descriptions represent the state of the art. Based mainly on energetic considerations, low-frequency Rayleigh modes are for instance generally assumed to be predominantly excited upon first impact with the surface. Some justification for this conjecture has in fact been provided by early studies of light atomic or molecular species scattering off noble metals (cf. for example Ref. 14 and references therein), while instances have also been reported to put it into question[24]. The validity extent of this assumption thus overall remains to its larger extent unknown. On the other hand, there is vice verca the question of how well these microscopic details need to be described from a modeling

a)Electronic mail: vanessa.bukas@ch.tum.de

perspective in order to arrive at a reliable description of the actual adsorbate dynamics.

In this situation, the recent advent of the QM/MM embedding approach for metals (originally coined, and hence referred to, as "QM/Me") allowed for a big step forward[15]. Within a multi-scale modeling philosophy, this embedding scheme complements a density-functional theory (DFT) based treatment of the immediate reaction zone around the adsorbate impingement site with a quantitative treatment of phononic dissipation into an extended substrate described at the molecular modeling (MM) level. In a first comparative study applying this QM/Me scheme to different metal facets we compared the hot adatom diffusion ensuing O_2 dissociation over Pd(100) and Pd(111)[16]. This revealed the experimentally accessible product end distances as a rather misleading measure for the lifetime of the hyperthermal state. The latter was found to be particularly long at Pd(111), where a random-walk type diffusion leads only to small net displacements. In contrast, the symmetry of the more "open" Pd(100) surface allows for channel-type diffusion and concomitant longer net displacements - yet at a rather short lifetime.

This already demonstrates a complex dependence on microscopic details of the dissipative dynamics. Here, we now directly investigate the role of substrate symmetry by providing a detailed mode-specific phonon analysis to compare the equilibration ensuing O_2 dissociation at all three low-index (111), (100) and (110) Pd facets. Despite the similarly high exothermicity of the dissociative reactions and comparable barriers for atomic diffusion, we find a striking difference in the degree of the resulting hyperthermal mobility, i.e. the O adatoms remain "hot" for shorter or longer periods of time on each of the substrates. We rationalize this finding by identifying the dominant dissipation channels as qualitatively different surface modes that do not necessarily involve the Rayleigh modes at the lower energy end of the phononic spectra. This ultimately leads to intrinsically different rates of dissipation from the three surfaces to the Pd bulk, as verified by quantifying the phononic energy uptake directly from the QM/Me-AIMD trajectories. We thus overall underscore the importance of modeling the "right" surface excitations, while offering a first-principles perspective on the phonon parameters that enter prevalent heat bath models.

II. METHODS

A. QM/Me: An Embedding Approach for Metals

QM/Me is an embedding scheme specifically designed to treat dynamical processes at metal surfaces[15]. Its originality, in comparison to QM/MM embedding as routinely employed in the modeling of biomolecules or band-gap materials[17–19], lies in avoiding the use of finite QM clusters. The embedded QM region is instead calculated using periodic boundary condition (PBC) supercells, as is required to fully capture the delocalized metallic band structure and its crucial importance to adsorption. The embedding into the MM region is then achieved by separating the chemical and elastic contributions in the QM interaction potential, which leads to the following embedding ansatz for an atom at position $\mathcal{R}$:

$$V^{\mathrm{QM/Me}}(\mathcal{R}) = V^{\mathrm{Me}}(\mathcal{R}_{\mathrm{bath}}) + \underbrace{\left[E^{\overline{\mathrm{QM}}}(\mathcal{R}_{\mathrm{slab}} \cup \mathcal{R}_{\mathrm{ads}}) - E^{\overline{\mathrm{QM}}}(\mathcal{R}_{\mathrm{slab}})\right]}_{V^{\Delta\overline{\mathrm{QM}}}(\mathcal{R}_{\mathrm{slab}} \cup \mathcal{R}_{\mathrm{ads}})} , \quad (1)$$

where the coordinate sets $\mathcal{R}_{\mathrm{bath}}$, $\mathcal{R}_{\mathrm{slab}}$, and $\mathcal{R}_{\mathrm{ads}}$ correspond to all metal atoms in the MM simulation cell, to the metal atoms in the embedded QM supercell, and the adsorbate atoms, respectively.

Equation (1) defines $V^{\Delta\overline{\mathrm{QM}}}$ as the specific chemical adsorbate-substrate and adsorbate-adsorbate interactions. It is obtained in practice from two successive DFT calculations within identical periodic supercells: The first includes the adsorbate atoms and the second excludes them, while in both cases the positions of the substrate atoms ($\mathcal{R}_{\mathrm{slab}}$) remain unchanged. Forming the difference of these calculations thus cancels contributions of elastic interactions in the metal substrate and leaves only the adsorbate-induced chemical interactions. The latter are sufficiently short-ranged to be well contained within the finite extent of computationally tractable supercells. Even though calculated within PBCs, $V^{\Delta\overline{\mathrm{QM}}}$ extends thus only over a finite region. V^{Me} then provides the missing elastic contributions from substrate-substrate interactions due to lattice deformations that occur with the progressing chemical reaction. They are accurately described by many-body classical interatomic potentials and the numerical efficiency of the latter allows to explicitly model them in an extended MM region. Several tens of thousand bath atoms can thus easily be included without the evaluation of V^{Me} becoming a computational bottleneck and without the simulation being affected by the lateral PBCs which we impose on the MM region for the sake of convenience.

"Embedding" $V^{\Delta\overline{\mathrm{QM}}}$ in V^{Me} through Eq. 1 thus complements first-principles based dynamical simulations of chemical reactions at metal surfaces with an explicit account of the energy dissipation into an atomically-resolved heat bath. It is exactly this atomic resolution that lays the foundations for the phonon analysis described in Section II B and the thereby derived important information on the microscopic details of energy dissipation.

B. Phonon Projection Scheme

In the following we describe a rigorous projection scheme used to quantitatively assess phononic excitations in a mode-specific manner by using information that can

be directly extracted from AIMD simulations. As already indicated, such an analysis is only made possible here by explicitly considering the atomistic details in the extended MM region and thus incorporating a realistic description of the phononic fine structure into the QM/Me Hamiltonian, cf. Eq. 1. A challenge remains, however, in making contact with the phonon dispersion relation in order to identify the nature of excited modes through their actual wave vector, while in the meantime circumventing the computationally formidable task of diagonalizing the dynamical matrix of a MM region that contains in excess of hundred thousand atoms.

We achieve this on the basis of a projection methodology that allows to represent the complex atomic displacement pattern of the atoms in the large MM region as a superposition of the normal mode displacement eigenvectors of a laterally periodic surface primitive cell. Phonons realized in different branches at the $\bar{\Gamma}$-point in the small Brillouin zone of the supercell are thus effectively backfolded into the (larger) Brillouin zone corresponding to the chosen surface primitive cell. The target phonon mode expansion coefficients then depend on time only through the real-space displacement field, which can be straightforwardly obtained at any time step of a MD trajectory. The projection scheme is thus rendered suitable for instantaneous application without the need for an averaging over time. This already offers a prodigious advantage over methods that rely on time autocorrelation functions to arrive at occupied phonon densities, in particular within first-principles based approaches for which a quantitative phonon analysis has thus far remained impractical or even impossible (cf. for example Refs 20–22).

The rigorous formulation of the phonon projection scheme was originally laid out by McGaughey and Kaviany for the monatomic ($N_{\mathrm{cell}} = 1$) bulk primitive cell of Lennard-Jones model crystals[23]. For the present application on a two-dimensional slab that extends over a sufficient number of surface layers (N_{layers}) this has been appropriately extended to a polyatomic primitive cell, a detailed derivation of which may be found in Ref. 24. This cell specifically contains a single atom per layer for the low-index fcc surfaces investigated here ($N_{\mathrm{cell}} = N_{\mathrm{layers}}$), while an arbitrarily large supercell can then be constructed by ($N_1 \times N_2$) repetitions in the lateral periodic directions.

The starting point is then the atomic displacement field of the MM supercell containing $N_{\mathrm{supercell}}$ ($\equiv N_1 \times N_2 \times N_{\mathrm{layers}}$) atoms. This displacement field is described in the $3N_{\mathrm{supercell}}$-dimensional vector $\boldsymbol{U}^{\mathrm{MD}}(t)$ that denotes the Cartesian displacements with respect to the equilibrium positions $\boldsymbol{R}^0$ at a given time t during the MD simulation. The vector is defined on the real-space lattice grid ($\boldsymbol{L}_n$) of the atomic positions and can be transformed onto the corresponding reciprocal grid ($\boldsymbol{q}_n$) of exact phonon wave vectors by means of a discrete two-dimensional spatial Fourier transform:

$$U^{\mathrm{MD}}_{\tilde{I}_\alpha}(\boldsymbol{L}_n;t) = \frac{1}{\sqrt{N_1 N_2}} \frac{1}{\sqrt{M_{\tilde{I}}}} \sum_{\boldsymbol{q}_{n'}}^{\mathrm{grid}} \left(\sum_{b'=1}^{3N_{\mathrm{layers}}} C(\boldsymbol{q}_{n'}, b'; t) \hat{u}_{\tilde{I}_\alpha}(\boldsymbol{q}_{n'}, b') \right) e^{i\boldsymbol{q}_{n'}\cdot\boldsymbol{L}_n} \quad . \tag{2}$$

The transformation is performed component-wise with Cartesian vector coordinates $\alpha = (x, y, z)$ and for every atom in the supercell. The latter are indexed by a number $\tilde{I}$ in the primitive cell (denoting the specific surface layer) and a two-dimensional lattice vector $\boldsymbol{L}$ leading to the desired periodic image (n) in the lateral directions. At every point $\boldsymbol{q}_{n'}$ the phonon mode expansion coefficients $C(\boldsymbol{q}_{n'}, b'; t)$, which are the key quantities of interest here, are represented in the orthonormalized basis of generally complex-valued displacement eigenvectors $\{\hat{u}_{\tilde{I}_\alpha}(\boldsymbol{q}_{n'}, b')\}_{b'} \subset \mathbb{C}^{3N_{\mathrm{layers}}}$, where b' is the phonon band index. Finally, masses ($M_{\tilde{I}}$) are separated out of the latter which are therewith given in mass-weighted coordinates as is the common convention in lattice dynamics.

As already indicated above, $\boldsymbol{q}$-points of the reciprocal-space grid are chosen such that the two-dimensional periodicity of the phonons is commensurate with the chosen supercell and hence described exactly. Making use of the orthonormality relations for both the discrete Fourier transform and the displacement eigenvectors greatly simplifies the task of obtaining the target $C(\boldsymbol{q}_n, b; t)$ from Eq. 2 and leads to the following ansatz:

$$C(\mathbf{q}_n, b; t) = \frac{1}{\sqrt{N_1 N_2}} \sum_{n}^{N_1 \times N_2} \sum_{\tilde{I}}^{N_{\mathrm{layers}}} \sqrt{M_{\tilde{I}}} [\hat{\mathbf{u}}_{\tilde{I}}(\mathbf{q}_n, b)]^* \cdot U^{\mathrm{MD}}_{n\tilde{I}}(t) \mathrm{e}^{-i\mathbf{q}_n\cdot(\mathbf{R}^0_{n\tilde{I}} - \mathbf{R}^0_{\tilde{I}})} \quad , \tag{3}$$

where the double-index $n\tilde{I}$ iterates over all $N_{\mathrm{supercell}}$ atoms in the MM supercell.

Following the same decomposition of Eq. 2 and the ensuing formalism also for the velocity field $\dot{\boldsymbol{R}}^{\mathrm{MD}}(t)$ yields

corresponding velocity expansion coefficients $\dot{C}(\boldsymbol{q}_n, b; t)$. Under the harmonic approximation, the total energy of a single phonon mode can then be expressed as

$$\begin{aligned}\varepsilon^{\mathrm{ph}}(\boldsymbol{q}_n, b; t) &= \varepsilon^{\mathrm{ph}}_{\mathrm{kin}}(\boldsymbol{q}_n, b; t) + \varepsilon^{\mathrm{ph}}_{\mathrm{pot}}(\boldsymbol{q}_n, b; t) \\ &= \frac{1}{2}|\dot{C}(\boldsymbol{q}_n, b; t)|^2 + \frac{1}{2}\omega^2(\boldsymbol{q}_n, b)|C(\boldsymbol{q}_n, b; t)|^2 \quad ,\end{aligned} \tag{4}$$

where the two terms correspond to the kinetic and (harmonic) potential energy of the corresponding mode with frequency ω. To the extent that the harmonic approximation holds, Eq. 4 thus forms the foundation for quantifying the total phononic energy uptake

$$E^{\mathrm{ph}}_{\mathrm{tot}}(t) = \sum_{\boldsymbol{q}_n}^{\mathrm{grid}} \sum_{b=1}^{3N_{\mathrm{layers}}} \varepsilon^{\mathrm{ph}}(\boldsymbol{q}_n, b; t) \quad , \tag{5}$$

while the provided mode selectivity allows to also focus on certain groups of modes and assess their role during the dissociation dynamics.

C. Computational & Technical Details

The oxygen-Pd interaction energetics are obtained by DFT calculations within the generalized gradient approximation and using the exchange correlation (xc) functional due to Perdew, Burke and Ernzerhof (PBE)[25]. The approximate account of electronic xc in the semi-local PBE functional is known to lead to spurious ferromagnetic ordering in bulk palladium[26]. To suppress this, we assume perfect quenching of the O_2 spin-triplet state close to the metal surface[27] and conduct all calculations in a non-spin polarized manner. Electronic states are described with an all-electron basis set as implemented within the `FHI-aims` code[28]. Specifically, the "tier2" basis set with the internal default `tight` settings for the numerical integrations are employed in the description of O atoms and Pd atoms belonging to the topmost surface layer. "Tier1" and `light` settings are chosen for all remaining Pd atoms. For the optimized O adsorption energies at all three considered Pd surfaces, this setup was found to significantly reduce the computational effort at an insignificant additional uncertainty <10 meV as compared to calculations performed at full "tier2"/`tight` level.

The effective separation of short-ranged chemical and long-ranged elastic interactions crucially relied upon by QM/Me holds only upon vanishing force differences $F^{\Delta\overline{\mathrm{QM}}}$ for Pd atoms at the boundaries of the embedded QM supercell and their larger distance from the adsorbate(s). Careful checks were thus performed to ensure that such force components on most distant atoms have decayed to $\leq 10^{-2}\,\mathrm{eV/Å^2}$ in order to minimize boundary effects for the embedding cells employed in this work. These consist of three layer slabs which are (6×3), (9×3) and (6×6) multiples of the Pd(110), Pd(100) and Pd(111) surface unit cells, respectively. These QM supercells are illustrated in the insets of Fig. 1 and each features a vacuum region of 30 Å. Calculations are performed using (2×4×1), (2×4×1) and (2×2×1) Monkhorst-Pack grids[29] for k-point sampling of the O_2-Pd(110), O_2-Pd(100) and O_2-Pd(111) systems, respectively. Using these computational settings consistently for both DFT calculations required at each time step (here, of a 2.5 fs length) during a QM/Me-based MD simulation ensures a numerically well-defined construction of $F^{\Delta\overline{\mathrm{QM}}}(\mathcal{R}_{\mathrm{slab}})$ with negligible embedding-induced errors, as also verified by the high-quality energy conservation (< 0.5 meV per atom) obtained for the investigated trajectories.

A cubic (50×50×50) MM region, incorporating a total of 125,000 Pd atoms, is used to describe the long-range phonon propagation in all investigated Pd substrates. Such system sizes are still very much affordable within a classical treatment and ensure that phonon propagation has not yet reached the boundaries of the employed simulation boxes even for the longer trajectories (3 ps) considered in this work. The bath energetics are evaluated using the `LAMMPS`[30] package and at the level of a modified embedded atom method (MEAM) as originally developed by Baskes[31]. For the Pd(100) and Pd(111) slabs we specifically employ the MEAM reparameterization used in the more recent work of Meyer and Reuter[15] which was found to better reproduce first-principles based relaxation effects[32] at these two surfaces. As already indicated, QM/Me forces are evaluated independently on the DFT, MM levels of theory and atomic positions are communicated between the two at each MD time step. The latter are automatically re-scaled here through the use of fractional coordinates in order to overcome the limitation imposed by any residual lattice mismatches between the MEAM and our PBE-DFT description of the Pd substrate. We note that qualitatively similar results are obtained in the context of the adsorbate equilibration dynamics for all investigated systems when employing either the original or reparameterized version of the MEAM potential.

Classical MD simulations are performed at a zero initial temperature within the NVE ensemble and according to the QM/Me embedding scheme. We loosely interface the calculations performed independently on the DFT and MEAM levels through the `Atomic Simulation Environment` (ASE)[33]. Extending on the latter, a simple "master" script is responsible for: i) properly communicating the coordinate and force sets during each time step of the MD simulation, ii) collecting the ingredients needed to apply the embedding ansatz of Eq. 1, iii) propagating the system in time via the Velocity Verlet algorithm, and iv) book keeping the large input/output files.

Static stand-alone DFT calculations are performed based on the `FHI-aims` setup described above, but employing five-layer (3×3) (or (4×4)) surface slabs with (4×4×1) (or (3×3×1)) Monkhorst-Pack grids for k-point sampling. Relaxations are conducted using the Broyden-Fletcher-Goldfarb-Shanno (BFGS) algorithm and a convergence criterion of $F_{\mathrm{max}} \leq 10^{-2}\,\mathrm{eV/Å}$. Vibrational

modes of adsorbed oxygen atoms are obtained within the harmonic approximation by diagonalizing a finite difference approximation of the Hessian matrix as implemented within ASE. The forces are calculated for six displacements from the equilibrium state per oxygen atom: $\pm\delta$ for each Cartesian coordinate where δ is set to 10^{-2} Å. Finally, transition state searches are conducted with the ASE-implemented Climbing Image version of the Nudged Elastic Band (NEB) method[34], while typically constraining all but the topmost one or two Pd surface layers for reasons of computational efficiency.

Phonon modes are calculated using the finite displacement method, based on the implementation available within ASE and after loosely interfacing with the `LAMMPS`[30] package. Atoms in the relaxed primitive cell of the Pd(110), Pd(100) and Pd(111) slabs are displaced by $\pm 10^{-3}$ Å along each of the x, y and z directions. Laterally converged results for both the phonon band structures and spectral densities (as e.g. those shown in Figs. 2, 3, and 4 below) are obtained based on (6×6) multiples of the surface unit cell.

III. RESULTS AND DISCUSSION

A. Dissociative O_2 Adsorption at Low-Index Pd Surfaces

The dissociative adsorption of oxygen on the clean Pd(111), Pd(100) and Pd(110) surfaces is similarly exothermic, with PBE-DFT predicting the release of more than 2 eV per dissociating molecule. This similarity does not extend, however, to the underlying adsorption mechanism which varies between direct and/or precursor-mediated dissociation[35–38]. Aiming here at a reliable representation of the O_2 bond scission as a starting point for the ensuing equilibration process, we focus on establishing in each case initial conditions of particular statistical relevance for the representative QM/Me-AIMD trajectories presented in the following. For modeling direct dissociation at Pd(100), we thus investigate the dominant entrance channel from the gas phase. To initialize trajectories in the precursor-mediated dissociation over Pd(110) and Pd(111), we focus instead on the more readily accessible transition states (TS) between molecular and dissociative adsorption as identified via NEB calculations. A negligibly small initial kinetic energy is then properly distributed in the direction of the O_2 reaction coordinate simply to enforce the forward reaction which is subsequently dominated by the large intrinsic exothermicity of the dissociation event itself.

O_2 at Pd(100): Classical MD simulations[39] performed on a DFT-based PES that has been interpolated within a neural-network approach[40] shows direct dissociation at Pd(100) to proceed via one dominant entrance channel. This has gas-phase O_2 centering side-on above a fourfold hollow site with its molecular axis oriented along the [001] direction, i.e. in the direction of the neighboring hollow sites. The representative QM/Me-AIMD trajectory presented in the following is therefore initialized with molecular oxygen in such a configuration and at a height of 1.8 Å above the surface, where O-Pd energy exchange can still be considered negligible. The molecule is assigned an incident momentum normal to the surface that is consistent with the present PES description. Exploring the dominant entrance channel in nine further QM/Me-AIMD trajectories initialized at slightly different positions showed no qualitative effect on the central observables targeted here, i.e. the O-O end distances and concomitant phononic response.

O_2 at Pd(110): A twofold adsorption mechanism is suggested on Pd(110) that exhibits a strong energy dependence and has precursor-mediated dissociation dominating in particular at low O_2 incident energies[36]. As we will describe in detail elsewhere[41], static DFT calculations exploring the high-symmetry adsorption sites on the relaxed, unreconstructed Pd(110) slab show molecular chemisorption to be preferred when O_2 lies parallel to the surface. Energetically favorable pathways underlying in fact both dissociation mechanisms are found to proceed via the fourfold hollow site and with the molecular axis oriented along the $[1\bar{1}0]$ direction, i.e. along the surface troughs. Investigating the low-coverage molecular precursor state in particular reveals a deep potential well (E_b =1.1 eV) from which O_2 can escape via a low dissociation barrier (E_{diss} =173 meV) that elongates the O-O bond and results in the adatoms separating along $[1\bar{1}0]$. The corresponding TS, combined with an initial O_2 kinetic energy of 25 meV, is used here as a starting point for the QM/Me-AIMD trajectory presented in the following. Qualitatively similar results are, however, also obtained for investigating diffusion along the [001] surface channels, i.e. by initializing O_2 from the less exothermic TS (E_{diss} =653 meV) at a rotated top-hollow-top configuration (not shown). Nine trajectories in total overall confirm the qualitative picture discussed in the following regarding phononic dissipation and show no significant dependence on the initial kinetic energy or dissociative configuration.

O_2 at Pd(111): Molecular beam experiments show no direct dissociation at Pd(111)[37,38]. The surface potential steers impinging O_2 instead into molecular precursor states from which thermally accommodated oxygen can then only proceed to dissociation in a second step after sufficient heating. Here we predict the most stable such precursor states at the limit of low coverages as top-hollow-bridge configurations, i.e. with the O_2 center of mass essentially above a threefold hollow site and the molecular axis oriented along the $[1\bar{2}1]$ direction. Adsorption is energetically almost degenerate over the fcc and hcp hollow sites (E_b =891 meV and 831 meV, respectively) and yields vibrational O-O stretching frequencies (903cm^{-1}, 873cm^{-1}, respectively) that are in good agreement with previous theoretical work[42,43]. These values may equally well represent the frequency measured for the most abundant molecularly chemisorbed species at low coverages (800-840 cm^{-1}, depending on experimen-

tal conditions) by high-resolution electron energy loss spectroscopy (HREELS)[44]. Consistently, both molecular configurations exhibit similarly high dissociation barriers ($E_{\rm diss}$ =686 meV and 621 meV, respectively) along the calculated minimum energy paths that lead to a pair of oxygen atoms optimally adsorbed at identical neighboring hollow sites (hcp-hcp, fcc-fcc). Having no formal justification therefore for favoring either one or the other reaction path, we consider both involved TS geometries as the most probable candidate representatives for initializing nine O_2/Pd(111) trajectories in total. These start from exploring the strict vicinity of the aforementioned TSs for molecular oxygen and differ slightly in the assigned initial kinetic energy (in the range of 5-50 meV). While the latter yield qualitatively similar results, the specific trajectory discussed in the following is initialized from the (exact) dissociative TS above hcp and with an O_2 kinetic energy of 25 meV.

B. Equilibration Dynamics and "Hot" Adatoms

The top panels of Fig. 1 schematically illustrate the oxygen trajectories obtained following dissociation over Pd(110) (left), Pd(100) (middle) and Pd(111) (right), while d_{O-O} directly measures the adatom separation distance as a function of time. The evolution of kinetic energies in the lower panels show how the released reaction energy initially accelerates the resulting O adatoms and decays thereafter into the Pd substrate. This decay clearly occurs on a picosecond timescale on all surfaces, i.e. it is not instantaneous on the timescale of the actual dissociation dynamics. An appreciable difference is, however, observed in the rate of energy transfer that decreases with increasing surface packing from Pd(110) over Pd(100) to Pd(111). This is most prominently reflected in the fraction of dissipated energy that has been propagated by phonons outside the QM embedding cells already on these timescales. Depicted by the shaded gray areas in Fig. 1, this amounts to 82%, 73%, and 54% of the total energy that has been dissipated to the substrate at ca. 1 ps after the initial O_2 bond dissociation over Pd(110), Pd(100), and Pd(111) respectively. This first quantitative estimate of heat transfer thus already underscores here the importance of augmenting self-standing AIMD simulations (that rely on, at most, several tens of substrate atoms) with a proper description of bulk dissipation, and has important consequences for the actual adsorbate dynamics.

The varying dissipation rates on the three surfaces give rise to dissociation products of an intrinsically different degree of hyperthermal mobility. Efficient heat dissipation at Pd(110) results in slow oxygen adatoms that are promptly captured by the surface potential at the immediately adjacent long-bridge sites. Figure 1 thus shows the adsorbates equilibrating at a distance of only one SLC ($\sim$ 2.8 Å) and already within a few tens of fs after the O_2 molecular bond breaks, i.e. even before they reach the (second nearest neighbor) quasi-threefold coordinated trough sites which are most favorable for atomic adsorption. This effectively lowers the amount of energy released during the ps-scale "hot" reaction to ca. 1.7 eV, as compared to the ideal 2.5 eV for adsorption over hollow. Dissociation over Pd(100) and Pd(111) results instead in translationally "hot" products whose transient mobility is marked by a series of hyperthermal diffusive hops (indicated by arrows in Fig. 1) between neighboring binding sites. A largely increasing separation distance d_{O-O} is found on Pd(100) as the adatoms follow a channel-type diffusive motion along the [001] direction. Two hyperthermal hops over bridge bring the adatoms to fcc hollow sites at four SLCs apart ($\sim$ 11.2 Å)[45], where they equilibrate within ca. 1 ps. A random-walk type diffusion is instead found on the densely packed Pd(111) surface which has the adatoms primarily trapped in the vicinity of hollow sites. Collisions with neighboring Pd atoms randomize the direction of the O lateral motion and the adatoms eventually occupy hcp hollow sites at a much smaller O-O separation distance of only two times the SLC ($\sim$ 5.6 Å). And yet, Fig. 1 reveals intriguingly hot adatoms on Pd(111) with significant fluctuations in kinetic energy even after the four barrier crossings counted along the presented 3 ps trajectory. In full agreement with experiment[8], similarly short end distances (in the range of 1-3 SLCs) are predicted by a total of nine QM/Me-AIMD trajectories, from which the extracted decay constants nevertheless suggest an average of 10 ps to a full thermalization.

Experimentally accessible product end distances can thus form a particularly misleading measure of adsorbate hyperthermal mobility[16]. While not reflected here in the trend of equilibrium d_{O-O} values, transient hyperthermal lifetimes increase by approximately one order of magnitude for O_2 dissociating at each of the three low-index Pd surfaces. This is a particularly intriguing result given the similarly high exothermicity of the dissociative reactions (2.5, 2.3 and 2.7 eV at DFT-PBE level for the O adatoms optimally adsorbed at the favored hollow sites on Pd(110), Pd(100) and Pd(111) respectively) and barriers for atomic diffusion 421, 154, and 327 meV, respectively). The substantially different oxygen equilibration rates must therefore arise from qualitative differences in the underlying mechanism of phononic dissipation toward which we thus turn our attention in the following.

C. Exciting Phonons

Based on the projection scheme laid out in section II B, we analyze the corresponding phonon dynamics by evaluating the time-dependent (harmonic) phonon energies at specific time steps along the obtained QM/Me-AIMD trajectories. Even for the longest (3 ps) trajectories considered in this work, the total phononic energy $E_{\rm tot}^{\rm ph}$ calculated through Eq. 5 is found to be well contained

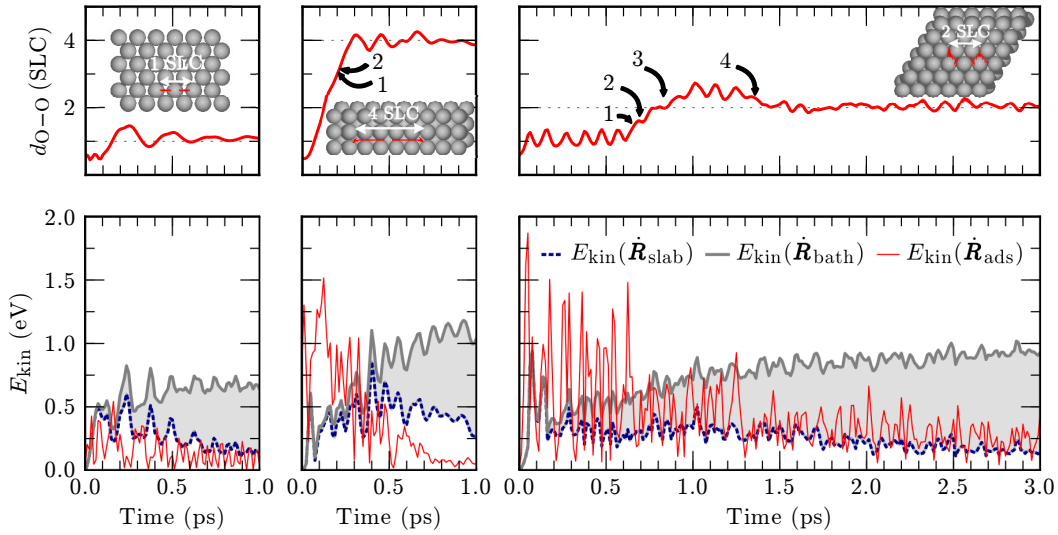

FIG. 1. (Color online) Dynamical information extracted from representative QM/Me-AIMD trajectories for O_2 dissociating at Pd(110) (left), Pd(100) (middle) and Pd(111) (right). Top panels: Separation distance of the oxygen adatoms in units of the surface lattice constant (SLC, ~ 2.8 Å). Hyperthermal adatom hops are numbered and schematically represented in a top-view of the DFT-described reaction zones in the figures insets. Lower panels: Kinetic energy of the Pd atoms contained in the QM embedding cell $E_{\rm kin}(\dot{\mathcal{R}}_{\rm slab})$ (dashed blue line), of all (125,000) Pd atoms in the heat bath $E_{\rm kin}(\dot{\mathcal{R}}_{\rm bath})$ (thick gray line), and of the adsorbates $E_{\rm kin}(\dot{\mathcal{R}}_{\rm ads})$ (thin red line). The area between the last two curves (shaded in gray) is correspondingly a measure of the heat dissipated outside of the QM reaction zone.

within (40×40) repeating units of 40-layer surface primitive cells, i.e. well within the boundaries of the employed MM region. In order to minimize the associated computational effort, commensurate reciprocal-space grids of a slightly reduced density are thus hereby employed to sample the corresponding twofold, fourfold and sixfold two-dimensional surface Brillouin zones of the Pd(110), Pd(100), and Pd(111) substrates, respectively. Comparing to the equivalent $E^{\rm ph}_{\rm tot}$ representation obtained by directly evaluating the anharmonic MEAM potential then provides a measure for the total error introduced by projecting onto a harmonic solid. The latter is found in all cases to yield an additive offset contribution which is particularly small during the early stages of the dissipation dynamics. For the results presented in the following, we specifically calculate a negligibly small absolute error of < 15 meV which thus conveys confidence in the emerging mechanistic analysis.

Energy resolved excitation spectra are calculated "on the fly" through a straightforward discretization of Eq. 4 along the energy ($\hbar\omega$) axis. While this greatly simplifies visualization, it is still the mode selectivity naturally provided by the underlying formalism that allows to focus on certain groups of modes. In particular the surface phonons obviously form a very prominent group in this context and are classified here as modes whose displacement eigenvector is localized to at least 20% in the two outermost slab layers. We verify that modifying this criterion has no qualitative effect on the presented results, but yields only quantitative changes simply because more or less phonons are identified as surface modes.

Figures 2, 3, and 4 show such excitation spectra calculated at $t = 50$ fs along the presented QM/Me-AIMD trajectories, i.e. during the very early stages of the oxygen adsorption dynamics. Intriguingly, despite their negligible spectral weight illustrated by the phononic density of states (DOS) in the middle panels, surface modes are found in all cases to carry a substantial fraction (45%, 45%, and 33% for Pd(110), Pd(100), and Pd(111), respectively) of the total energy that has been dissipated into the substrate at that time. Qualitative differences, however, in the phononic response have already set in and are clearly apparent.

At Pd(110) the dissipated energy is distributed within the entire frequency range of the phonon band structure which is given for reference in the leftmost panel of Fig. 2. The latter is decorated by a rich spectrum of both pure and resonant surface states (outlined by black markers), as expected by the large structural relaxation at this open surface[32]. The rightmost panel of Fig. 2 shows a strong non-equilibrium population of these modes (in black), with a significant fraction (33%) of the surface energy lying within a bulk-hybridized resonant state at intermediate frequencies (13-15 meV) that displays a predominantly longitudinal displacement pattern as it (partially) extends along $\bar{\Gamma} - \bar{\rm Y}$ (confirmed also in previous theo-

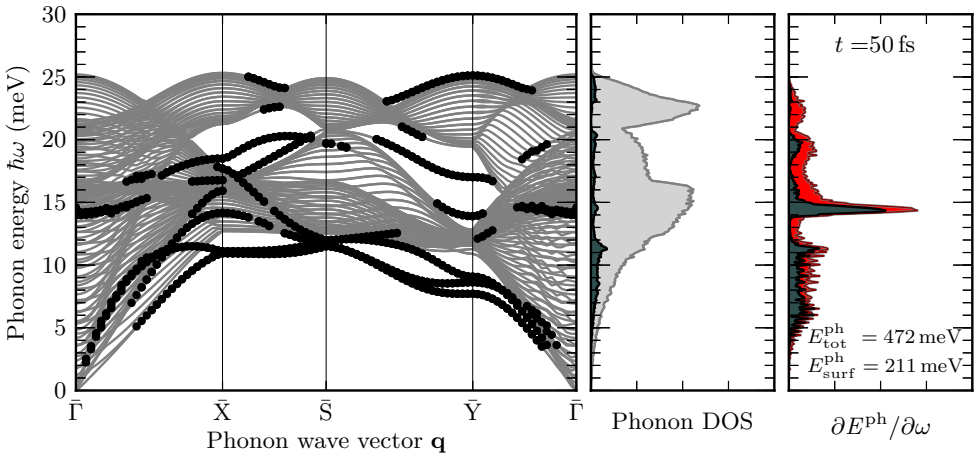

FIG. 2. (Color online) Rightmost panel: Energy resolved phonon excitation spectrum calculated at $t = 50$ fs along the QM/MM-AIMD trajectory of O_2 dissociating at Pd(110) as described in the main text. The total amount of energy ($E^{\rm ph}_{\rm tot}$) along with the fraction assigned to surface modes ($E^{\rm ph}_{\rm surf}$) are noted and correspond to the areas shaded red and black respectively. Middle and leftmost panels: The corresponding equilibrium bulk Pd phonon density of states (DOS) and phonon dispersion along the boundaries of the irreducible wedge are shown for reference. In all cases modes are classified as surface phonons if their displacement eigenvector is localized to $\geq 20\%$ in the outermost two slab layers and their contributions are indicated by black markers/thick lines.

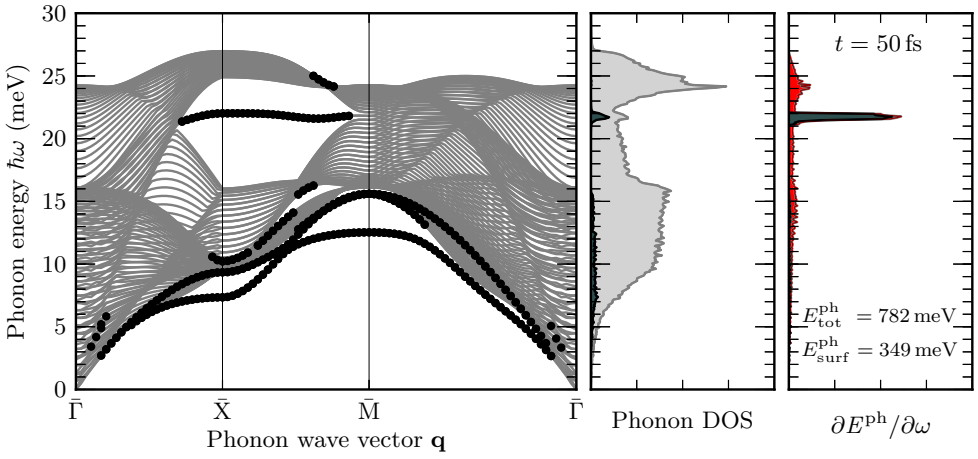

FIG. 3. (Color online) Same as Fig. 2, but for O_2 dissociating at Pd(100).

retical studies[32,46]). Quite in contrast therefore to what is predominantly assumed about energy sinks in model bath Hamiltonians (cf. for example Ref 47 and references therein), it is not the Rayleigh modes here that become dominantly excited although lying energetically below the onset of the bulk part of the spectrum. Anharmonic decay of the different Pd(110) surface excitations overall leads, already at this time, to substantial bulk excitation that obviously does not (directly) result from interaction with the adsorbate alone. Visualizing the distribution of bulk kinetic energy over the two-dimensional Pd(110) Brillouin zone at $t = 100$ fs (cf. inset of Fig. 5) reveals indeed a strongly perturbed phononic system with excitations spreading primarily around the $\bar{Y}$ symmetry point.

Figure 3 shows a qualitatively different picture at Pd(100) where the dissipated energy is highly concentrated in a single surface optical band of high frequencies (21-22 meV) that lies in a pseudogap between the bulk modes, in accordance with Refs. 16 and 24. Ana-

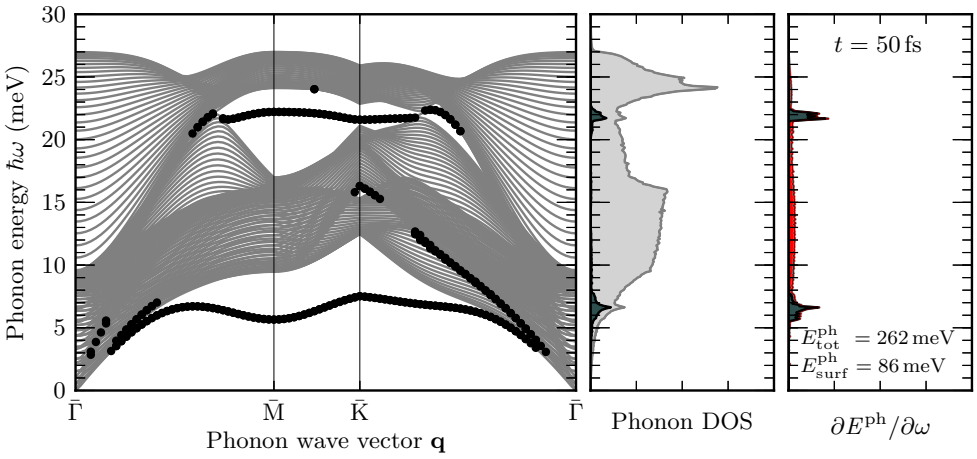

FIG. 4. (Color online) Same as Fig. 2, but for O_2 dissociating at Pd(111).

lyzing the mode eigenvectors straightforwardly rationalizes this unexpected non-Rayleigh excitation[16,24] by the preferred binding site of the O adatoms. Rather than indenting the topmost substrate layer upon impingement, which is the picture suggesting a predominant excitation of corresponding Rayleigh modes, the dissociating O atoms penetrate directly into the hollow sites and subsequently diffuse laterally over bridge sites along one of the [001] surface channels. Along this motion they rather push the top-layer Pd atoms laterally away, which corresponds exactly to the purely longitudinal displacement pattern of the modes belonging to the aforementioned surface optical phonon band[32,46].

The random-walk type diffusion of oxygen on Pd(111) leads instead to a weighted phonon population that essentially follows the surface DOS, cf. Fig. 4. Similar to Pd(100), high-frequency optical modes with a longitudinal character promptly decay into large wavelength bulk modes that reside in the strict vicinity of the $\bar{\Gamma}$-point, cf. insets of Fig. 5. The larger fraction of the released chemical energy is, however, contained within low-frequency acoustic phonons at short wavelengths. With their small group velocities, these notoriously long-lived Rayleigh waves[48] efficiently confine the released energy at the surface and within a small reaction zone around the O_2 impingement region. Within this region anharmonic phonon-phonon interactions quickly establish a quasi-equilibrium state that is sufficiently well described by a Planckian distribution. An effective local temperature extracted therefrom shows an increasingly "hot" surface that contrasts the corresponding bulk behavior and confirms minimal coupling between the two phononic sub-systems over the entire course of the QM/Me-AIMD trajectory[16].

The substantially different equilibration rates on the three surfaces are thus ultimately determined by microscopic details of the interfacial energy exchange. Efficient heat dissipation at Pd(110) is channeled through the multitude of surface excitations at a constant rate of $\sim 10\,\mathrm{meV/fs}$, as extracted from the evolution of the total phonon energy ($E^{\mathrm{ph}}_{\mathrm{tot}}$) in Fig. 5. The vast majority (94%) of the theoretically predicted 1.7 eV is thus already dissipated within the first 150 fs of the adsorption dynamics (while subsequent fluctuations around 100% reflect oxygen's metastable adsorption at the long-bridge sites). This contrasts the corresponding value of 0.79 eV for Pd(100) at this time. Nevertheless, a largely increasing phononic energy uptake is also observed here through the (sub-ps) anharmonic decay of the aforementioned highly populated surface optical band. Saturation of $E^{\mathrm{ph}}_{\mathrm{tot}}$ (at the theoretical value of 2.3 eV) is thus reached within about 1 ps after the initial O_2 bond dissociation and at a concomitant longer lifetime of the hyperthermal state. The substantially slower equilibration at Pd(111) results instead from the dominant excitation of long-lived Rayleigh waves which spatially confine the released chemical energy. As reflected by the non-monotonic behavior in the total phononic energy uptake, this promotes a back and forth O-Pd energy exchange and rationalizes the exceptional hyperthermal mobility observed at this surface.

The presented analysis thus offers a first-principles perspective on parameters entering effective models of substrate mobility, such as the prevalent Surface Oscillator[49] (SO) and Generalized Langevin Oscillator[11–13] (GLO) methodologies. Our results show that phononic excitations are intrinsically more complicated than postulated in common-practice representations of a single (usually low-frequency) surface oscillation[50], and certainly not transferable even between different surfaces of the (chemically) same substrate. As heralded however by recent first-principles based SO/GLO applications of H_2 at Pd[51], investigated statistical properties (typically sticking or scattering probabilities) have so far demonstrated

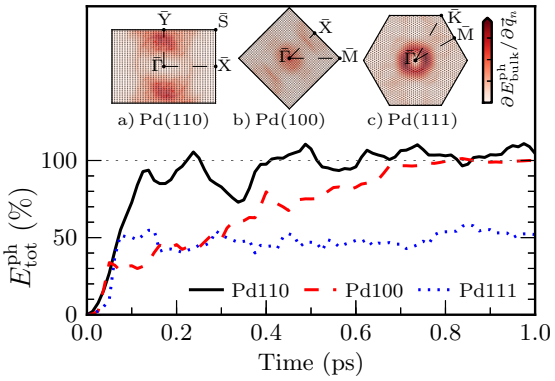

FIG. 5. (Color online) Phononic energy uptake along the presented QM/Me-AIMD trajectories as a fraction of the theoretically predicted chemical energy released during the "hot" reaction of O_2 dissociation at Pd(110) (solid black line), Pd(100) (dashed red line), and Pd(111) (dotted blue line). Insets (a,b,c): Distribution of bulk Pd kinetic energy over the two-dimensional surface Brillouin zones of the three surfaces at $t = 100$ fs. The coloring is based on a linear interpolation between values at exact phonon wavevectors ($\vec{q}_n$, black markers) at which the kinetic energy of all bulk phonon branches has been summed.

an exceptional insensitivity with respect to such input frequency parameters.

With increasing reaction exothermicity and/or concomitant adsorbate-substrate vibrational coupling, a higher sensitivity to the underlying phononic fine structure might nevertheless still be expected. Occurrences of resonant phenomena involving selective-phonon excitations are indeed not unheard of and have for example been shown to play an important role in the sticking of light H_2, HD molecules at metal surfaces[14]. We observe here a similar effect for O_2 dissociation and subsequent channel-type diffusion at Pd(110) and Pd(100) which, however, does not involve the predominantly assumed Rayleigh excitation, but rather optical surface modes at higher frequencies. The "right" surface excitations can thereby only be extracted from a detailed microscopic phonon analysis such as the one presented here. Picking up on these frequencies to use as input parameters in more numerically efficient heat bath models is now an obvious step forward. Whether the approximate nature of the latter will, however, allow for lifting the aforementioned insensitivity and capturing selective-adsorption resonances remains yet open to investigation.

IV. SUMMARY AND CONCLUSIONS

In summary, we augmented *ab initio* molecular dynamics simulations with a quantitative account of phononic dissipation and studied the equilibration process ensuing the exothermic oxygen dissociation at all low-index (110), (100), and (111) Pd surfaces. The specific motivation was to elucidate the influence of substrate symmetry on the resulting hyperthermal adatom mobility, while assessing the level of detail required to be accounted for in the underlying phonon excitations. We observe a striking difference in the hot O lifetime that decreases from Pd(110) over Pd(100) to Pd(111) and is not overall reflected in experimentally accessible product end distances. Whilst difficult to reconcile on purely energetic grounds, this finding already demonstrates a complex dependence on microscopic details of the dissipative dynamics.

Relying on our atomically-resolved description of a macroscopic heat bath, we unravel mechanistic details of the energy conversion process through a mode-specific phonon analysis. This reveals qualitative differences in the phononic response setting in already during the very first steps of oxygen dissociation. Excitation of specific groups of localized surface modes set the initial conditions for the ensuing phonon relaxation which is manifested through anharmonic phonon-phonon interactions and leads to intrinsically different rates of dissipation to the Pd bulk. Demonstrating how critically these microscopic details may influence the actual adsorbate dynamics thus nicely highlights the strengths of QM/Me embedding compared to previous theoretical treatments of phononic dissipation. Wahnström and co-workers for example entirely neglected such early surface excitations due to limitations of their semi-empirical potential in describing O_2 dissociation at Al(111) and concluded on minimal adsorbate-phonon coupling[52]. On the other hand, stand-alone AIMD simulations provide the desired predictive-quality chemical description but will unavoidably falsify the demonstrated picosecond-scale adsorbate equilibration due to the finite extent of computationally tractable supercells[15].

With qualitatively different surface excitations observed at both the high- and low-frequency regimes, we illustrate from a first-principles perspective a complex multi-phonon picture for the non-equilibrium adsorbate-phonon dynamics such as has been suggested in early experimental work for e.g. NO at Ag(111)[53]. In the meantime, we highlight the danger of generalizing the single-phonon approximation to strongly chemisorbing adsorbates that go beyond prototypical studies of light atom/molecule scattering[54]. In a systematic comparison with respect to surface symmetry, we relate real-space trajectories to the specific oxygen-induced excitations which can be subsequently used as input parameters for computationally attractive models of an effective substrate mobility.

ACKNOWLEDGMENTS

S. P. Rittmeyer is thanked for many stimulating discussions. Funding through the Deutsche Forschungsgemeinschaft is acknowledged within project RE1509/19-

1, as is generous access to CPU time through the Leibniz Rechenzentrum der Bayerischen Akademie der Wissenschaften (project pr85wa).

[1] J. Barth, Surf. Sci. Rep. **40**, 75 (2000).
[2] L. C. Ciacchi and M. C. Payne, Phys. Rev. Lett. **92**, 176104 (2004).
[3] A. Carley, P. Davies, and M. Roberts, Catal. Lett. **80**, 25 (2002).
[4] H. Brune, J. Wintterlin, R. J. Behm, and G. Ertl, Phys. Rev. Lett. **68**, 624 (1992).
[5] S. Schintke, S. Messerli, K. Morgenstern, J. Nieminen, and W.-D. Schneider, J. Chem. Phys. **114**, 4206 (2001).
[6] M.-F. Hsieh, D.-S. Lin, H. Gawronski, and K. Morgenstern, J. Chem. Phys. **131**, 174709 (2009).
[7] C. Sprodowski, M. Mehlhorn, and K. Morgenstern, J. Phys.-Condens. Mat. **22**, 264005 (2010).
[8] M. Rose, A. Borg, J. Dunphy, T. Mitsui, D. Ogletree, and M. Salmeron, Surf. Sci. **561**, 69 (2004).
[9] J. Wintterlin, R. Schuster, and G. Ertl, Phys. Rev. Lett. **77**, 123 (1996).
[10] M. Schmid, G. Leonardelli, R. Tschelienig, A. Biedermann, and P. Varga, Surf. Sci. **478**, L355 (2001); A. J. Komrowski, J. Z. Sexton, A. C. Kummel, M. Binetti, O. Weiße, and E. Hasselbrink, Phys. Rev. Lett. **87**, 246103 (2001).
[11] S. A. Adelman and J. D. Doll, J. Chem. Phys. **64**, 2375 (1976).
[12] J. C. Tully, J. Chem. Phys. **73**, 6333 (1980).
[13] J. C. Polanyi and R. J. Wolf, J. Chem. Phys. **82**, 1555 (1985).
[14] M. D. Stiles and J. W. Wilkins, Phys. Rev. Lett. **54**, 595 (1985).
[15] J. Meyer and K. Reuter, Angew. Chem. Int. Edit. **53**, 4721 (2014).
[16] V. J. Bukas and K. Reuter, Phys. Rev. Lett. **117**, 146101 (2016).
[17] H. Lin and D. Truhlar, Theor. Chem. Acc. **117**, 185 (2007).
[18] C. Bo and F. Maseras, Dalton Trans. , 2911 (2008).
[19] N. Bernstein, J. R. Kermode, and G. Csányi, Rep. Prog. Phys. **72**, 026501 (2009).
[20] M. M. Siddick, G. J. Ackland, and C. A. Morrison, J. Chem. Phys. **125**, 064707 (2006).
[21] N. de Koker, Phys. Rev. Lett. **103**, 125902 (2009).
[22] N. de Koker, Earth Planet. Sc. Lett. **292**, 392 (2010).
[23] A. J. H. McGaughey and M. Kaviany, Phys. Rev. B **69**, 094303 (2004).
[24] J. Meyer, *Ab initio modeling of energy dissipation during chemical reactions at transition metal surfaces*, Ph.D. thesis, Freie Universität Berlin, Germany (2012).
[25] J. P. Perdew, K. Burke, and M. Ernzerhof, Phys. Rev. Lett. **77**, 3865 (1996); Phys. Rev. Lett. **78**, 1396 (1997).
[26] S. S. Alexandre, E. Anglada, J. M. Soler, and F. Yndurain, Phys. Rev. B **74**, 054405 (2006); D. A. Stewart, New J. Phys. **10**, 043025 (2008).
[27] C. Carbogno, A. Gross, J. Meyer, and K. Reuter, in *Dynamics of Gas-Surface Interactions*, Springer Series in Surface Sciences, Vol. 50, edited by R. D. Muiño and H. F. Busnengo (Springer, 2013) pp. 389 – 419.
[28] V. Blum, R. Gehrke, F. Hanke, P. Havu, V. Havu, X. Ren, K. Reuter, and M. Scheffler, Comput. Phys. Commun. **180**, 2175 (2009).
[29] H. J. Monkhorst and J. D. Pack, Phys. Rev. B **13**, 5188 (1976).
[30] S. Plimpton, J. Chem. Phys. **117**, 1 (1995).
[31] M. I. Baskes, Phys. Rev. B **46**, 2727 (1992).
[32] R. Heid and K.-P. Bohnen, Phys. Rep. **387**, 151 (2003).
[33] S. R. Bahn and K. W. Jacobsen, Comput. Sci. Eng. **4**, 56 (2002).
[34] G. Henkelman, B. P. Uberuaga, and H. Jnsson, J. Chem. Phys. **113**, 9901 (2000).
[35] A. den Dunnen, S. Wiegman, L. Jacobse, and L. B. F. Juurlink, J. Chem. Phys. **142**, 214708 (2015).
[36] P. Junell, K. Honkala, M. Hirsimki, M. Valden, and K. Laasonen, Surf. Sci. **546**, L797 (2003).
[37] P. Sjövall and P. Uvdal, Chem. Phys. Let. **282**, 355 (1998).
[38] P. Nolan, B. Lutz, P. Tanaka, and C. Mullins, Surf. Sci. **419**, L107 (1998).
[39] V. J. Bukas, S. Mitra, J. Meyer, and K. Reuter, J. Chem. Phys. **143**, 034705 (2015).
[40] V. J. Bukas, J. Meyer, M. Alducin, and K. Reuter, Z. Phys. Chem. **227**, 1523 (2013).
[41] V. J. Bukas and K. Reuter, *in preparation*.
[42] A. Eichler, F. Mittendorfer, and J. Hafner, Phys. Rev. B **62**, 4744 (2000).
[43] K. Honkala and K. Laasonen, J. Chem. Phys. **115**, 2297 (2001).
[44] K. W. Kolasinski, F. Cemic, and E. Hasselbrink, Chem. Phys. Lett. **219**, 113 (1994).
[45] We ensure the equilibrium end-distance is not limited by unphysical O-O interactions through lateral periodic images of the embedding cell by pausing the QM/Me trajectory at a point for which $d_{O-O} = 3\,\mathrm{SLCs}$, i.e. where substrate mediated adsorbate interactions are expected to have largely vanished[55]. We thereby continue integration based on *two* (3×3) QM embedding cells centered around each oxygen atom and treated independently on the DFT level (yet still coupled via the the substrate motion described on the MEAM level). Having the cells dynamically "follow" the motion of the individual oxygen atoms over the surface reproduces the original trajectory, thus conveying further trust in both the embedding approach and the resulting maximum adatom separation distance.
[46] I. Sklyadneva, G. Rusina, and E. Chulkov, Surf. Sci. **377**, 313 (1997).
[47] M. D. Stiles, J. W. Wilkins, and M. Persson, Phys. Rev. B **34**, 4490 (1986); B. Jackson, Comput. Phys. Commun. **63**, 154 (1991); Comput. Phys. Commun. **80**, 119 (1994); J. Chem. Phys. **108**, 1131 (1998).
[48] S.-I. Tamura, Phys. Rev. B **30**, 610 (1984).
[49] M. Hand and J. Harris, J. Chem. Phys. **92**, 7610 (1990).
[50] G.-J. Kroes, Science **321**, 794 (2008).
[51] H. F. Busnengo, W. Dong, P. Sautet, and A. Salin, Phys. Rev. Lett. **87**, 127601 (2001); H. F. Busnengo, W. Dong, and A. Salin, Phys. Rev. Lett. **93**, 236103 (2004); H. F. Busnengo, M. A. Di Césare, W. Dong, and A. Salin, Phys. Rev. B **72**, 125411 (2005).
[52] C. Engdahl and G. Wahnström, Surf. Sci. **312**, 429 (1994); G. Wahnström, A. B. Lee, and J. Strömquist, J. Chem. Phys. **105**, 326 (1996).
[53] D. J. Auerbach, Phys. Scripta **1983**, 122 (1983).
[54] A. S. Sanz and S. Miret-Artés, Phys. Rep. **451**, 37 (2007).
[55] Y. Zhang, V. Blum, and K. Reuter, Phys. Rev. B **75**, 235406 (2007).